

:- i- 1.3

MICHIGAN STATE UNIVERSITY LIBRARIES
3 1293 00904 3880

This is to certify that the

dissertation entitled

STRUCTURE AND DYNAMICS OF LAYERED SYSTEMS

presented by

Hyangsuk Seong

has been accepted towards fulfillment of the requirements for

Ph. D degree in PHYSICS

Major professor

Date APRIL 21, 1993

# LIBRARY Michigan State University

PLACE IN RETURN BOX to remove this checkout from your record. TO AVOID FINES return on or before date due.

DATE DUE	DATE DUE	DATE DUE

MSU is An Affirmative Action/Equal Opportunity Institution c:\circ\detectus.pm3-p.1

# STRUCTURE AND DYNAMICS OF LAYERED SYSTEMS

 $\mathbf{B}\mathbf{y}$ 

Hyangsuk Seong

A DISSERTATION

Submitted to
Michigan State University
in partial fulfillment of the requirements
for the Degree of

DOCTOR OF PHILOSOPHY

Department of Physics and Astronomy

1993

### **ABSTRACT**

### Structure and Dynamics of Layered Systems

#### BY

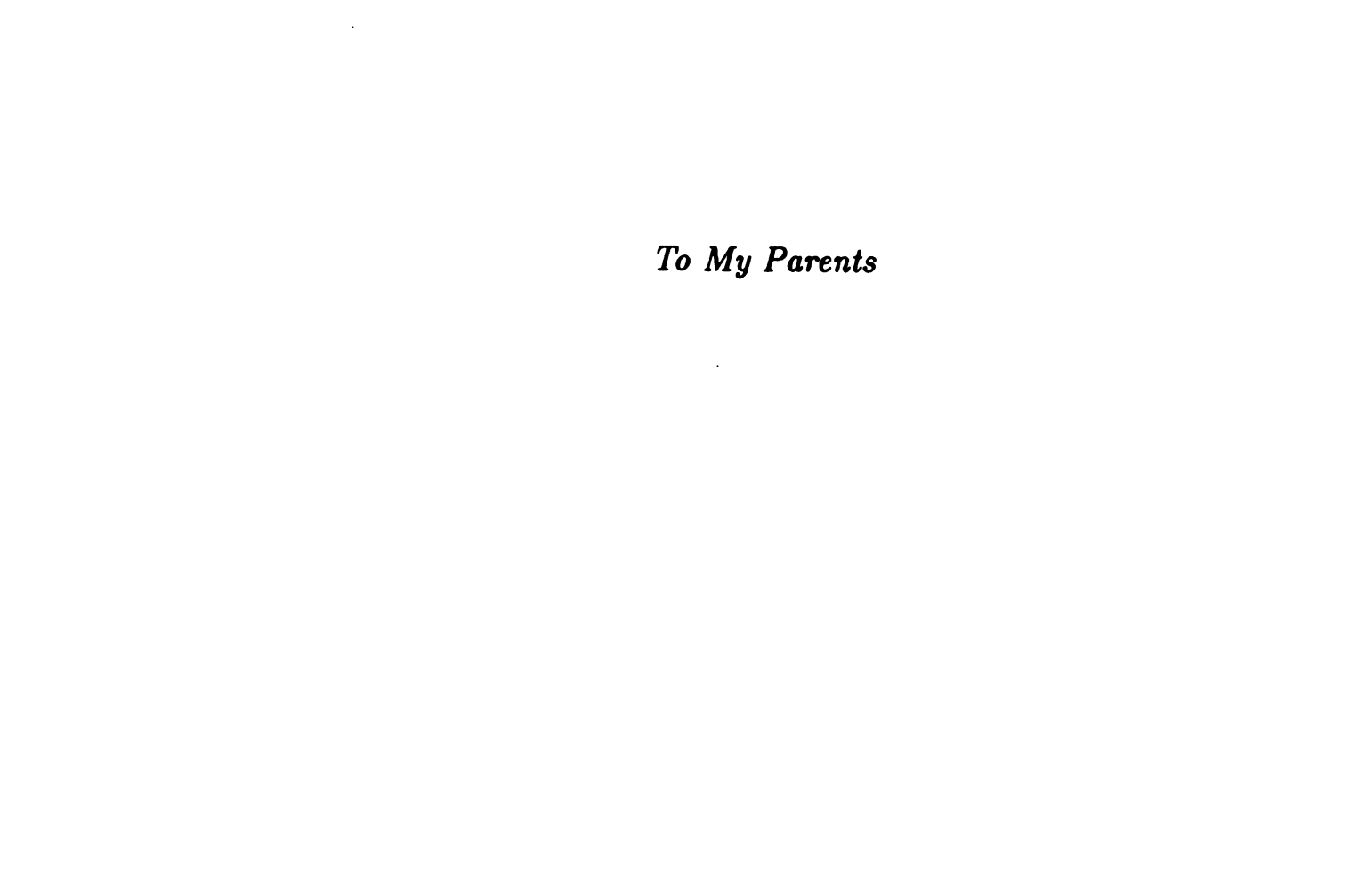
### Hyangsuk Seong

This dissertation addresses some of the current problems dealing with the structure and dynamics of layered solids. Three different types of physical systems have been studied. (1) 2-dimensional (2D) repulsive screened Coulomb systems in the presence of corrugation modelling a large class of intercalation compounds, (2) randomly intercalated layered solids modelling ternary intercalation systems, and (3) layered superlattices with interfacial disorder.

For (1), using molecular dynamics simulations we have investigated structural, thermodynamic, and dynamic properties as a function of the intercalant density and the strength of the corrugation. For physical parameters appropriate for  $RbC_{24}$ , we explain the observed low-T structure of the Rb intercalants, the continuous nature of the melting transition, and the wave number and frequency dependence of the dynamic structure factor observed in neutron scattering measurements. In addition, we have studied in detail how the dynamics of a 2D fluid evolves from homogeneous (corrugation free) to lattice-fluid limit by changing the strength of the corrugation. We find that corrugation enhances the possibility of observing two-phonon peak in the solid phase and these peaks persist even in the liquid phase, a remarkable property of a lattice-fluid.

For (2), we have studied the combined effects of local anharmonicity and the transverse layer rigidity on the gallery expansion. Simulation results are compared with those obtained within effective medium approximation and a simple and yet successful model called the Catchment Area Model. While in the harmonic limit Vegard's law is obtained when the two intercalants have the same compressibility, we find that inclusion of anharmonicity gives rise to deviations from Vegard's law which increase with the host layer rigidity and the degree of anharmonicity.

For (3), the effect of interfacial disorder on the structure of coherent superlattices has been studied. For a given profile of the interlayer diffusion, various physical quantities such as average bond lengths, specific bond lengths, and change in the coherent strain energy with the degree of interfacial disorder have been calculated. We show that depending on local geometry, interfacial disorder can in fact be energetically favorable.



#### ACKNOWLEDGMENTS

I deeply acknowledge my advisor, Professor S.D. Mahanti, for his continual and patient guidance throughout all stages of this work. Without his understanding, support, and influence on my graduate study this dissertation could not have been finished.

I thank Professor M.F. Thorpe for his advice and collaboration on the problem of disordered interfaces in coherent multilayer systems and the intercalated bilayer problems. I also thank Professor J.S. Chung for collaboration on the problem of gallery expansion of randomly intercalated anharmonic bilayers. I would like to thank Drs. Surajit Sen and Tahir Çağin for their advice and collaboration on the structure of 2-dimensional intercalation compounds. I specially thank Dr. Tahir Çağin for giving me his MD code and for his computer programming skill.

I am grateful to Professors M.F. Thorpe, T.A. Kaplan, C. Foiles, and D. Stump for their service on my Ph.D. guidance committee. I would like to thank Professor J.J. Kovacs, Ms. J. King, and Ms. S. Holland for their assistance.

My special thanks go to my parents for their support and encouragement. I also thank my dear friends: Junghwa Park Bang, Hyunju Chang, Keng Ching Lin and others in this department for their friendship and refreshing conversation. I acknowledge Seonggon Kim for his help in solving all kinds of problems encountered in VAX.

Financial support from Michigan State University, the center for Fundamantal Material research and the National Science Foundation are gratefully acknowledged.

## **Contents**

1	Intr	roduction	1
2	Str	acture of Disorderd Interfaces in Coherent Multilayers	9
	2.1	Introduction	9
	2.2	The Model	10
	2.3	Analytic Solutions and Numerical Simulations	13
		2.3.1 Average Bond Lengths	15
		2.3.2 Specific Bond Lengths	20
		2.3.3 Fluctuations and Strain Energy	23
	2.4	Summary and Conclusion	26
3	Gal	lery Expansion of Randomly Intercalated Anharmonic Bilayers	31
	3.1	Introduction	31
	3.2	The Model and Limiting Cases	35
	3.3	Single Impurity with Anharmonic Cubic Potential	40
	3.4	Effective Medium Theory (EMT)	42
	3.5	Numerical Simulations and Comparison with EMT	48

	3.6	Comparison of Anharmonic Potential Model with Catchment Area	
		Model	52
	3.7	Conclusion	60
4	Str	ucture of 2-Dimensional (2D) Repulsive Screened Coulomb Sys-	
	tem	s/ Model Intercalation Compounds	63
	4.1	Introduction	<b>6</b> 3
	4.2	Physical Systems	64
	4.3	Potential Model	68
	4.4	Details of Molecular Dynamics Simulations	69
	4.5	Structural Properties	70
	4.6	Periodic Domain Wall Model	76
	4.7	Summary and Conclusion	81
5	Me	ting of a Repulsive Screened Coulomb System in 2D - Effect of	r
	Cor	rugation	85
	5.1	Introduction	85
	5.2	Physical Systems	88
	5.3	Thermodynamic Properties	89
		5.3.1 Energy vs. Temperature	90
		5.3.2 Bond Orientational Order Parameter	92
		5.3.3 Angular Susceptibility	94
		5.3.4 Topological Defects	07

		5.3.5	Translational Diffusion Constants	99
	5.4	Sumr	mary and Discussion	103
6	Dyı	namics	of 2D Repulsive Screened Coulomb Fluids on a Cor	ru-
	gate	ed Sur	face	109
	6.1	Introd	luction	109
	6.2	Time	Correlation Functions in Real Space	111
		6.2.1	$G_{ullet}(\mathbf{r},t)$ for Typical Systems	112
		6.2.2	Self-Diffusion Constant	114
	6.3	Intern	nediate Scattering Function	121
	6.4	Incoh	erent Dynamic Structure Factor	128
		6.4.1	Classical Harmonic Oscillator	131
		6.4.2	Corrugation-free System	134
		6.4.3	Effect of a Strong Corrugation Potential	138
		6.4.4	Evolution of $S_s(q,\nu)$ with Strength of Corrugation	141
	6.5	Coher	ent Correlation Functions	144
	6.6	Summ	nary and Discussion	157
7	Mu	ltipho	non Response in 2D Corrugated Systems	161
	7.1	Introd	luction	161
	7.2	Lattic	ee Dynamics	166
	7.3	Phono	on Density of States through Velocity Auto-correlation Functi	on 170
	7.4	Phone	on Density of States through Incoherent Dynamic Structure Fac	ctor174

	7.5	Summary and Conclusion	18
A	Ave	erage length for $\Delta \neq 0$	18
	<b>A.1</b>	$\delta$ - bonds (same layer)	18
	A.2	$ u(\eta)$ - bonds (interlayer)	18
В	EM'	IT in Harmonic Limit	18
C	Mea	an Square Displacement in d-dimension	18

## List of Tables

4.1	Epitaxy angles and primary peak positions of $S(\mathbf{k})$	•	•	•	•	 •	•	76
6.1	Barrier height and diffusion constant for various systems					 _		117

# List of Figures

1.1	A schematic phase diagram in the corrugation strength vs. temperature	3
2.1	Heterostructures with interfacial disorder	11
2.2	Schematic picture of coherent superlattices	16
2.3	Average layer spacings	18
2.4	Average bond length vs. $x_5$ near the interface layers	19
2.5	Specific bond lengths of the interface in the $\delta$ -direction	22
2.6	Specific bond lengths near the interfaces in the $\nu$ -direction	24
2.7	Strain energy as a function of interfacial disorder	27
3.1	Schematic pictures of bilayers with different layer rigidities	34
3.2	Typical average spacings for different interaction potentials	39
3.3	Comparison of the numerical simulations with a single impurity results	43
3.4	Average gallery spacing of a bilayer system	50
3.5	Comparison of the numerical simulations with the results of EMT for	
	different layer rigidities	51
3.6	Comparison of the numerical simulations with the EMT results for	
	different strengths of the anharmonicity	53

3.7	Comparison of the simulation results obtained with the LJ potential
	model with the Catchment Area Model
3.8	Comparison of the simulation results obtained with the LJ potential
	model with the modified Catchment Area Model I
3.9	Comparison of the simulation results obtained with the LJ potential
	model with the modified Catchment Area Model II
4.1	Structure of graphite and staging sequence
4.2	Pair correlation function $g(r)$ for $RbC_{24}$
4.3	Solid structure of $RbC_{24}$ and $RbC_{24.57}$
4.4	Static structure factor $S(\mathbf{k})$ for $RbC_{24}$ at $3K$
4.5	Static structure factor for $RbC_{24}$ at 250K
4.6	Two epitaxy angles vs. various domain sizes
5.1	Potential energy vs temperature
5.2	Bond orientational order parameter vs temperature for systems I and II 93
5.3	Angular susceptibility vs temperature for systems I and II 95
5.4	Temperature dependence of (a) bond orientational order parameter
	for systems II and III and (b) corresponding angular susceptibility 98
5.5	Topological defects in solid and liquid states
5.6	Number of disclinations vs temperature
5.7	Diffusion constant vs temperature
6.1	Trajectories of tagged particles for various strengths of corrugation 115

6.2	Time dependent diffusion coefficient near 250K
6.3	VAF for various values of 2K near 250K
6.4	VAF for various temperatures for $2K = 0.9 \dots 122$
6.5	The self part of the intermediate scattering functions at $q=0.4 \mathring{A}^{-1}$ . 124
6.6	The self part of the intermediate scattering function at $q = 1.2 \mathring{A}^{-1}$ 125
6.7	The self part of the intermediate scattering function at $q = 4 \mathring{A}^{-1}$ 126
6.8	Spectral weight of the incoherent dynamic structure factor of a har-
	monic oscillator at $\nu = 0$ for various values of $2K$
6.9	Spectral weight of the incoherent dynamic structure factor of a har-
	monic oscillator at $\nu = \nu_0$ for various values of $2K \dots 133$
6.10	Incoherent dynamic structure factor vs. frequency for a system with-
	out corrugation potential at 254K
6.11	Diffusion coefficients from $S_s(q, \nu)$ as functions of $q$
6.12	Incoherent dynamic structure factor in the liquid state vs. frequency
	for a strong corrugated potential $(2K = 0.9) \dots \dots$
6.13	Incoherent dynamic structure factor vs. frequency for various strengths
	of the corrugation near 250K for $q=4\mathring{A}^{-1}$
6.14	Intermediate scattering function at $q=0.4 \mathring{A}^{-1}$ near 250K 146
6.15	Intermediate scattering function at $q = 1.2 \text{\AA}^{-1}$ near 250K 147
6.16	Intermediate scattering function at $q = 4\mathring{A}^{-1}$ near 250K 148
6.17	Dynamic structure factor at $q = 0.4 \mathring{A}^{-1} \dots 150$
6.18	Dynamic Structure factor at $q = 1.2 \mathring{A}^{-1}$

6.19	Dynamic Structure factor at $q = 4\mathring{A}^{-1}$
6.20	Longitudinal current correlation functions for $2K = 0 \dots 154$
6.21	Longitudinal current correlation functions for $2K = 0.9 \dots 155$
6.22	Dispersion curve of Brillouin peaks
7.1	Intercalant in-plane mode phonon density of states from Kamitaka-
	hara and Zabel for $RbC_{24}$
7.2	Unit cells of systems I and III
7.3	Dispersion curves for systems I and III
7.4	Phonon density of states through lattice dynamics for the system III. 171
7.5	Fourier transform of velocity auto-correlation function for the systems
	II and III
7.6	$A(q,\nu)$ at $q=4\mathring{A}^{-1}$ for the system II
7.7	$A(q,\nu)$ at $q=0.4 \mathring{A}^{-1}$ for the system II
7.8	$A(q, \nu)$ 's for a harmonic oscillator
7 0	Multiphonon response of the systems I and II

## Chapter 1

### Introduction

A large number of solids occurring in nature or synthesized in a laboratory exhibit a high degree of anisotropy in their physical properties. In some of these solids, the interatomic forces within a layer are usually much stronger than those between the layers. Such solids are characterized as layered solids, typical examples are graphite, layered chalcogenides, and silicate clays. In other types of layered solids, although interatomic forces are not so anisotropic, certain physical properties are highly so. Examples are high- $T_c$  oxide superconductors and artificial superlattices. Many of these layered solids provide a natural arena to study two dimensional (2D) or quasi-2D physical phenomena.

This dissertation focuses on some of the physical properties of layered solids; (1) the structure, melting, and dynamics of 2D systems in the presence of substrate corrugation modelling the properties of binary intercalation systems (chapters 4-7), (2) gallery spacing of ternary intercalation systems (chapter 3), and (3) the structure of layered superlattices in the presence of interfacial disorder (chapter 2). The layered solids with weak interlayer interaction can be made to imbibe guest molecular, ionic and/or atomic species which are sandwiched between the host layers. This process is called intercalation and manifests itself most dramatically as a gross

one-dimensional expansion of the pristine host in a direction normal to the layer planes (denoted commonly as the c-axis). For (1) and (2), the systems we have in mind are binary and ternary intercalated layered solids, the physical properties of the intercalants being of interest in (1).

In binary intercalation compounds, where there is only one type of intercalant inside the gallery, the intercalants form a two dimensional sheet and their structure is determined by a competition between the interaction between the intercalants and the intercalant-host interaction. Depending on the planar density of the intercalants and the strength of the substrate corrugation, one expects to see incommensurate structures characterized by domains and domain walls of various size, or simple commensurate structures. Thermodynamic properties, in particular melting of these 2D solids, and their dynamic properties both in solid and liquid states are areas of great current interest. We address these questions in the present thesis.

In Figure 1.1, we show a generic phase diagram of a 2D system in the presence of corrugation, K being a measure of its strength. Of course the nature of the interparticle potential whether repulsive screened Coulomb (charged intercalants or ionic overlayers) or Lennard Jones types (rare gas atoms on graphite and similar systems), and the density vis-a-vis the period of corrugation play extremely important roles in the detailed nature of the phase diagram. When K=0, one has the problem of melting of a homogeneous 2D solid. In the limit of extremely large K, the particles are localized at the minima of the corrugation potential thereby giving a "lattice-gas" system whose thermodynamic properties are quite different from the K=0 case. We will focus on two aspects of this phase diagram for a repulsive screened Coulomb system; these are shown as two lines in the figure. First, for a given strength of the corrugation, we want to see how the system melts from a

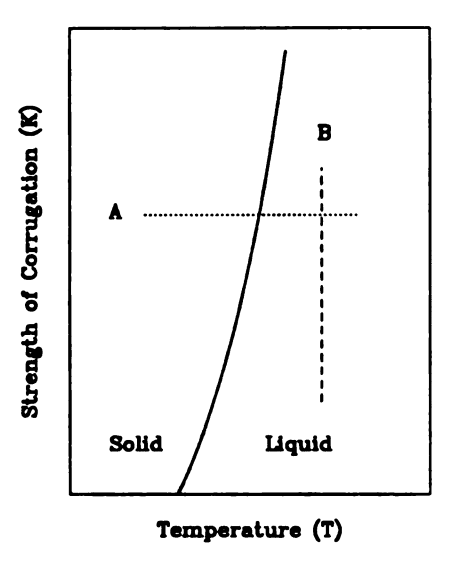


Figure 1.1: A schematic phase diagram in the corrugation strength (K) vs. temperature (T) plane is given for a constant density. The solid curve indicates transition from a solid to a liquid. The study along a dotted line denoted as A gives the T dependence of melting for a fixed strength of the corrugation. The study along the dashed line, B, tells how the liquid dynamics changes with K at a given T.

solid to a liquid and how this differs from the K=0 case (A). Second, for a given temperature, we study how the structure and dynamics of a 2D fluid evolve from a homogeneous fluid to a lattice-fluid (B).

In ternary intercalation compounds, one has a mixture of two types of intercalants inside the gallery. In general, structural, thermodynamic, and dynamic properties of these systems are quite complex. One problem that has been of great interest in recent years is the overall gallery structure of ternary intercalation compounds of the type  $A_{1-x}B_xL$ , where A and B are two types of intercalants of different size and L is the host. One studies the average c-axis spacing as a function of xfor a random configuration of the intercalants and tries to understand the general conditions under which one sees a linear x dependence (Vegard's law) and deviations from this law. In addition, there have been several interesting studies on the ground state structure of 2D random alloys of two different types of atoms with different sizes to see how the system looses its long range order and algebraic decay in correlation as either a function of size mismatch or alloy concentration, the so called size-mismatch melting. Here, we are concerned only with the problem of gallery expansion with specific purpose of identifying the role of anharmonicity and its effects on the Vegard's law.

In coherent superlattices with interfacial disorder, another layered system of great current interest, it is believed that disorder near the interfaces is very important and may profoundly affect the physical properties of these systems. In this thesis, our primary interest is to study the effect of interfacial disorder on the structures of these superlattice systems.

As a first step towards understanding the interfacial structure of coherent multilayer systems, we use harmonic potentials for the interaction of atoms in multilayers (chapter 2). Next, to study the gallery structure of randomly intercalated ternary systems (chapter 3), anharmonic potentials are introduced for the interaction between intercalants and host layers while keeping harmonic potentials for interaction between the host atoms themselves. In these two chapters, we address the T=0 structure, the disorder configuration being frozen. From chapters 4 to 7, we use anharmonic potentials for both intercalant (adsorbate)-host (substrate) interactions and intercalant-intercalant interactions to study the structure and dynamics as a function of temperature. In the following, a brief description of the physical systems and their properties which we have investigated is presented.

Chapter 2 is the study of the effect of interfacial disorder on the structure of

coherent superlattices consisting of l layers of A atoms and m layers of B atoms. For a given profile of the interlayer diffusion, i.e the concentration of A atoms in B rich layers and vice versa, we have been able to obtain several exact results for different structural parameters characterizing the disordered systems in the harmonic limit if we assume that the spring constants associated with the straining of AA, AB, and BB bonds are the same. Various physical quantities such as (1) the average bond lengths both parallel and perpendicular to the growth direction, (2) specific bond lengths such as AA, AB, and BB both near the interface and away from it, and (3) the change in the coherent strain energy with degree of interfacial disorder have been calculated. Our theoretical results can be applied to the multilayers of Ge/Si, GaAs/GaInAs, and GaAs/GaSbAs.

Chapter 3 concerns with the gallery expansion of randomly intercalated anharmonic systems. In these systems one usually has a random alloy of two types of intercalants inside the gallery of host layers, denoted as  $A_{1-x}B_xL$ , and the gallery expansion is monitored as a function of x. These systems are referred to as ternary intercalation compounds. Harmonic models have been extensively studied in bilayers, multilayers, and in 2D and 3D solid solutions. General conditions for the validity of Vegard's law within harmonic theory have been put forward. Whereas some 3D solid solutions show Vegard's law behavior, randomly intercalated layered solids show significant deviations from Vegard's law. It is believed that anharmonicity effects in layered intercalation compounds are significant. Therefore, we have studied the combined effects of local anharmonicity and the transverse layer rigidity on the gallery expansion in ternary intercalated systems, but for the simplicity we have chosen a bilayer model. Unlike the harmonic model, the problem cannot be solved exactly when anharmonicity is present. Numerical simulation results are compared

with analytic calculations within an effective medium approximation and a simple but quite successful "Catchment Area Model".

As discussed above, chapters 2 and 3 are primarily studies of the structure of partially disordered or disordered solids at T=0. For a given random configuration of the intercalants their positions are allowed to relax and the role of disorder on the structure is the main concern. On the other hand, chapters 4 through 7 involve a study of structural, melting, and dynamic properties of a multicomponent system where one of the components is frozen due to its own structural rigidity and the other forms a 2D physical system and shows many interesting phenomena. For example in layered intercalated compounds, the host layer is assumed to be rigid and the intercalants, in addition to a screened Coulomb repulsion, feel the static corrugation potential provided by the host layer (substrates). Because of the complex nature of this system exact solutions are not possible and we have used Molecular Dynamics (MD) simulations to probe their physical properties (see below).

In chapter 4, the structure of domains and domain walls in the low temperature solid phase of stage- $n(\geq 2)$  alkali-metal graphite intercalation compounds (GICs) is studied. For these systems, one can, to a good first approximation, ignore the effects of interlayer intercalant interactions. Since detailed X-ray diffraction measurements have been done in K, Rb, and Cs stage-2 GICs and excellent potential models are available for  $RbC_{24}$ , we focus on this particular system. Our aim is to see whether the low temperature structures obtained from MD simulations can provide a consistent explanation of the in-plane X-ray diffraction measurements. Based on the simulation results we also want to see if simple Periodic Domain Wall (PDW) models can be constructed to explain the dominant features of the X-ray diffraction experiments in these GICs.

Chapter 5 is on the melting and freezing transitions of a 2D system consisting of charged particles interacting with a repulsive screened Coulomb (Yukawa) potential. The motivation for this work is two-fold. One is to compare our MD results with the experimental data in  $RbC_{24}$  and the other to study in general the role of corrugation on the melting transitions of a 2D solid. In particular, we have investigated the role of an incommensurate substrate corrugation potential of six-fold symmetry on the melting transitions by probing the temperature dependence of the bond orientational order parameter and its conjugate susceptibility. Other physical quantities such as energy, diffusion constant, and the density of local topological defects have been monitored through the transition region to find out the detailed nature of the phase transition.

In chapter 6, we discuss the dynamics in the liquid phase of a 2D screened Coulomb system by varying the strength of the corrugation potential. Mean square displacement, velocity-auto correlation function, intermediate scattering function, and dynamic structure factor are examined. Neutron scattering studies of the dynamic structure factor at large wave numbers from a 2D fluid on a corrugated substrate show an extremely narrow resolution limited central peak on top of a broad central peak, and a broad finite frequency peak. We have attempted to reproduce all these features using MD simulations. Furthermore, since we can tune the strength of the corrugation potential, we study the evolution of these spectral features as a function of the corrugation strength and scattering wave number.

Finally, in chapter 7, we discuss the effects of corrugation on the phonon density of states (PDOS) associated with in-plane vibrational excitations of the intercalants in the solid phase. At very low temperatures, in the absence of corrugation, the primary excitations are phonons of a triangular lattice. In the presence of corrugation,

the ground state structure of RbC24 can be approximated by a PDW solid with a few "local" defects. The excitations of pure PDW solid which has a commensurate ground state structure have a gap determined by the strength of the corrugation potential. One important question we want to address is how the PDOS changes when we go from the commensurate to the incommensurate system. PDOS associated with the in-plane vibrational dynamics of intercalants in corrugated 2D systems such as GICs obtained from inelastic neutron scattering (INS) measurements at large wave numbers show a characteristic two-peak structure. This two-peak structure was explained previously by one phonon density of states, the phonon frequencies having been obtained from an unscreened Coulomb interaction model. Earlier MD simulation studies also supported this picture but with a screened Coulomb model. The fact that the two completely different interaction models could give the same PDOS implies that something is basically wrong with these explanations. Using MD simulations and screened Coulomb model which has been extremely successful for alkali metal GICs, we propose to clear up this confusion and provide a correct understanding of the INS experiments.

### Chapter 2

# Structure of Disorderd Interfaces in Coherent Multilayers

### 2.1 Introduction

With molecular beam epitaxy (MBE), one can routinely grow coherent strained superlattices (CSLs) with l layers of A atoms and m layers of B atoms repeated p times, denoted by  $(A_lB_m)_p$  [1]. In thin (small l and m) epitaxial layers the lattice mismatch between pure A and B layers is commonly accommodated by distortion of the unit cells, resulting in strained pseudomorphic structures [2, 3]. Some of the superlattices of current interest are lattice mismatched heterostructures for electronic and optoelectronic device fabrications, for example  $(Si_lGe_m)_p$  [4] and  $InP/In_{1-x}Ga_xAs$  [5] superlattices. In the latter system, one can in fact control the lattice mismatch and hence the coherency strain by controlling x, x = 0.47 giving the perfect lattice match with InP.

For ideal devices one should not have interlayer diffusion across the interface (to avoid interfacial disorder) and misfit dislocations [6]. The misfit dislocations can be avoided by growing thin superlattices but it is generally difficult to avoid interfacial disorder [7]. Recent direct imaging studies of interfacial structure in an ultrathin

(Si<sub>4</sub>Ge<sub>8</sub>)<sub>24</sub> superlattice based on Z-contrast transmission electron microscopy [4, 8] show that Si-layers contain a large concentration of Ge atoms. In  $InP/In_{1-x}Ga_xAs$ [5] superlattices it is in fact possible to introduce interlayer diffusion (hence interfacial disorder) of In and Ga ions in the presence of Zn ions. Interfacial disorder (IFD) in lattice mismatched systems leads to bond length fluctuations and hence destroys the ideal physical characteristics of the device. Also under growth conditions if IFD reduces the strain, then a disordered interface will be energetically favorable. Thus it is important to understand the effects of IFD on the structural properties of superlattice systems. In addition to the semiconducting superlattices, there has been also a great deal of interest in recent years in magnetic multilayers showing giant magnetoresistance (GMR) (Pratt et al. [9] and Levy et al. [10]). It is believed that the observed GMR [10] is sensitive to IFD. In this chapter, we address the questions which deal with the structure of disordered interfaces by studying the effects of IFD in  $(A_l B_m)_p$  superlattices [11] on various physical characteristics such as (1) the average bond lengths both parallel and perpendicular to the growth direction, (2) specific bond lengths such as AA, AB, and BB both near the interfaces and away from them, and (3) change in the coherency strain energy with degree of IFD.

### 2.2 The Model

The model we have studied is illustrated in Figure 2.1. The bottom panel is a Z-contrast scanning transmission electron microscopy image of a nominal  $(Si_4Ge_8)_{24}$  superlattice [4] grown along [110] direction showing Si and Ge multilayers. The middle panel is a schematic picture of CSLs with disordered interfaces. The white and solid circles stand for two different types of atomic layers without mixing and the

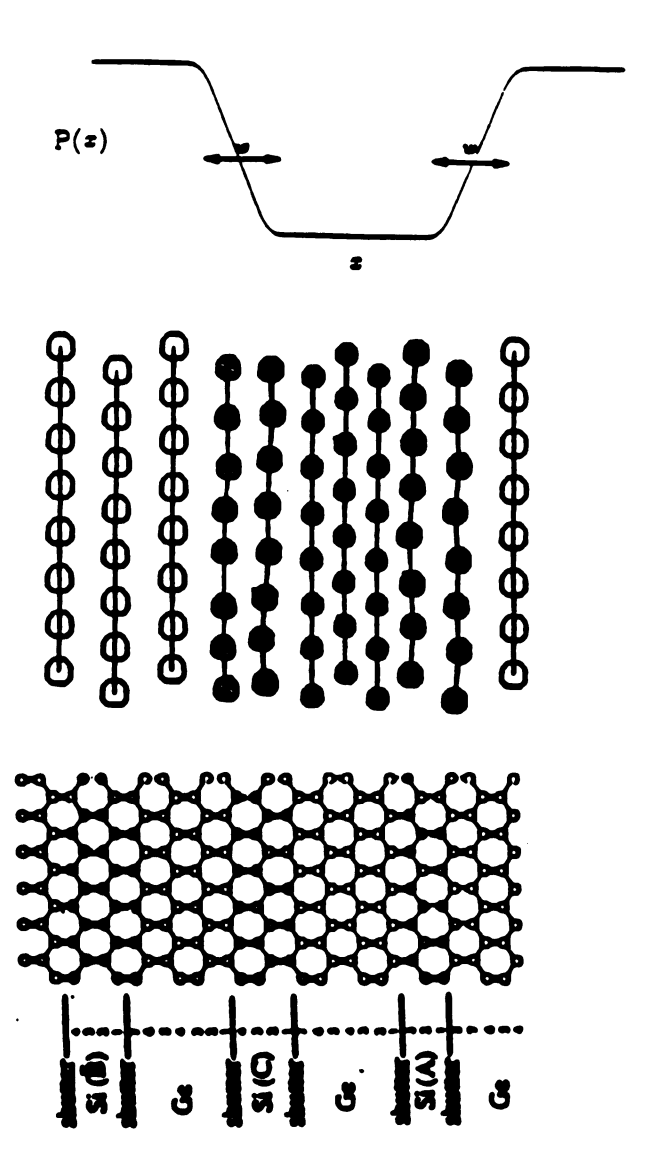


Figure 2.1: Heterostructures with interfacial disorder: The bottom panel is Z-contrast scanning transmission electron microscopy image of a nominal  $(Si_4Ge_8)_{24}$  superlattice [4]. The middle panel is a schematic picture of disordered interfaces, the shaded circles representing the disordered layers. The top panel shows a continuous profile p(x) of the concentration of one type of atom; w is a measure of the width of the disordered region.

shaded circles represent the disordered layers whose layer stoichiometry depends on the degree of mixing of two types of atoms. In the top panel we plot the concentration profile of one type of atoms,  $x_{\mu}$ , for different layers ( $\mu$ ) treated as a continuous function p(x); w is a measure of the width of the disordered region.

For simplicity we will consider a 2-dimensional superlattice although our results are general and can be applied to the 3-dimensional case. The energy associated with the distortion of the individual bonds from their natural lengths  $L^0_{ij}$  is given by

$$V = \frac{1}{2} \sum_{\langle i,j \rangle} K_{ij} (|\mathbf{L}_{ij}| - L_{ij}^{0})^{2}, \tag{2.1}$$

where  $K_{ij}$  can be  $K_{AA}$ ,  $K_{BB}$ , and  $K_{AB}$  and  $L^0_{ij}$  can be  $L^0_{AA}$ ,  $L^0_{BB}$ , and  $L^0_{AB}$  [12]. The summation goes over all nearest neighbor bonds ij and the angular brackets imply that the nearest neighbor sites are only counted once. We introduce a reference lattice ( $\bar{\mathbf{L}}$ ) that is a perfectly undistorted triangular network and assume a small displacement  $\mathbf{u}_i$  associated with the site i.

$$\mathbf{L}_{ij} = \bar{\mathbf{L}} + [(\mathbf{u}_i - \mathbf{u}_j) \cdot \hat{R}_{ij}] \hat{R}_{ij}, \tag{2.2}$$

where  $\bar{\mathbf{L}}$  can take three possible values depending on ij and  $\hat{R}_{ij}$ 's are unit vectors along the undistorted triangles of the reference lattice. By using harmonic approximation and minimizing the energy (Eq. (2.1)), we find that

$$\sum_{j} K_{ij} [(\mathbf{u}_{i} - \mathbf{u}_{j}) \cdot \hat{R}_{ij}] \hat{R}_{ij} - \sum_{j} K_{ij} (L_{ij}^{0} \hat{R}_{ij} - \mathbf{\bar{L}}) = 0.$$
 (2.3)

Eq. (2.3) can be rewritten as follows:

$$\vec{M} \cdot \mathbf{u} = \mathbf{F},\tag{2.4}$$

where  $\mathbf{F} = K_{ij}(L_{ij}^0 \hat{R}_{ij} - \mathbf{\bar{L}})$ .  $\mathbf{\bar{M}}$  is a random matrix and  $\mathbf{F}$  is a column vector with random elements describing the deviation of the natural bond lengths from that of the reference lattice.

When  $K_{ij} = K$  (i.e. when all the nearest neighbor interactions are the same), M becomes a nonrandom matrix and

$$\mathbf{u} = \mathbf{\ddot{G}} \cdot \mathbf{F},\tag{2.5}$$

where  $\vec{G}$  is the usual Green function for the perfect system. In Eq. (2.5) disorder appears only through the natural bond lengths  $L_{ij}^0$  occurring in  $\mathbf{F}$ . Knowing  $\mathbf{u}$  we can obtain the bond lengths  $L_{ij}$ ,

$$\mathbf{L}_{ij} = \bar{\mathbf{L}} + K \sum_{k,n} (\vec{G}_{in} - \vec{G}_{jn}) \cdot (\hat{R}_{nk} L_{nk}^0 - \bar{\mathbf{L}}). \tag{2.6}$$

Now, we can calculate average bond lengths, their fluctuation, and strain energy.

# 2.3 Analytic Solutions and Numerical Simulations

Up to this point, all results are formal and can be applied to any system. Now, we will describe how to interpret Eq. (2.6) for the CSLs with a specific lattice structure i.e. triangular lattice. First,  $\bar{\mathbf{L}}$  has two distinct directions; one ( $\delta$ ) is along the layers and the other ( $\nu$  or  $\eta$ ) connects neighboring layers. Second, each layer has different average concentrations of A and B atoms. Here, we use Greek letters to denote the layer index. Therefore, i can be rewritten as  $\mu n$  which corresponds to the nth atom in the  $\mu$ th layer. Concentration of large atoms B in the layer  $\mu$  is denoted by  $x_{\mu}$ . The layer concentration of small atoms A is therefore  $1 - x_{\mu}$ . For the CSLs with ideal interfaces,  $x_{\mu} = 1(0)$  for the layers with all B(A) atoms.

In the absence of IFD and in the limit of uniform force constants, i.e.  $K_{ij} = K$ ,  $\bar{\mathbf{L}}$  can be determined by demanding that there is no net macroscopic force on an imaginary line through the reference lattice. From Eq. (2.3) when  $K_{ij} = K$ ,

$$K\sum_{ij}(\bar{\mathbf{L}} - L_{ij}^0 \hat{R}_{ij}) = 0. (2.7)$$

Therefore the nearest neighbor distance of the underlying virtual crystal for an arbitrary direction is obtained from the above equation.

We introduce a projection operator  $\sigma_{\mu n}$  to deal with the random variable  $L_{ij}^0$ .  $\sigma_{\mu n} = 1(-1)$  for an A(B) atom in the  $\mu$ th layer. The mean value of  $\sigma_{\mu n}$  for a given layer  $\mu$  is

$$\langle \sigma_{\mu n} \rangle = \sum_{n} \sigma_{\mu n} / N = 1 - 2x_{\mu}, \tag{2.8}$$

where N is the number of sites in the layer. For the sake of simplicity we will use only the layer index  $\mu$  instead of  $\mu n$  to describe  $\sigma_{\mu n}$  since  $\langle \sigma_{\mu n} \rangle$  is independent of the site index n. However, when the random variable  $\sigma_{\mu}$  appears before taking an average, its n dependence is implicitly assumed. Consider a nearest neighbor bond between atoms in two layers  $\mu$  and  $\xi$ . The natural bond length is given by

$$L^{0}_{\mu,\xi} = \frac{1+\sigma_{\mu}}{2} \frac{1+\sigma_{\xi}}{2} L^{0}_{AA} + \frac{1-\sigma_{\mu}}{2} \frac{1-\sigma_{\xi}}{2} L^{0}_{BB} + \left[ \frac{1+\sigma_{\mu}}{2} \frac{1-\sigma_{\xi}}{2} + \frac{1-\sigma_{\mu}}{2} \frac{1+\sigma_{\xi}}{2} \right] L^{0}_{AB}.$$
 (2.9)

If we take  $\Delta \equiv L_{AA}^0 + L_{BB}^0 - 2L_{AB}^0 = 0$  i.e.  $L_{AB}^0$  is the arithmetic mean of  $L_{AA}^0$  and  $L_{BB}^0$ , then Eq. (2.9) reduces to

$$L^{0}_{\mu,\xi} = \left(\frac{1+\sigma_{\mu}}{4} + \frac{1+\sigma_{\xi}}{4}\right)L^{0}_{AA} + \left(\frac{1-\sigma_{\mu}}{4} + \frac{1-\sigma_{\xi}}{4}\right)L^{0}_{BB}. \tag{2.10}$$

An important difference between Eq. (2.9) and Eq. (2.10) is that they lead to different reference lattices; the former gives an isosceles triangle whereas the latter gives an equilateral one. As a result, when  $\Delta=0$ , we need only one topological parameter to describe the rigidity of the reference system which is an equilateral triangle. Also the resulting equations for different physical quantities are much simpler. From here on we will discuss our results only for the case  $\Delta=0$  and results for  $\Delta\neq 0$  will be given in Appendix A.

### 2.3.1 Average Bond Lengths

First, we calculate the average distance  $\langle L_{\mu,\xi} \rangle$  for inter- and intra-layer spacing denoted as  $\nu$  (or  $\eta$ ) and  $\delta$  directions, respectively. We find for the average intralayer bond length

$$\langle L_{\mu,\mu} \rangle_{\delta} = (1 - X) L_{AA}^{0} + X L_{BB}^{0}, \tag{2.11}$$

where X is the global concentration of B atoms over the entire CSLs i.e.  $X = \sum_{\mu} x_{\mu}/N_l$ , where  $N_l$  is the total number of layers. Along  $\nu$  (or  $\eta$ ) direction

$$\langle L_{\mu,\xi} \rangle_{\nu} = (1 - x_{\mu,\xi}) L_{AA}^{0} + x_{\mu,\xi} L_{BB}^{0}, \qquad (2.12)$$

where

$$x_{\mu,\xi} = \frac{x_{\mu} + x_{\xi}}{2}. (2.13)$$

Thus the average bond length along the layer (coherency strain direction) depends only on the global concentration X of B atoms due to the requirement of coherency whereas that between the layers depend on the local concentration. This asymmetry is a characteristic of the CSL structure and is not found in random alloy systems [12].

In the absence of IFD,  $x_{\mu}$  has a steplike structure, 0 in A multilayers and 1 in B multilayers whereas in the presence of IFD this steplike behavior of  $x_{\mu}$  changes to a smooth function of  $\mu$  near the interfaces (see the top panel of Figure 2.1). Numerical simulations with conjugate gradient method have been done for the system  $(A_lB_m)_p$  with l=m=p=5 and with 200 atoms in each layer (see Figure 2.2 where one unit of  $A_5B_5$  is shown). We have chosen  $L_{AA}^0=1$  and  $L_{BB}^0=1.04$ ; a 4% lattice mismatch is typical for semiconductor alloys. Each layer can be denoted as  $A_{1-x_{\mu}}B_{x_{\mu}}$  with  $x_{\mu}$  changing from one layer to the other. For simulation, we considered IFD to be

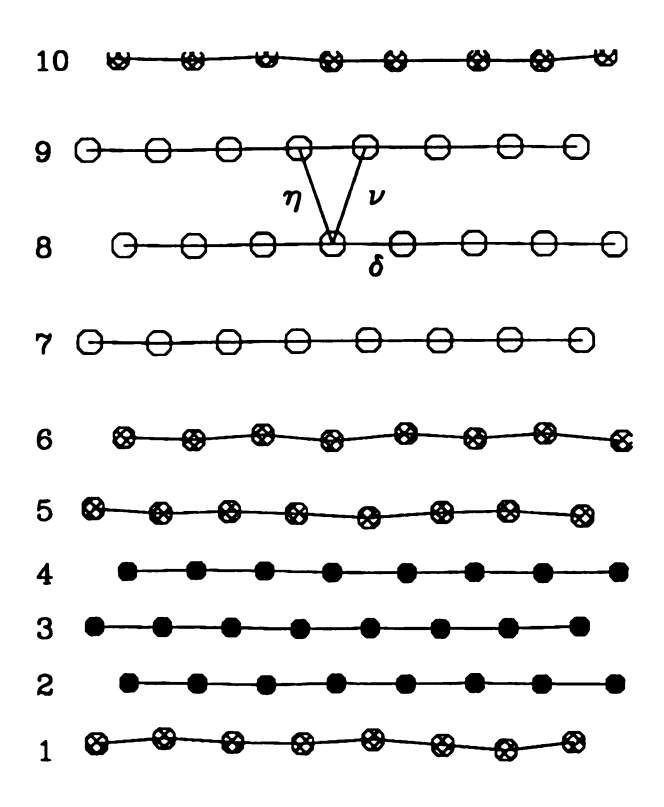


Figure 2.2: A schematic picture of a coherent superlattice with disordered interfaces. The multilayer structure is  $(A_5B_5)_5$ . Layers 2, 3, and 4 have all A atoms. Layers 7, 8, and 9 have all B atoms. Layers 5, 6 and 10, 1 are interface layers, shaded circles representing the disordered layers.  $\delta$ ,  $\nu$ , and  $\eta$  are directional vectors we use for the reference lattice.

confined to the two interfacial layers only. In this case,  $x_{\mu}=0$  for  $\mu=2,3,4$  and  $x_{\mu}=1$  for  $\mu=7,8,9$ . The 5th and the 6th layers (as well as the 1st and the 10th layers) are interface layers and we have considered a situation where the A atoms from the 5th layer and B atoms from the 6th layer are mixed but the total number of A and B atoms are conserved within the two adjacent layers. Because of the conservation of the number of each type of atoms, we have  $1-x_5+1-x_6=1$   $(x_5+x_6=1)$  for A (B) atoms respectively. Thus the 5th (6th) layer forms a random alloy  $A_{1-x_5}B_{x_5}$   $(A_{1-x_6}B_{x_6}\equiv A_{x_5}B_{1-x_5})$ .

Figure 2.3 gives the projection of average interlayer spacings  $\langle L_{\mu,\mu+1} \rangle_y$  along the layer growth direction (denoted as y) as a function of the layer index  $\mu$  for several profiles of IFD i.e. from no interlayer diffusion (perfectly clean interface,  $x_5 = 0$  and  $x_6 = 1$ ) to complete exchange (layer interchange,  $x_5 = 1$  and  $x_6 = 0$ ). The inside four different curves are for different degrees of interface mixing i.e.  $x_5 = 0.1$ , 0.3, 0.5, and 0.7. In all cases, numerical simulations (denoted by symbols) and analytic calculations (solid lines) agree very well.

To see how the average interlayer bond length (or equivalently the average bond length joining atoms in the layers  $\mu$  and  $\mu + 1$ ) changes with IFD, let us look at Figure 2.4. The lowest  $(\langle L_{3,4} \rangle)$  and the topmost  $(\langle L_{7,8} \rangle)$  lines are independent of  $x_5$  simply due to the absence of any interlayer mixing. Similarly,  $\langle L_{2,3} \rangle$  and  $\langle L_{8,9} \rangle$  are also independent of  $x_5$  and have not been shown in the figure. The linear increase (decrease) of  $\langle L_{4,5} \rangle$  ( $\langle L_{6,7} \rangle$ ) can be easily understood from Eqs. (2.12) and (2.13) by noting that  $x_4 = 0, x_7 = 1$ , and  $x_6 = 1 - x_5$ . One interesting result is that the average bond length between layers 5 and 6  $\langle L_{5,6} \rangle$  does not depend on the concentration  $x_5$  although these are interface layers and the concentration of B atoms in each layer changes. This is because the average bond length (Eq. (2.12))

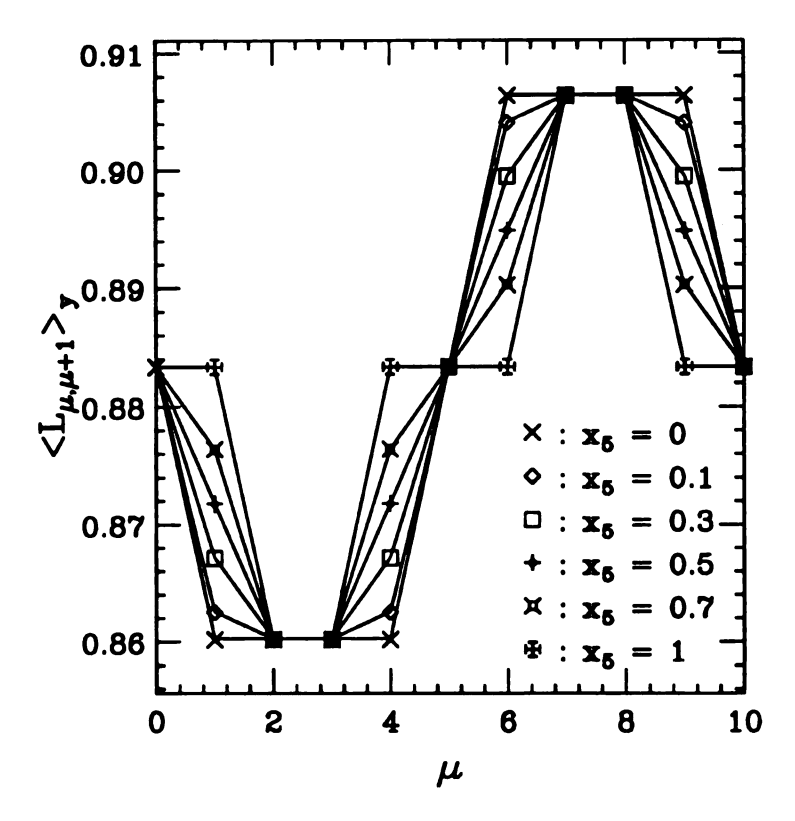


Figure 2.3: The same system as Figure 2.2. Comparison between analytic calculations (solid lines) and numerical simulations (symbols) of average layer spacing  $\langle L_{\mu,\mu+1} \rangle_y$  as a function of the layer index  $\mu$  for the multilayer  $(A_5B_5)_5$ .  $x_5=0$  means perfect interface whereas  $x_5=1$  implies the interchange of two adjacent interface layers.

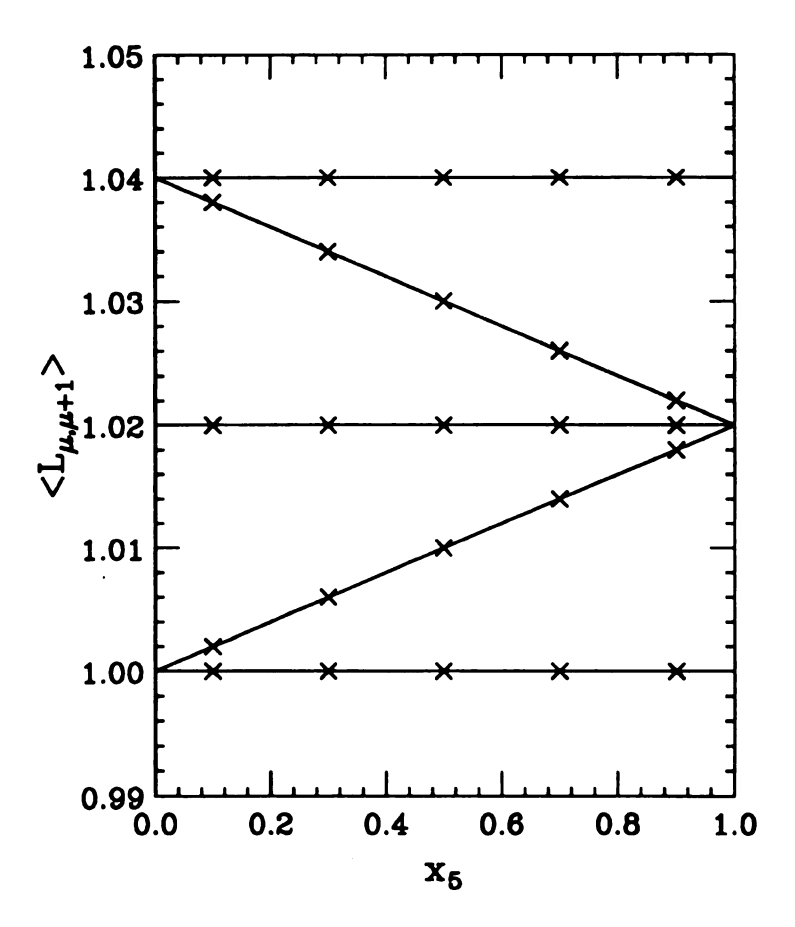


Figure 2.4: The same system as Figure 2.2. Each line corresponds to an average bond length  $\langle L_{\mu,\mu+1} \rangle$  between layer  $\mu$  and  $\mu+1$ ,  $x_5$  is the concentration of B atoms in the layer 5. From the bottom to top  $\mu$  is 3, 4, 5, 6, and 7. The  $\times$  symbols are numerical simulation results.

depends on the average concentration (Eq. (2.13)) of the two layers and since the change in concentration of the atoms occurs only through the exchange of A and B atoms within the two layers  $2x_{5,6} = x_5 + x_6 = 1$ . Therefore, there is no change in the average concentration  $(x_{5,6})$  between the interface layers resulting in  $(L_{5,6})$  being independent of IFD. Each layer follows Vegard's law [13] and numerical simulations and analytic calculations agree very well.

#### 2.3.2 Specific Bond Lengths

We have calculated specific bond lengths both along (denoted as  $\delta$ -bond) and between ( $\nu$  bond) the layers. For the  $\delta$ -bonds (same layer), we find

$$\langle L_{\mu,\mu} \rangle_{\delta}^{AA} = \langle \bar{L} \rangle + a^{**} x_{\mu} (L_{AA}^{0} - L_{BB}^{0})$$
 (2.14)

$$\langle L_{\mu,\mu} \rangle_{\delta}^{BB} = \langle \bar{L} \rangle - a^{**} (1 - x_{\mu}) (L_{AA}^{0} - L_{BB}^{0})$$
 (2.15)

$$\langle L_{\mu,\mu} \rangle_{\delta}^{AB} = \langle \bar{L} \rangle - a^{**} (\frac{1}{2} - x_{\mu}) (L_{AA}^{0} - L_{BB}^{0}).$$
 (2.16)

Here, the mean length  $\langle \bar{L} \rangle = (1-X)L_{AA}^0 + XL_{BB}^0$  is determined only by the global concentration X due to the coherency requirement along the  $\delta$ -direction. The parameter  $a^{**}$  [14, 15, 16] in the above equations characterizing the topological rigidity of the reference lattice is given by

$$a^{**} = \frac{1}{z} \sum_{\gamma \gamma'} \sum_{\mathbf{Q}} \sin(\mathbf{Q} \cdot \gamma) [\gamma \cdot \overrightarrow{D} (\mathbf{Q})^{-1} \cdot \gamma'] \sin(\mathbf{Q} \cdot \gamma'), \tag{2.17}$$

where z is the number of the nearest neighbor atoms and  $\gamma$  and  $\gamma'$  stand for the nearest neighbor directional vectors  $(\pm \delta, \pm \nu \text{ and } \pm \eta)$  of the triangle describing the reference lattice. It is easy to see that  $\langle \bar{L} \rangle = (1 - x_{\mu})^2 \langle L_{\mu,\mu} \rangle_{\delta}^{AA} + x_{\mu}^2 \langle L_{\mu,\mu} \rangle_{\delta}^{BB} + 2x_{\mu}(1 - x_{\mu}) \langle L_{\mu,\mu} \rangle_{\delta}^{AB}$ . Furthermore, because of the assumption  $\Delta = 0$ , we have an additional relation  $\langle L_{\mu,\mu} \rangle_{\delta}^{AA} + \langle L_{\mu,\mu} \rangle_{\delta}^{BB} - 2\langle L_{\mu,\mu} \rangle_{\delta}^{AB} = 0$ .

Figure 2.5 gives the  $x_{\mu}$  dependence of different normalized intralayer spacings for the layers 5 and 6. When  $x_5 = 0$ ,  $\langle L_{5,5} \rangle_{\delta}^{AA} = \langle L_{6,6} \rangle_{\delta}^{BB}$  and these depend only on  $\langle \bar{L} \rangle$ . Our choice of l = m = 5 gives the global concentration X = 0.5. Therefore  $\langle \bar{L} \rangle$  is 0.5 in the normalized length. Here, we introduce a normalized bond length such that

$$\langle d_{\mu,\xi} \rangle_{\delta}^{AA} = \frac{\langle L_{\mu,\xi} \rangle_{\delta}^{AA} - L_{AA}^{0}}{L_{BR}^{0} - L_{AA}^{0}}.$$
 (2.18)

When  $x_5=0$ , the AA(BB) bonds in the 5th (6th) layer are already expanded (contracted) to form a CSL. Also,  $\langle d_{\mu,\mu} \rangle_{\delta}^{AA}(\langle d_{\mu,\mu} \rangle_{\delta}^{BB})$  is never equal to 0(1) which reflects a characteristic (or requirement) of the CSL as we see in Figure 2.5. Let us try to understand the  $x_5$  dependence of  $\langle d_{5,5} \rangle_{\delta}$  in Figure 2.5. When B atoms from the 6th layer go into the 5th layer making  $x_5 \neq 0$ , the stretched AA bonds tend to go towards their natural bond lengths  $L_{AA}^0$ . This is why  $\langle d_{5,5} \rangle_{\delta}$  decreases as  $x_5$  increases. On the other hand, when  $x_5=0$ , the layer 6  $(A_{1-x_6}B_{x_6}\equiv A_{x_5}B_{1-x_5})$  is filled with all B atoms which are contracted to match with layers with A atoms. As  $x_5$  increases i.e. atoms with small size come into this layer, large atoms can relax toward their natural lengths, causing an increase in  $\langle d_{6,6} \rangle_{\delta}$  with  $x_5$ .

For the  $\nu$ -bonds (interlayer bonds) connecting two adjacent layers with concentrations  $x_{\mu}$  and  $x_{\xi}$ , we obtain

$$\langle L_{\mu,\xi} \rangle_{\nu}^{AA} = \langle L_{\mu,\xi} \rangle_{\nu} + a^{**} x_{\mu,\xi} (L_{AA}^{0} - L_{BB}^{0}),$$
 (2.19)

$$\langle L_{\mu,\xi} \rangle_{\nu}^{BB} = \langle L_{\mu,\xi} \rangle_{\nu} - a^{**} (1 - x_{\mu,\xi}) (L_{AA}^{0} - L_{BB}^{0}),$$
 (2.20)

$$\langle L_{\mu,\xi} \rangle_{\nu}^{AB} = \langle L_{\mu,\xi} \rangle_{\nu} - a^{**} (\frac{1}{2} - x_{\mu,\xi}) (L_{AA}^{0} - L_{BB}^{0}),$$
 (2.21)

where  $\langle L_{\mu,\xi} \rangle_{\nu}$  and  $x_{\mu,\xi}$  have been defined in Eqs. (2.12) and (2.13), respectively. The average interlayer bond lengths are also determined by the same single topological rigidity parameter  $a^{**}$ . In the  $\nu$  or  $\eta$  direction, when  $x_{4,5} = 0$  i.e. when  $x_5 = 0$ , the

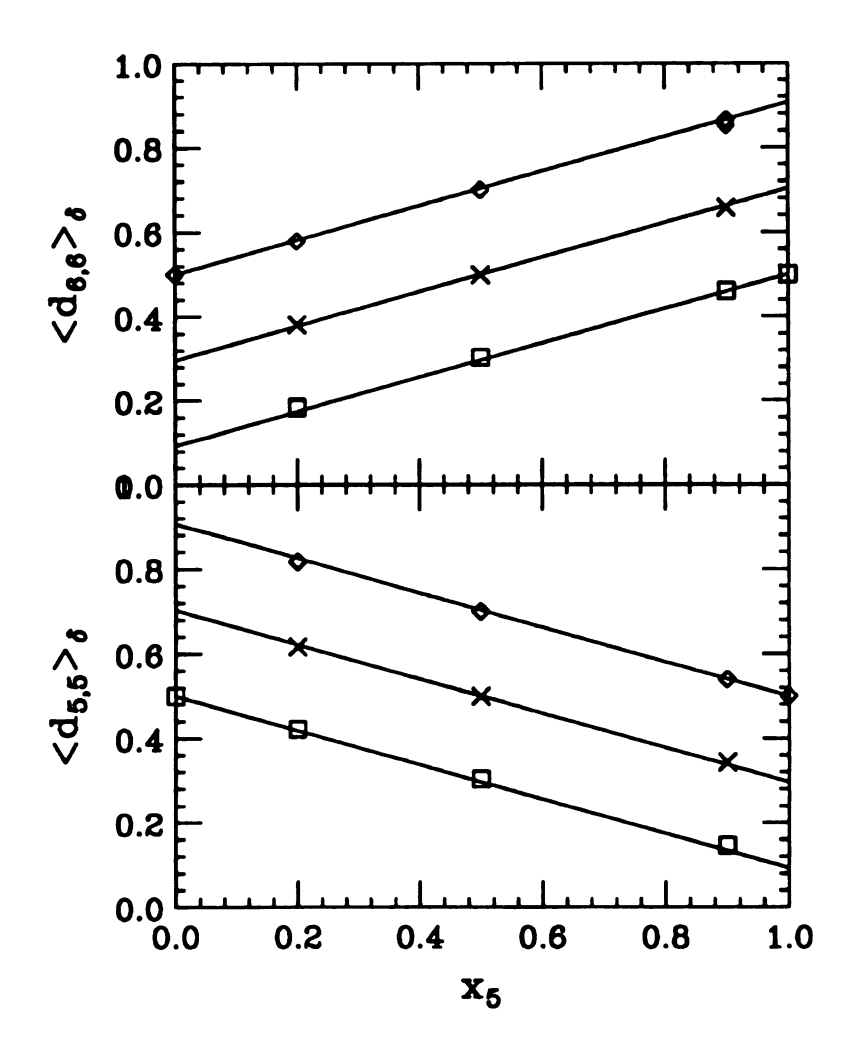


Figure 2.5: Normalized average intralayer bond length for the interface layers as a function of  $x_5$ . Three curves of each set from top to bottom correspond to  $BB(\diamond)$ ,  $AB(\times)$ , and  $AA(\square)$  bond lengths.

AA bond is unstrained (see Figure 2.6). Here,  $x_4$  is always equal to 0 because we are considering the interface mixing only between the layers 5 and 6, i.e. the layer 4 has all A atoms. Therefore, possible bonds between the layers 4 and 5 are only of the AA and AB type. Similarly, the layer 7 has all B atoms and bonds between layers 6 and 7 are only of BB and AB type. As B(A) atoms come into the layer with all A(B) atoms, interlayer bond length  $\langle d_{4,5} \rangle_{\nu}$  ( $\langle d_{6,7} \rangle_{\nu}$ ) becomes bigger (smaller) which means that the AA(BB) bond expands (contracts). Therefore,  $\langle d_{4,5} \rangle_{\nu}^{AA}$  increases as the concentration of B atoms in the 5th layer increases. The  $x_{4,5}$  dependence of average AB bond length can be explained similarly. Of course, all combinations are possible across the layers 5 and 6. However,  $\langle d_{5,6} \rangle_{\nu}$  for AA, AB, and BB bonds are independent of the  $x_{5,6}$  and can be explained by the same reasoning as discussed for the Figure 2.4 in the previous section.

#### 2.3.3 Fluctuations and Strain Energy

Next, we calculate the global bond length fluctuations and strain energies associated with the bonds in the  $\delta$ - and  $\nu$ -directions, respectively. In particular, we study how the strain energy depends on the degree of IFD and  $a^{**}$  and investigate under what conditions strain energy favors IFD.

For fluctuations of bond length distribution, we find

$$\langle L^{2} \rangle_{\delta} - \langle L \rangle_{\delta}^{2} = a^{**} (1 - a^{**}) (L_{AA}^{0} - L_{BB}^{0})^{2} \sum_{\mu=1}^{l+m} \frac{x_{\mu} (1 - x_{\mu})}{2(l+m)}, \qquad (2.22)$$

$$\langle L^{2} \rangle_{\nu} - \langle L \rangle_{\nu}^{2} = \langle L^{2} \rangle_{\eta} - \langle L \rangle_{\eta}^{2}$$

$$= a^{**} (1 - a^{**}) (L_{AA}^{0} - L_{BB}^{0})^{2} \sum_{\mu=1}^{l+m} \frac{x_{\mu} (1 - x_{\mu}) + x_{\mu-1} (1 - x_{\mu-1})}{4(l+m)}. \quad (2.23)$$

We see that bond length fluctuations over the entire CSLs are same for the  $\delta$  and  $\nu$  directions in spite of the coherency constraint along the  $\delta$ -direction. The specific bond length fluctuations for AA, BB, and AB are also found to be the same. The

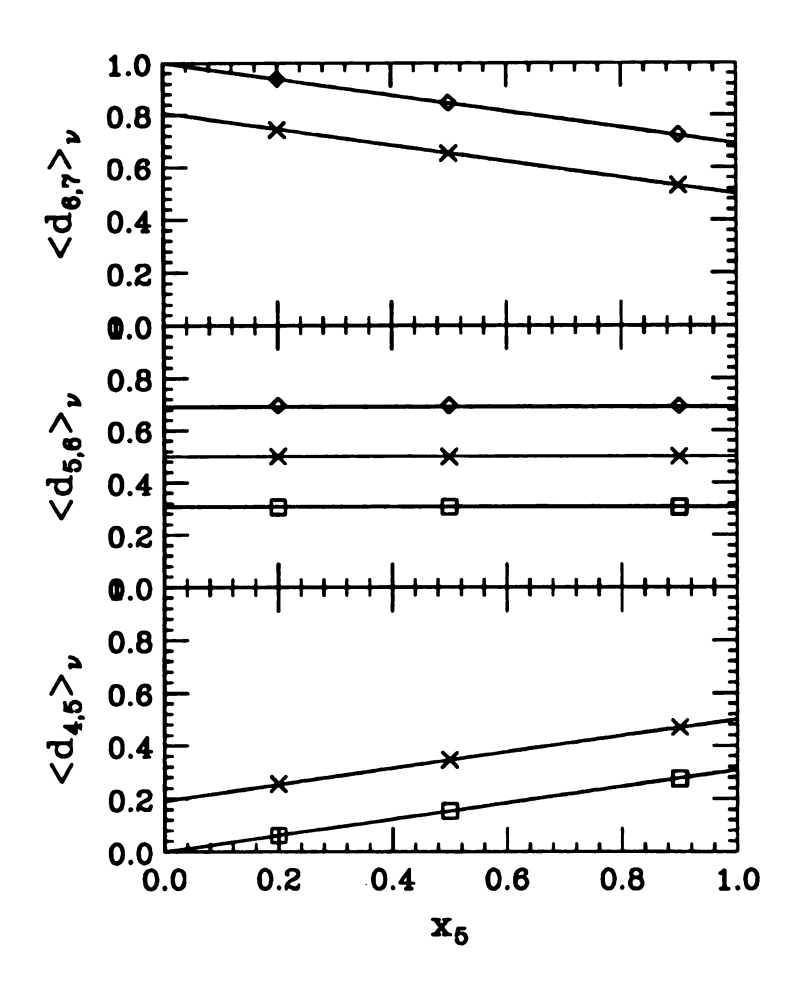


Figure 2.6: Specific bond lengths near the interfaces for  $\nu$ -direction vs.  $x_5$  concentration of B atoms in the layer 5. The symbols stand for the same as Figure 2.5 i.e.  $BB(\diamond)$ ,  $AB(\times)$ , and  $AA(\square)$  bond lengths.

average strain energy per bond is given by

$$\mathcal{E} = \frac{K(L_{AA}^0 - L_{BB}^0)^2}{2 \cdot 3} (\mathcal{E}_{\delta} + \mathcal{E}_{\nu} + \mathcal{E}_{\eta}), \tag{2.24}$$

where

$$\mathcal{E}_{\delta} = \frac{1}{l+m} \sum_{\mu=1}^{l+m} \left[ (X - x_{\mu})^2 + (1 - a^{**}) \frac{x_{\mu}(1 - x_{\mu})}{2} \right], \tag{2.25}$$

$$\mathcal{E}_{\nu} = \mathcal{E}_{\eta} = \frac{(1 - a^{**})}{l + m} \sum_{\mu=1}^{l+m} \frac{x_{\mu}(1 - x_{\mu}) + x_{\mu-1}(1 - x_{\mu-1})}{4}.$$
 (2.26)

Combining Eqs. (2.24)-(2.26), we obtain

$$\mathcal{E} = \frac{K}{2} (L_{AA}^0 - L_{BB}^0)^2 \frac{1}{l+m} \sum_{\mu=1}^{l+m} \left[ \frac{z_c}{z} (X - x_\mu)^2 + \frac{x_\mu (1 - x_\mu)}{2} (1 - a^{**}) \right], \quad (2.27)$$

where  $z_c$  is the coordination number in the  $\delta$  direction (along the layer) and z is the number of nearest neighbors.

If we describe the interfacial diffusion by a continuous function p(x) of width w (see Figure 2.1), we obtain

$$\mathcal{E} = \frac{K}{2} (L_{AA}^0 - L_{BB}^0)^2 \left[ \frac{z_c}{z} (\langle x^2 \rangle - X^2) + \frac{X - \langle x^2 \rangle}{2} (1 - a^{**}) \right], \tag{2.28}$$

where  $\langle x^n \rangle = \int x^n p(x) dx$ . Thus the difference in the strain energy between the multilayer with perfect interface (w=0) and that with IFD is given by

$$\mathcal{E}_{w=0} - \mathcal{E}_{w} = \frac{K}{2} (L_{AA}^{0} - L_{BB}^{0})^{2} \left[ \frac{z_{c}}{z} - \frac{1}{2} (1 - a^{**}) \right] (\langle x^{2} \rangle_{w=0} - \langle x^{2} \rangle_{w}). \tag{2.29}$$

Since the term  $\langle x^2 \rangle_{w=0} - \langle x^2 \rangle_w$  is always positive, we see that when  $\frac{z_c}{z} > \frac{1}{2}(1 - a^{**})$ ,  $\mathcal{E}_{w=0} > \mathcal{E}_w$  i.e. a perfect interface has higher energy than the disordered interface. Therefore, in this case, interface mixing is preferred due to the reduction in the strain energy. For a triangular lattice,  $a^{**} = 0.392$ , z = 6, and  $z_c = 2$ . Therefore the IFD will reduce the strain energy of this system. For the FCC lattice,  $a^{**} = 0.24$  and z = 12. In this case if the growth direction is (100) then  $z_c = 4$  and a disordered

interface increases the strain energy thereby forming a clean interface. However, if the sample is grown along (111) direction, then  $z_c = 6$  and in this case interface mixing will be preferred. This can be understood easily because  $z_c$  measures the number of bonds in the coherency plane. The larger value of  $z_c$  results in more strain energy because more bonds are constrained to make CSLs.

Before we close this section, let us discuss the result for the strain energy when  $\Delta \neq 0$ . For the sake of simplicity, we have again considered interfacial mixing of the two adjacent layers 5 and 6 only, the same situation for which numerical simulations were done. Total strain energy is

$$E_{tot} = \mathcal{E} + \mathcal{E}_{\Delta},\tag{2.30}$$

where  $\mathcal{E}_{\Delta}$  is the additional term contributing to the strain energy due to nonzero  $\Delta$  which is as follows.

$$\mathcal{E}_{\Delta} = \frac{K}{2} x_{5} (1 - x_{5}) \Delta^{2} \left[ 3 - 6x_{5} + 2x_{5}^{2} - \frac{8x_{5} (1 - x_{5})}{l + m} \right]$$

$$- 2(1 - x_{5}) (x_{5} a_{\delta \delta}^{*} + (2 - x_{5}) a_{\nu \nu}^{*}) - 2(1 - 2x_{5}) ((1 - 2x_{5}) b_{\delta \delta}^{*} + 2b_{\nu \nu}^{*})$$

$$- 4x_{5} (1 - 2x_{5}) (b_{\delta \nu}^{*} + b_{\delta \eta}^{*}) - 4x_{5}^{2} b_{\nu \eta}^{*} \right], \qquad (2.31)$$

where the parameters  $a_{\delta\delta}^*$ ,  $a_{\nu\nu}^*$ ,  $b_{\delta\delta}^*$  etc. are defined in the Appendix A. Figure 2.7 shows the dramatic difference in the  $x_5$  dependence of the strain energy for various values of  $\Delta$  for the triangular net. For  $\Delta=0$ , the strain energy vs. concentration of the interface layer shows a minimum at  $x_5=0.5$  (the bottom curve), consistent with our prediction. However, as we increase  $\Delta$ , IFD is suppressed.

#### 2.4 Summary and Conclusion

We have investigated the effects of interfacial disorder on the structure of coherent multilayers of two types of atoms. A simple central-force model has been set up for

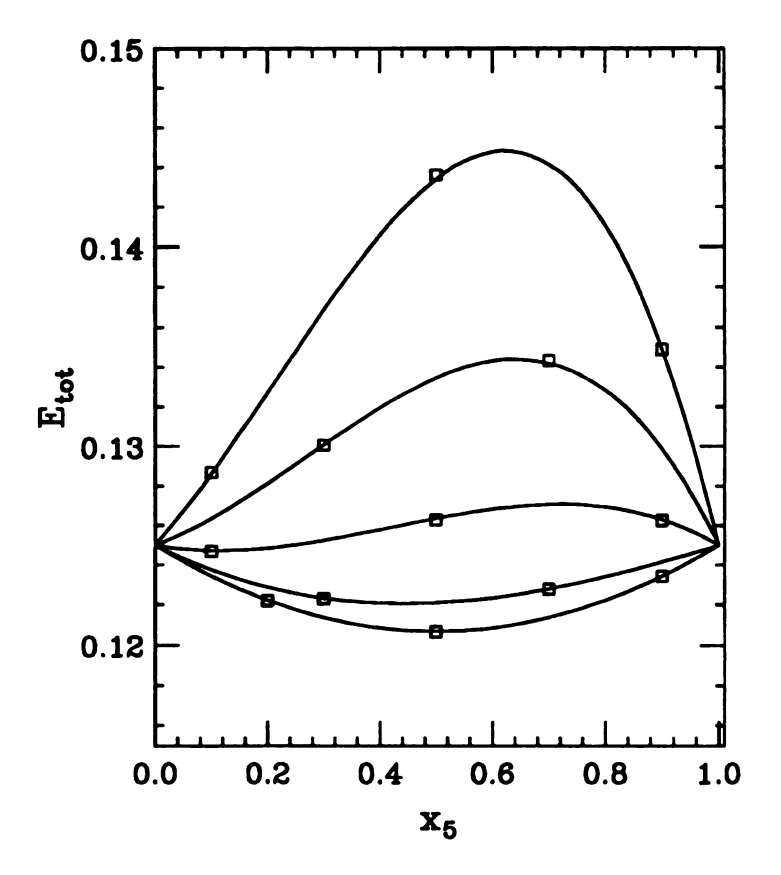


Figure 2.7: The strain energy vs. concentration of the interface layer 5 for the CSL. The system for the  $\Delta=0$  (bottom curve) shows the minimum strain energy at  $x_5=0.5$  which indicates that interface mixing is preferred. Here,  $\Delta=0$  means that  $L_{AA}^0=1$ ,  $L_{BB}^0=1.04$ , and  $L_{AB}=1.02$ . The other curves are obtained by gradually changing  $L_{AB}^0$  with  $L_{AB}^0=1.015$ , 1.01, 1.005, and 1, the top curve corresponding to  $L_{AB}^0=1.015$ .

this purpose. To preserve the coherent structure, the size of the system parallel to the layer is fixed. The problem of disordered interfaces can be solved exactly in the harmonic limit and when the spring constants between AA, BB, and AB atoms are the same. We find that the average interlayer spacings, the strain energy and average bond lengths depend on a single topological parameter  $a^{**}$  when  $\Delta=0$ . Layer spacings change in the presence of interfacial disorder and can in principle be measured by X-ray experiments. Individual bond lengths have been calculated and can be obtained from EXAFS and nuclear quadrupole resonance experiments which are in practice difficult because of the small signals from the interface regions [17]. We also find that the strain energy can determine the degree of interfacial mixing when  $L_{AA}^0$ ,  $L_{BB}^0$ , and  $L_{AB}^0$  are given although other sources such as charge transfer energy may be relevant in some situations.

### **Bibliography**

- [1] L. Esaki and R. Tsu, IBM J. Res. Develop. 14, 61 (1970).
- [2] D.B. McWhan, Synthetic Modulated Structures, Ed. by Leroy L. Chang and B.C. Giessen, Academic Press, New York (1985), p43.
- [3] An example of a strained layer superlattice in InGaAs/InP system has been discussed by J.M. Vanberg, D. Gershoni, R.A. Hamm, M.B. Parrish and H. Temkin, J. Appl. Phys. 66, 4035 (1989).
- [4] D.E. Jesson, S.J. Pennycook, and J. M. Baribeau, Phys. Rev. Lett. 66, 750 (1991).
- [5] D.M. Hwang, S.A. Schwarz, T.S. Ravi, R. Bhat, and C.Y. Chen, Phys. Rev. Lett., 66, 739 (1991).
- [6] J.W. Matthews and A.E. Blakeslee, J. Cryst. Growth 27, 118 (1974); ibid 29, 273 (1975).
- [7] A. Bourret, P. Fuoss, G. Feuillet, and S. Tatarenko, Phys. Rev. Lett., 70, 311 (1993).
- [8] S.J. Pennycook and D.E. Jesson, Phys. Rev. Lett. 64, 938 (1990).
- [9] W.P. Pratt, Jr., S.-F. Lee, J.M. Slaughter, R. Loloee, P.A. Schroder, and J. Bass, Phys. Rev. Lett. 66, 3060 (1991).

- [10] Horacio E. Camblong and Peter M. Levy, Phys. Rev. Lett. 69 2835 (1992).
- [11] Hyangsuk Seong, S.D. Mahanti, and M.F. Thorpe, Bull. Am. Phys. Soc. 36, 991 (1991); preprint.
- [12] M.F. Thorpe and E.J. Garboczi, Phys. Rev. B 42, 8805 (1990).
- [13] L. Vegard, Z. Phys. 5, 17 (1921).
- [14] Y. Cai and M.F. Thorpe, Phys. Rev. B 46, 15872 (1992).
- [15] Y. Cai and M.F. Thorpe, Phys. Rev. B 46, 15879 (1992).
- [16] Normand Mousseau and M.F. Thorpe, Phys. Rev. B 46, 15887 (1992).
- [17] Z.H. Ming, A. Krol, Y.L. Soo, Y.H. Kao, Bull. Am. Phys. Soc. 38, 84 (1993).

### Chapter 3

## Gallery Expansion of Randomly Intercalated Anharmonic Bilayers

#### 3.1 Introduction

All crystalline solid solutions show a composition dependence of the lattice constant which increases with the concentration of the large component (x) [1]. The well-known Vegard's law [2], where the average volume depends linearly on x, is obeyed a large class of semiconducting and insulating alloys of the type of  $A_{1-x}B_xC$  [3]. However, it is not obeyed by metallic alloys and ternary intercalation systems. These systems exhibit rather complex nonlinear behaviors which depend on the competition between local and global energies associated with the formation of a solid solution. An important class of such solid solutions with which we are concerned in this thesis are ternary intercalated layered systems,  $A_{1-x}B_xL$  with  $0 \le x \le 1$ , where A (small) and B (large) are two different intercalants and L represents the host layer. The major expansion of these materials occurs along the direction normal to the layers, which is commonly denoted as the c-axis[4]-[9].

Several theoretical models [5],[10]-[15] have been proposed to understand the nonlinear x-dependence of the c-axis expansion and the condition under which Ve-

gard's law can be seen. In one limiting version of these models which has been referred to as the "rigid-layer model" [5, 10], the host layers are assumed to be flat, i.e., completely rigid against transverse distortions. In this limit, the nonlinearity of the c-axis expansion arises from the finite but different compressibilities of the two intercalants i.e. different strengths of the harmonic interaction between the intercalants and the host. In another limiting version [10]-[13], so called "layer rigidity model", the finite transverse layer rigidity of the host layers has been taken into account but the intercalants have been treated to be completely incompressible (hard spheres of different diameters) and any finite concentration of large spheres opens up the gallery to its maximum value. In this model, the nonlinear x-dependence arises from the transverse rigidity of the host layers. To circumvent these two extreme assumptions, namely infinite layer rigidity and completely incompressible intercalants, a simple harmonic spring model [14, 15] has been introduced. In this model, the host-intercalant interaction is represented by two harmonic springs of equilibrium lengths  $h_A^0$  and  $h_B^0$  with spring constants  $K_A$  and  $K_B$ , respectively and the host layer rigidity is characterized by a spring constant  $K_T$ . This model has been investigated thoroughly both for bilayers [14] and for multilayers with and without correlation between the occupation of the intercalants [15]. However, this harmonic model, although quite general in many respects, does not address the role of anharmonic interaction in the gallery expansion problem. In some cases, it does not give a proper account of experimental data near x = 1 [11] and the discrepancy becomes large for rigid layers and nearly incompressible intercalants.

On physical grounds one can expect the anharmonicity in host-intercalant interaction to be important when the layers possess finite rigidity against transverse distortion. In Figure 3.1, we show a small intercalant surrounded by large intercalants. If the host layer is completely floppy then one essentially samples the harmonic region of the host-intercalant interaction potentials both for the small and large intercalants. On the other hand, if the host layer is rigid, although the interaction between the host layer and the large intercalants can be treated in harmonic approximation, one samples the anharmonic region of the potential between the small intercalant and the host layer. Harmonic approximation is not appropriate to model this latter interaction.

In addition to the atomic potential models described above, a discrete host layer distortion model with hard sphere intercalants has been proposed [10] and solved exactly [12], and its results have been applied to fit the experimental data [11, 13]. In this model referred to as "Catchment Area model" (CAM), the average normalized interlayer spacing is given by  $\langle d \rangle = 1 - (1-x)^p$ , where x is the concentration of the large intercalant and p is a measure of the healing length. In other words, p is a measure of the size of the catchment area i.e. the region over which a large intercalant B with size  $h_B^0$  opens up the gallery spacing in its neighborhood to  $h_B^0$ . Also, in this model, it is assumed that if another large intercalant is present within this "healing length", then the gallery spacing at this site does not increase any further and remains at  $h_B^0$ . The form of  $\langle d \rangle$  obtained with CAM describes the gallery expansion of layered solids such as  $Li_xV_{1-x}C_6$  (V is a vacancy) and  $Cs_xRb_{1-x}Vm$  (Vm is a vermiculite) [13] very well. From the fit to the experimental data, one finds that the host layer rigidity parameter (p) increases from graphite to vermiculite and is consistent with the increased transverse rigidity of the host layers.

The CAM as described above represents an extremely anharmonic system, as regards both the host-intercalant interaction and the host layer distortion are concerned. Unfortunately, in this model anharmonicity cannot be controlled. It is

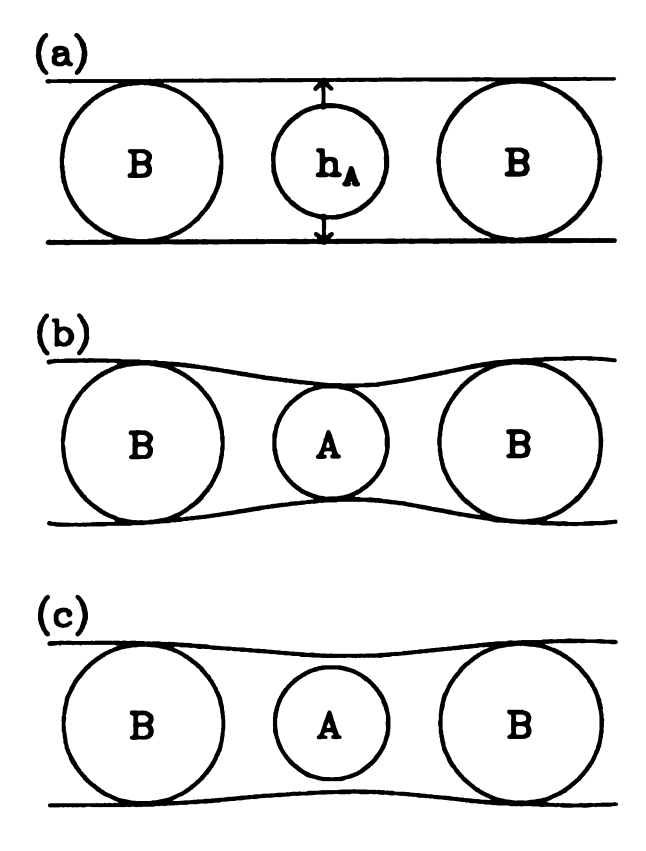


Figure 3.1: An example of a 1-dimensional bilayer model in which a small intercalant is surrounded by large intercalants. The solid lines represent the host layers and the circles depict the intercalants. The diameter of the circle A(B) is  $h_A^0(h_B^0)$  which is the natural length of atom A(B). (a) The host layer is perfectly rigid; therefore, equilibrium length of A atom,  $h_A$ , is  $h_B^0$ , thus sampling the anharmonic region of the potential between the small intercalant and the host layers. (b) The host layer is perfectly floppy; therefore,  $h_A$  is  $h_A^0$  which is its natural length. (c) The host layer has a finite rigidity; therefore,  $h_A^0 < h_A^0 < h_B^0$ .

therefore important to study a physical model where one can control the degree of anharmonicity and see how it affects the average gallery spacing and the local gallery distortion.

In this chapter, we introduce an anharmonic potential model and study this using both numerical simulations and analytic techniques. For simplicity, we use a bilayer model, in which we only consider a single gallery between two host layers where the intercalants go. Also, we include anharmonicity only in the potential energy between the host layer and the intercalants, while using the usual harmonic approximation for the host layer deformation energy. Preliminary results of this model have been reported in Ref.[16]. Taking account of anharmonicity effects in the host layer distortion energy is extremely difficult and will be the subject of future research.

The arrangement of this chapter is as follows. In Sec. 3.2, different anharmonic potentials between the host layer and the intercalants are introduced and the results of a few limiting cases (perfectly floppy and perfectly rigid layer) are discussed. In Sec. 3.3, the single impurity problem is studied analytically to understand the behavior of the system near x = 1. An effective medium theory is developed in Sec. 3.4 and its results compared with numerical simulations in Sec. 3.5. In Sec. 3.6, we compare the results of the numerical simulations of Lennard-Jones potential with that of the CAM discussed earlier. Finally, in Sec. 3.7, we give a brief summary of our major findings.

#### 3.2 The Model and Limiting Cases

Consider a ternary layered system  $A_{1-x}B_xL$  consisting of a single gallery with intercalants randomly occupying a set of lattice sites between two host layers. A (small) and B (large) are two different types of intercalants and L is the host layer such as graphite, dichalcogenide, or vermiculite. For a fixed intercalant distribution, there are two major contributions to the total deformation energy of the system; one is the interaction between the host and the intercalants and the other between the host atoms themselves,

$$E = E_{HI} + \frac{1}{2} \sum_{n} K_T (h_n - h_{n+1})^2.$$
 (3.1)

In Eq. (3.1),  $E_{HI}$  is the interaction energy between the host and the intercalants,  $K_T$  represents the transverse rigidity of the layers, and  $h_n$  is the local gallery height (the distance between two adjacent host layers) at the n-th site. In the harmonic approximation,  $E_{HI}$  is replaced by harmonic potentials [14], i.e.,

$$E_{HI} = \frac{1}{2} \sum_{n} K_n (h_n - h_n^0)^2, \tag{3.2}$$

where  $K_n$  and  $h_n^0$  are the spring constant and the equilibrium height of the intercalant at the site n, respectively.

A simple and yet realistic way to extend the model to physical systems is to consider a Lennard-Jones (LJ) potential to represent the interaction between the host and the intercalants. For charged intercalants, as in ternary complex layered oxides, the interaction between the host and the intercalant is long ranged. But for short wavelength "local" deformations, this long range interaction may not be very important. In graphite intercalation compounds, the long range interaction is usually screened and a short range model is adequate. In the LJ potential model,

$$E_{HI} = E_{LJ} = \sum_{n} 4\epsilon_n \left\{ \left( \frac{\sigma_n}{h_n} \right)^{12} - \left( \frac{\sigma_n}{h_n} \right)^{6} \right\}, \tag{3.3}$$

where the parameters  $\epsilon_n$  and  $\sigma_n$  can be obtained, for example, from the gas-phase data [17, 18]. To see the strength of the anharmonic effect in the LJ model, one

can make use of Taylor series expansion of the LJ potential about the minimum  $(h_n^0 = \sqrt[6]{2}\sigma_n)$ , namely,

$$E_{LJ} = \sum_{n} \left[ E_{n0} + \frac{1}{2!} K_n (h_n - h_n^0)^2 - \frac{1}{3!} \gamma_n (h_n - h_n^0)^3 + \cdots \right], \tag{3.4}$$

where

$$K_n = \frac{\partial^2 E_{LJ}}{\partial h_n^2} = \frac{72\epsilon_n}{\sqrt[4]{2}\sigma_n^2},\tag{3.5}$$

and

$$\gamma_n = -\frac{\partial^3 E_{LJ}}{\partial h_n^3} = 1512 \frac{\epsilon_n}{\sqrt{2}\sigma_n^3}.$$
 (3.6)

The second term on the right hand side of Eq. (3.4) corresponds to a harmonic potential and the subsequent terms to the anharmonic contributions. In the LJ potential, the strength of the first anharmonic term relative to the harmonic term  $\gamma_n/K_n$  is fixed for a given value of  $\sigma_n$ . Therefore, to isolate the effect of anharmonicity, we introduce a slightly modified model in which one can vary the strength of the anharmonic term independently, namely,

$$E_C \equiv \frac{1}{2!} \sum_n K_n (h_n - h_n^0)^2 - \frac{1}{3!} \sum_n \gamma_n (h_n - h_n^0)^3, \tag{3.7}$$

where  $K_n(>0)$  and  $\gamma_n(>0)$  serve as control parameters. In this model one can easily study how the physical properties of the system evolve from the harmonic interaction limit. This cubic potential model is simpler than LJ potential for analytic calculations, hence we will concentrate on this model for analytic calculations.

In connection with the transverse rigidity of the host layer, one can think of two limiting cases,  $K_T \to 0$  and  $K_T \to \infty$ . If the layers are completely floppy towards transverse distortions  $(K_T = 0)$ , then obviously all  $h_n$ 's have their equilibrium lengths. Therefore the average gallery height  $\langle h \rangle$ , defined by

$$\langle h \rangle \equiv \frac{1}{N} \sum_{n} h_{n}, \tag{3.8}$$

obeys Vegard's law (i.e.  $\langle h \rangle = (1-x)h_A^0 + xh_B^0$ ) for both Eqs. (3.4) and (3.7). If on the other hand, the layers are infinitely rigid  $(K_T \to \infty)$ , then the energy E in Eq. (3.1) is minimized by having all  $h_n$ 's equal. Then the average height has the value

$$\langle h \rangle_{LJ} = \left( \frac{(1-x)K_A h_A^{0^{14}} + xK_B h_B^{0^{14}}}{(1-x)K_A h_A^{0^{8}} + xK_B h_B^{0^{8}}} \right)^{\frac{1}{6}}$$
(3.9)

for the LJ potential, and

$$\langle h \rangle_C = \frac{(1-x)(K_A + \gamma_A h_A^0) + x(K_B + \gamma_B h_B^0)}{(1-x)\gamma_A + x\gamma_B}$$

$$-\frac{\sqrt{\left\{(1-x)K_A+xK_B+x\gamma_B\Delta h\right\}^2-\left\{(1-x)\gamma_A+x\gamma_B\right\}\Delta hx(2K_B+\gamma_B\Delta h)}}{(1-x)\gamma_A+x\gamma_B},$$

(3.10)

for the cubic potential and  $\Delta h = h_B^0 - h_A^0$ . In the harmonic limit  $(\gamma_A = \gamma_B = 0)$ , Eq. (3.10) recovers the results of Dahn *et al.* [5] which is

$$\langle h \rangle_C = \frac{(1-x)K_A h_A^0 + xK_B h_B^0}{(1-x)K_A + xK_B},\tag{3.11}$$

and obeys Vegard's law when  $K_A = K_B$ .

We have performed a series of numerical simulations for both the LJ and the cubic potential models. Typical behavior for the x-dependence of the normalized spacing  $\langle d \rangle$  is shown in Figure 3.2, where the simulation results for  $K_A = K_B$  are compared with Vegard's law. When  $K_A = K_B$ , the harmonic potential system shows Vegard's law regardless of the value of  $K_T$  [14]. However, even if  $K_A = K_B$ ,

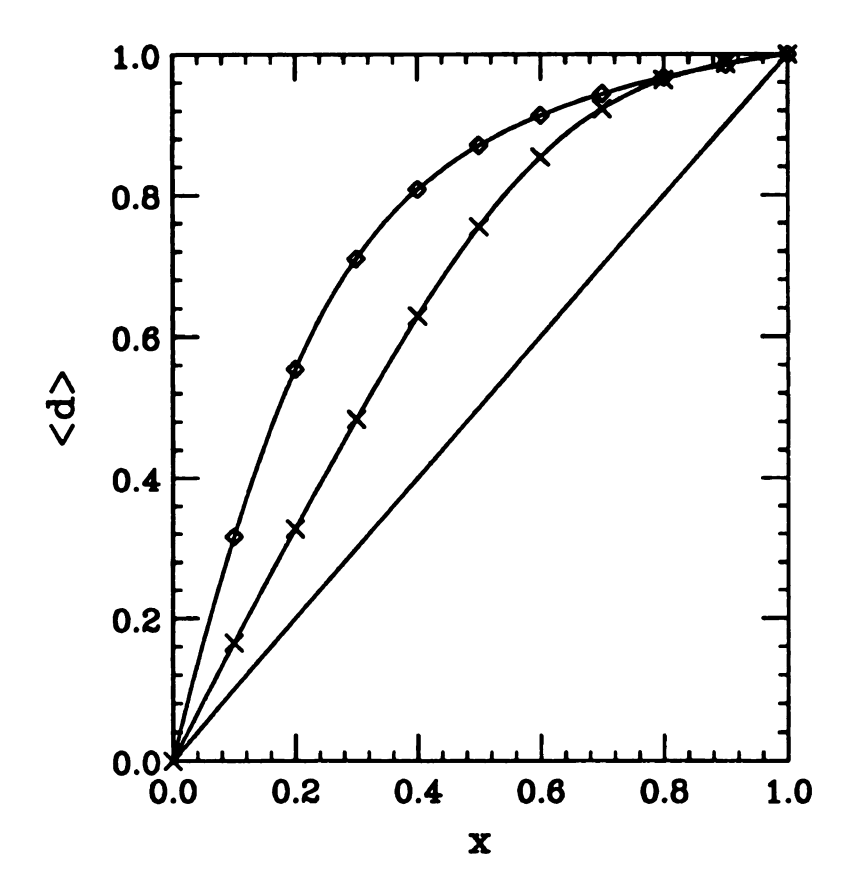


Figure 3.2: The deviation from the Vegard's law for the anharmonic potentials:  $K_A/K_B = 1, K_T/K_B = 10. \diamond$ : LJ potential,  $\times$ : cubic potential with  $\gamma_n$  given by Eq. (3.5), -: Vegard's law. The solid lines on symbols are guide for eyes.

or equivalently  $\epsilon_A/\sigma_A^2 = \epsilon_B/\sigma_B^2$ ,  $\langle h \rangle_{LJ}$  and  $\langle h \rangle_C$  do not obey Vegard's law but show a nonlinear x dependence due to the effect of anharmonicity.

The upward shift of the curves from the linear x-dependence in Figure 3.2 can be explained from the shape of the potentials used. For positive  $\gamma_n$ 's both forms of the anharmonic potentials cost more (less) energy under compression (expansion) than the harmonic potentials. Therefore, when one minimizes the total deformation energy, the small atoms with the anharmonic potentials adjacent to big atoms tend to stretch longer than those with the harmonic ones, while the big atoms tend to compress less. This is manifested in the larger average gallery expansion for the anharmonic potentials than that for the harmonic ones as seen in Figure 3.2. If one had used negative  $\gamma_n$ 's, one would have seen downward shift (sublinear x-dependence) of the curves from Vegard's law behavior.

# 3.3 Single Impurity with Anharmonic Cubic Potential

To understand the upward shift (or what is referred to as overhang) of the gallery height quantitatively near x = 1, let us consider a single small atom A in a chain of N lattice sites with all other sites occupied by B atoms. For simplicity, we will use a harmonic potential for the B atoms and a cubic anharmonic potential for the A atom. Harmonic approximation for the B atoms has been found to be adequate from numerical simulations. The anharmonicity of B atoms hardly affects the average gallery expansion because large atoms are always compressed in bilayer systems. Suppose that a single A atom is at the origin, then the deformation energy of the chain is given by

$$E_S = \frac{1}{2} \sum_{n} K_n (h_n - h_n^0)^2 - \frac{1}{3!} \sum_{n} \gamma_n (h_n - h_n^0)^3 + \frac{1}{2} \sum_{n} K_T (h_n - h_{n+1})^2, \tag{3.12}$$

where

$$K_n = K_B(1 - \delta_{n0}) + K_A\delta_{n0} = K_B - \Delta K\delta_{n0},$$

$$h_n^0 = h_B^0(1 - \delta_{n0}) + h_A^0\delta_{n0} = h_B^0 - \Delta h\delta_{n0},$$

and

$$\gamma_n = \gamma \delta_{n0}$$
.

Here, we have used  $\Delta K \equiv K_B - K_A$  and  $\Delta h \equiv h_B^0 - h_A^0$ . Minimizing this energy with respect to  $h_n$ , we get

$$K_n(h_n - h_n^0) - \frac{1}{2}\gamma_n(h_n - h_n^0)^2 + K_T(2h_n - h_{n+1} - h_{n-1}) = 0.$$
 (3.13)

Next, taking the Fourier transform of  $h_n$  i.e.  $h_n = \sum_q h(q)e^{iqn}$  and using periodic boundary condition  $(h_{N+n} = h_n)$ , we obtain

$$(K_B + 2K_T(1-\cos p))h(p) - \frac{\Delta K}{N} \sum_{q} h(p-q) + \frac{1}{N}(K_B \Delta h + h_A^0 \Delta K)$$

$$-\frac{\gamma}{N} \left[ \frac{h_A^{0^2}}{2} - h_B^0 \sum_{q} h(p-q) + \frac{\Delta h}{N} \sum_{q} \sum_{q'} h(p-q-q') + \frac{1}{2} \sum_{q} \sum_{q'} h(q') h(p-q-q') \right]$$

$$=K_B h_B^0 \delta_{p,0}. \tag{3.14}$$

The quantity of physical interest,  $\langle h \rangle$ , which is equal to h(0) can be obtained from the solution of Eq. (3.14). Assuming that  $\sum_{q} h(p-q) = \sum_{q} h(q)$  and changing the

notation 1/N to 1-x, we have the final result for the average gallery height,

$$\langle h \rangle = h(0) = h_B^0 - \Delta h \frac{1-x}{W} + \frac{1-x}{\gamma W} \left[ \frac{K_B}{W} - \Delta K - \sqrt{\left\{ \frac{K_B}{W} - \Delta K \right\}^2 - 2K_B \gamma \Delta h (\frac{1}{W} - 1) \right]}.$$

$$(3.15)$$

In the above equation, W is the Watson integral [14] given by

$$W = \frac{1}{N} \sum_{p} \frac{K_B}{K_B + 2K_T (1 - \cos p)}$$
 (3.16)

and is inversely proportional to the transverse layer rigidity  $K_T$ . The results of Eq. (3.15) for different  $K_T$  are compared with the results of numerical simulations in Figure 3.3 and fit very well with the slopes of the average gallery spacings obtained numerically.

When  $\gamma = 0$ , the third term in Eq.(3.15) vanishes and the average gallery height reduces to the correct harmonic limit of Ref. [14]. In addition, for  $\gamma > 0$ , the anharmonic contribution to  $\langle h \rangle$  is always positive because  $0 \le W \le 1$ . This positive deviation results in a larger gallery expansion than the harmonic case caused by the cubic anharmonic potential. Further, the more rigid the layer is, the larger this deviation is.

### 3.4 Effective Medium Theory (EMT)

To understand the gallery expansion of  $A_{1-x}B_xL$  for arbitrary values of x, we use an effective medium theory (EMT) for the bilayer model with many defects. In this section, the cubic potential is used for both A and B intercalants. To develop an EMT for this anharmonic system, we follow the general ideas discussed in a series of papers [14, 15, 19] developed for the harmonic potential model.

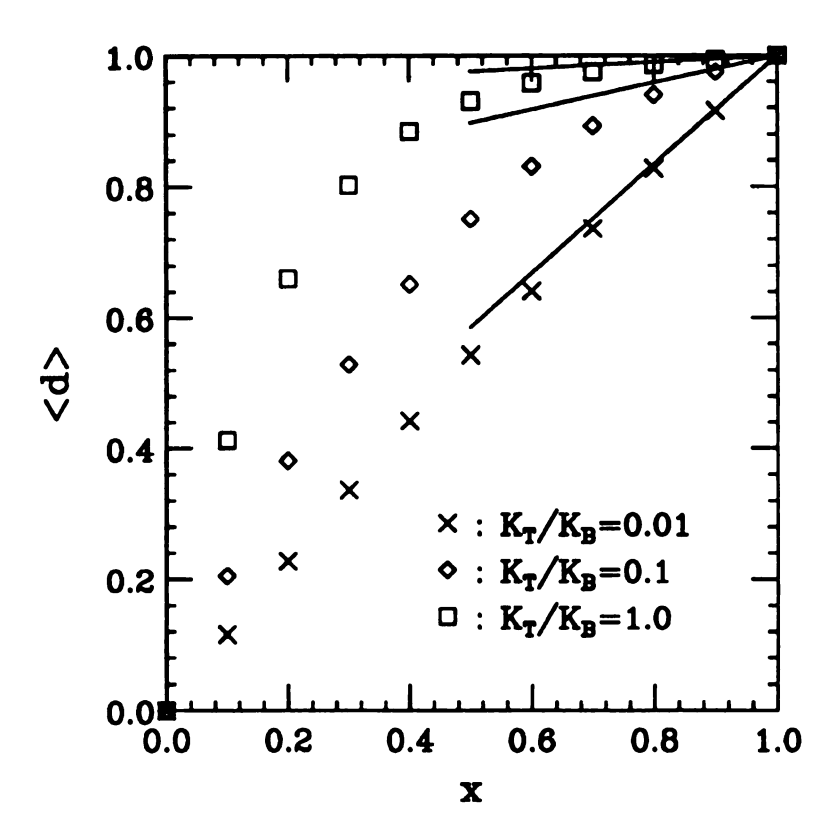


Figure 3.3: Comparison of the numerical simulations (symbols) with the single impurity results. Solid lines are single impurity results which give us the slopes of the average gallery spacings near x = 1. We have used three different values of  $K_T/K_B$  as shown in the figure with other parameters fixed;  $\gamma_A/K_A = \gamma_B/K_B = 2.0$  and  $K_A/K_B = 0.1$ .

In the EMT for harmonic systems, an effective medium is constructed with uniform springs of force constant K and equilibrium length  $h_e$  for each intercalant and  $K_T$  for the host layers. To study the local distortions caused by an external force F, the total system is represented by one spring with an effective force constant  $K_e$  and an effective equilibrium length  $h_e$ . The effective force constant  $K_e$  can be easily shown to be given by

$$K_e = \frac{K}{W},\tag{3.17}$$

where the Watson integral W given in Eq. (3.16) contains the combined effects of all the springs in the system.

To study the effect of randomly intercalated atoms, the theory proceeds by replacing one of the effective medium springs, K, by a spring for either A or B impurity. This system can be visualized as two springs in parallel, one with spring constant  $K_e - K$  and the other with either  $K_A$  or  $K_B$ . The local height and the energy of either A or B intercalant are obtained by minimizing the energy for each configuration. With these local heights and the corresponding local distortion energies, the total energy is expressed as a sum of the energies of A and B impurities with probabilities 1 - x and x, respectively. This total energy is now a function of two unknown parameters,  $h_e$  and K. Finally, the problem is solved by imposing two conditions; one is the self-consistent equation for the displacement under the external force F to obtain  $K_e$ , hence K. The other is the minimization of the total energy to get  $h_e$ .

For the anharmonic system, we similarly consider an effective medium composed of uniform anharmonic springs characterized by K and  $\gamma$  with natural lengths  $h_e$  for the host-intercalant interaction and harmonic springs characterized by  $K_T$  for the

host layers. To obtain the effective spring parameters  $K_e$  and  $\gamma_e$ , we consider the system in the presence of a local external force F. If the external force is applied to a single site at the origin, the energy can be written as

$$E = \frac{1}{2} \sum_{n} K(h_{n} - h_{e})^{2} - \frac{1}{3!} \sum_{n} \gamma(h_{n} - h_{e})^{3} + \frac{1}{2} \sum_{n} K_{T}(h_{n} - h_{n+1})^{2} - F(h_{0} - h_{e}).$$
(3.18)

Minimizing this energy with respect to  $h_n$  and performing the Fourier transform on  $\Delta_n \ (\equiv h_n - h_e)$ , we get

$$\Delta(p) = \frac{F}{\Phi(p)} + \frac{\gamma}{2} \sum_{q} \frac{\Delta(q)\Delta(p-q)}{\Phi(p)},\tag{3.19}$$

where

$$\Phi(p) \equiv K + 2K_T(1 - \cos p). \tag{3.20}$$

The local displacement at the origin  $\Delta_0$  can be written as

$$\Delta_0 = \sum_{p} \Delta(p) \tag{3.21}$$

$$= \sum_{p} \frac{F}{\Phi(p)} + \frac{\gamma}{2} \sum_{p} \sum_{q} \Delta(q) \Delta(p-q) / \Phi(p)$$
 (3.22)

$$= \sum_{p} \frac{F}{\Phi(p)} + \frac{\gamma}{2} \frac{1}{K'} \sum_{p} \sum_{q} \Delta(q) \Delta(p-q)$$
 (3.23)

$$= \frac{FW(K)}{K} + \frac{\gamma}{2} \frac{1}{K'} \Delta_0^2. \tag{3.24}$$

1/K' is a quantity related to  $1/\Phi(p)$  and  $\Delta(p)$  through the equation

$$1/K' = \frac{\sum_{p} \sum_{q} \Delta(q) \Delta(p-q) / \Phi(p)}{\sum_{p} \sum_{q} \Delta(q) \Delta(p-q)}.$$
(3.25)

Different approximation to obtain 1/K' will be discussed later. Eq. (3.24) can now be solved to give the equilibrium length at the origin under the external force F, i.e.,

$$h_0 = h_e + \Delta_0 = h_e + \frac{K' - \sqrt{K'^2 - 2\gamma W F K' / K}}{\gamma}.$$
 (3.26)

Now the same system can also be described by a single anharmonic spring characterized by  $K_e$ ,  $\gamma_e$ , and an effective length  $h_e$  under the same external force F. Then the energy is given by

$$E_{eff} = \frac{1}{2!} K_e (h - h_e)^2 - \frac{1}{3!} \gamma_e (h - h_e)^3 - F(h - h_e). \tag{3.27}$$

Minimizing this energy gives the equilibrium length,  $h_s$ , of the effective single spring in the presence of F,

$$h_s = h_e + \frac{K_e - \sqrt{K_e^2 - 2\gamma_e F}}{\gamma_e}.$$
(3.28)

The parameters for the single effective spring can now be found by equating  $h_0$  of Eq. (3.26) with  $h_s$  of Eq. (3.28) and expanding the resulting equation in terms of an arbitrary force F. This leads to

$$K_e = \frac{K}{W} \tag{3.29}$$

and

$$\gamma_e = \frac{\gamma K}{W K'}.\tag{3.30}$$

Like the EMT for harmonic springs, we now replace one of the uniform springs with K and  $\gamma$  by either A or B spring. Then the system can be represented by two

anharmonic springs in parallel; one with  $K'_e = K_e - K$  and  $\gamma'_e = \gamma_e - \gamma$  formed by removing the spring K and  $\gamma$  and the other with  $K_{\alpha}$  and  $\gamma_{\alpha}$  where  $\alpha$  can be either A or B with probability 1-x and x, respectively. The total energy (per site)  $\mathcal{E}_{\alpha}$  for either of these two types of springs in the presence of F is given by

$$\mathcal{E}_{\alpha} = \frac{K'_{e}}{2!} (h - h_{e})^{2} - \frac{\gamma'_{e}}{3!} (h - h_{e})^{3} - F(h - h_{e}) + \frac{K_{\alpha}}{2!} (h - h_{\alpha}^{0})^{2} - \frac{\gamma_{\alpha}}{3!} (h - h_{\alpha}^{0})^{3}.$$
(3.31)

This energy is minimized with respect to h and gives the local height  $\langle h_{\alpha} \rangle$ ;

$$\langle h_{\alpha} \rangle = \frac{\gamma_e' h_e + \gamma_{\alpha} h_{\alpha}^0 + K_e' + K_{\alpha}}{\gamma_e' + \gamma_{\alpha}}$$

$$-\frac{\sqrt{(\gamma'_{e}h_{e} + \gamma_{\alpha}h_{\alpha}^{0} + K'_{e} + K_{\alpha})^{2} - (\gamma'_{e} + \gamma_{\alpha})(\gamma'_{e}h_{e}^{2} + \gamma_{\alpha}h_{\alpha}^{0}^{2} + 2(K'_{e}h_{e} + K_{\alpha}h_{\alpha}^{0} + F))}}{\gamma'_{e} + \gamma_{\alpha}}.$$
(3.32)

The average height  $\langle h \rangle$  is therefore

$$\langle h \rangle = (1 - x)\langle h_A \rangle + x\langle h_B \rangle. \tag{3.33}$$

Self-consistency requires that this  $\langle h \rangle$  be the same as  $h_s$  in Eq. (3.28). The expansion of the equation  $h_s = \langle h \rangle$  up to the second order in F gives three equations for K,  $\gamma$ , and  $h_e$ , namely

$$h_e = \frac{1-x}{\gamma'_e + \gamma_A} (g(A) - \sqrt{T_A}) + \frac{x}{\gamma'_e + \gamma_B} (g(B) - \sqrt{T_B})$$
(3.34)

$$\frac{1}{K_e} = \frac{1-x}{\sqrt{T_A}} + \frac{x}{\sqrt{T_B}} \tag{3.35}$$

$$\frac{\gamma_e}{K_e^3} = \frac{1-x}{\sqrt{T_A}^3} (\gamma_e' + \gamma_A) + \frac{x}{\sqrt{T_B}^3} (\gamma_e' + \gamma_B)$$
 (3.36)

where

$$g(A) = \gamma'_{e}h_{e} + \gamma_{A}h_{A}^{0} + K'_{e} + K_{A}$$

$$f(A) = \gamma'_{e}h_{e}^{2} + \gamma_{A}h_{A}^{0^{2}} + 2K'_{e}h_{e} + 2K_{A}h_{A}^{0}$$

$$T_{A} = g(A)^{2} - (\gamma'_{e} + \gamma_{A})f(A)$$

and similar equations with A replaced by B.

Eqs. (3.34)-(3.36) are the EMT equations for the anharmonic model and are solved numerically in conjunction with Eqs. (3.29) and (3.30) where  $K_e$  and  $\gamma_e$  are given in terms of K and  $\gamma$ . The results will be discussed in the next section. In the Appendix B, we show how these three equations recover the earlier EMT equations obtained in the harmonic system when  $\gamma_A = \gamma_B = 0$ .

Finally we would like to discuss how one obtains 1/K' defined in Eq. (3.25). Solutions of the above three equations also depend on how we choose 1/K' which appears in the solution to the local distortion problem. As an approximation, we replace  $1/\Phi(p)$  in the second term in the right hand side of Eq. (3.22) by its average over the p-space which is W/K, because the most natural way of including the layer rigidity is to use the Watson integral. Nevertheless, one has to be cautious because this choice implies that  $\gamma_e = \gamma$  and therefore  $\gamma'_e = 0$  i.e. if we apply a force to one of the springs of the effective medium  $(K,\gamma)$ , the effect of coupling through  $K_T$  to the rest of the springs only modifies the harmonic part  $K \to K_e$  but not the anharmonic part. However, it is worth noticing that, regardless of the choice of 1/K', Eqs. (3.34)-(3.36) do recover the results for known cases i.e. for the perfectly floppy layers (Vegard's law), for the perfectly rigid layers (Eq. (3.11)) [5], and in the harmonic potential limit [14]  $(\gamma = 0)$ .

## 3.5 Numerical Simulations and Comparison with EMT

Numerical simulations have been carried out for a linear chain with N(=2000) atoms for both the LJ and the cubic potential models. Natural length of an atom A(B),  $h_A^0(h_B^0)$ , is chosen to be 3.074 (3.820). To generate a configuration of the  $A_{1-x}B_xL$  bilayer system, the linear chain is initially filled with all A atoms. Then, A atoms are randomly selected and replaced by B atoms until the total number of B atoms  $N_B = xN$ . For a given concentration x, 2000 different configurations are considered. For each configuration, the conjugate gradient method [20] is used to minimize the deformation energy given by Eq. (3.1).

Figure 3.4 gives a typical result from the simulations as x varies from 0 to 1. The symbols are simulation results and the lines are guide to the eye. We have chosen  $K_A/K_B = 0.1$ , i.e., the smaller atom is more compressible. The middle curve shows the normalized average gallery spacing of the chain  $\langle d \rangle$  which is defined by

$$\langle d \rangle = \frac{\langle h \rangle - h_A^0}{h_B^0 - h_A^0}. \tag{3.37}$$

The lower (upper) curve shows the normalized average spacing  $\langle d_A \rangle (\langle d_B \rangle)$  of the A(B) atoms.  $\langle d_A \rangle$  changes much more rapidly with x than  $\langle d_B \rangle$  because the A atoms with smaller spring constant cost less energy to compress or expand.

Figure 3.5 compares the numerical simulation results with EMT calculations for different values of the layer rigidity parameter  $K_T$ . The solid line is the usual Vegard's law given here for the sake of a reference, which is obtained when  $K_T = 0$  (perfectly floppy system). The overall agreement between the simulations and the EMT results is very good. In the region  $x \to 1$  where small intercalants can be treated as impurities, EMT results fit extremely well with the simulation results

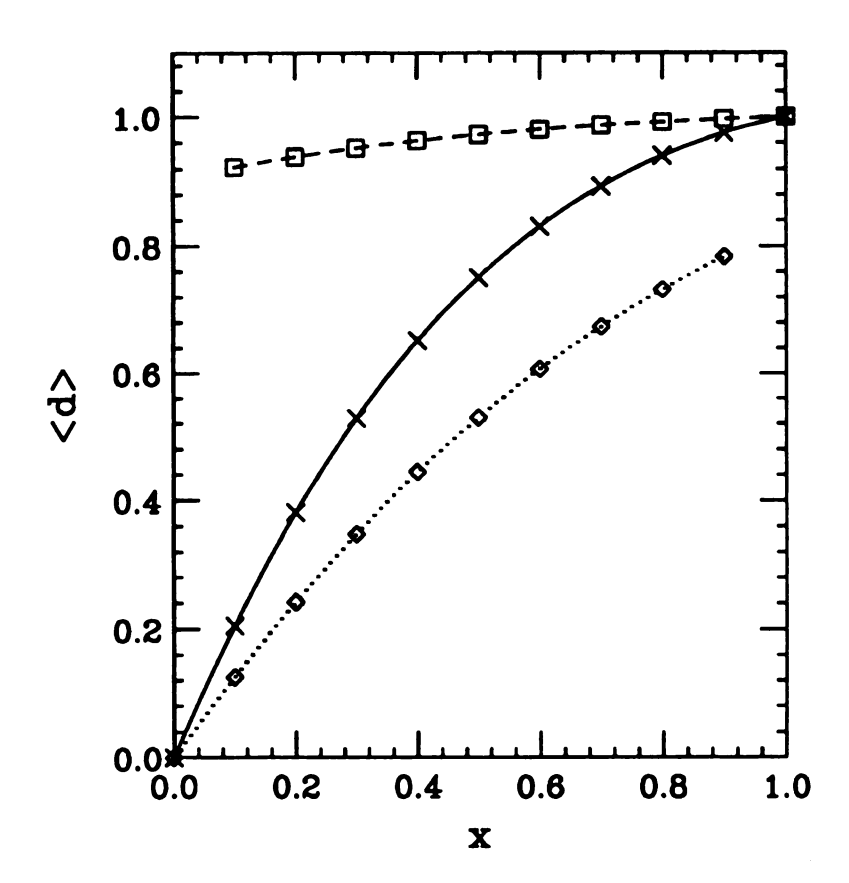


Figure 3.4: Average gallery spacing (x) of a bilayer system,  $\square$  for B-atom,  $\diamond$  for A-atom in  $K_A/K_B = K_T/K_B = 0.1$  and  $\gamma_A/K_A = \gamma_B/K_B = 2$ . The lines are guides to the eye.

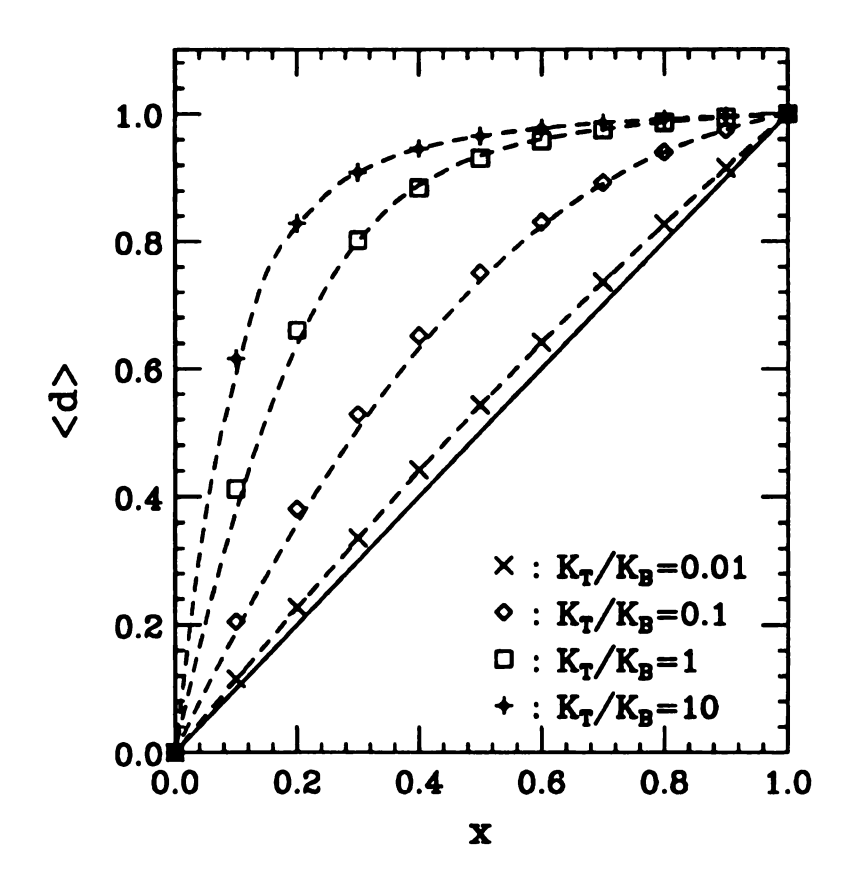


Figure 3.5: Comparison of the numerical simulations (symbols) with the EMT (dashed curves). The straight solid line represents the Vegard's law. We have used four different values of  $K_T/K_B$  as shown in the figure with other parameters fixed;  $\gamma_A/K_A = \gamma_B/K_B = 2$  and  $K_A/K_B = 0.1$ .

because (1) our choice  $(\gamma_e = \gamma)$  handles the anharmonicity of an impurity very accurately and (2) the anharmonicity of large atoms does not play any significant role in the gallery expansion as we have discussed in Sec. 3.3. In the small x limit, however, there are many small atoms whose anharmonicity plays important role in the gallery expansion. Therefore our analytic calculation shows some deviations in the small x region due to the several approximations made in obtaining the EMT results. As seen in the figure, EMT results agree very well with the simulations for small and large  $K_T$  and deviate for intermediate  $K_T$  values. Deviation between EMT and numerical simulation results as  $K_T$  is varied is understood in the following way. In Eq. (3.25), the quantity 1/K' can be thought of as the weighted average of  $1/\Phi(p)$  with the weight function  $w(p) = \sum_{p} \sum_{q} \Delta(q) \Delta(p-q)$ . We can think of limiting cases again as in Sec. 3.2. (1) perfectly floppy layers or  $K_T/K = 0$ , W(K) = 1: Since  $\Phi(p)$  is independent of p (see Eq. (3.20)), the weighted average of  $1/\Phi(p)$ , 1/K', is given by 1/K regardless of w(p);  $K_T/K_B = 0.01$  in Figure 3.5 is close to this case. (2) perfectly rigid layers or  $K_T/K \to \infty$ , W(K) = 0: Since  $\Phi(p)$  is very large (see Eq. (3.20)), the weighted average of  $1/\Phi(p)$ , 1/K', can be considered 0 which is again independent of p.  $K_T/K_B = 10$  in the figure can be in this category. Therefore, for these two limiting cases, 1/K' is treated accurately and our EMT results fit numerical simulation results very well for arbitrary values of  $K_T$ .

Figure 3.6 shows gallery expansion as anharmonic parameters are increased for a given value of  $K_T$ . All the results of EMT fit well with numerical simulation results for weak anharmonicity and the agreement is particularly good in the region of  $x \to 1$ . The EMT results, however, deviate appreciably with increasing anharmonicity because of the assumptions we have made.

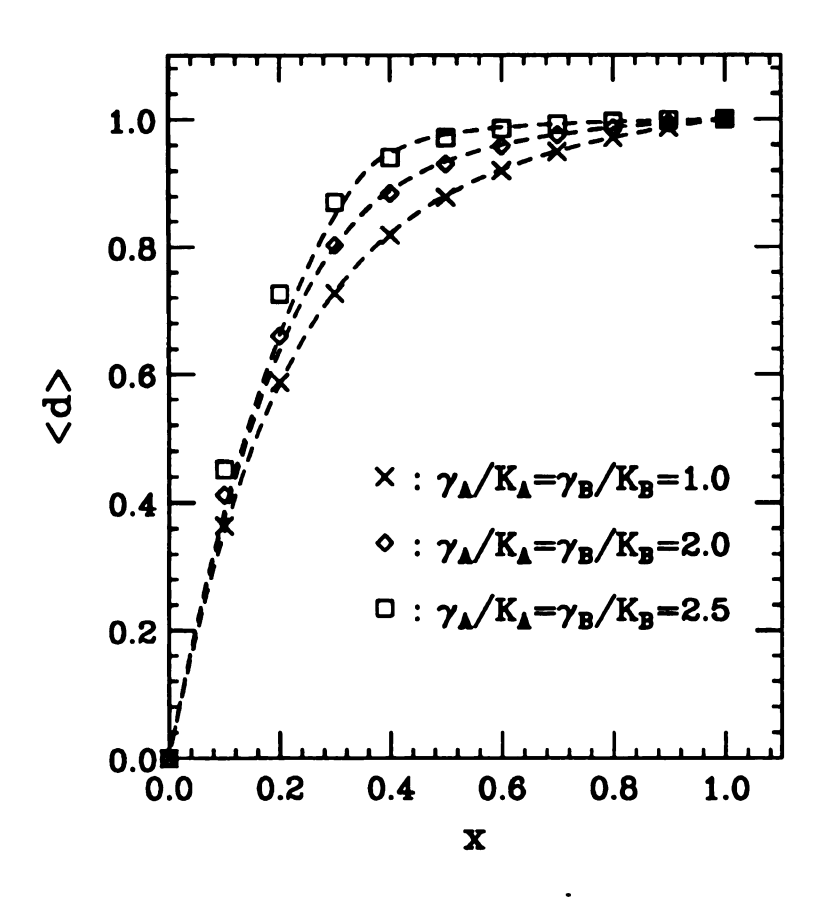


Figure 3.6: Comparison of the numerical simulations with the EMT results for different strengths of the anharmonicity. The results from the simulations are denoted by different symbols, while those from the EMT are drawn by dashed lines.  $K_A/K_B = 0.1, K_T/K_B = 1.0$ .

# 3.6 Comparison of Anharmonic Potential Model with Catchment Area Model

As we have discussed in Sec. 3.1, the normalized gallery height  $\langle d \rangle$  is given by

$$\langle d \rangle = 1 - (1 - x)^p \tag{3.38}$$

in the CAM [11, 12], which is an example of an extremely anharmonic (hard sphere) potential model. In this model, the average gallery spacing evaluated over the small intercalant sites is

$$\langle d_A \rangle = 1 - (1 - x)^{p-1}.$$
 (3.39)

This is easily obtained from the following argument: the CAM involves hard sphere atoms, therefore, the large intercalants cannot be compressed. Namely the normalized gallery spacing of the large intercalants,  $\langle d_B \rangle$ , is always 1 and there is an exact relation [12] between  $\langle d \rangle$ ,  $\langle d_A \rangle$ , and  $\langle d_B \rangle$  given by

$$\langle d \rangle = (1 - x)\langle d_A \rangle + x\langle d_B \rangle. \tag{3.40}$$

From this equation and noting that  $\langle d_B \rangle = 1$ , we immediately obtain  $\langle d_A \rangle = 1 - (1 - x)^{p-1}$ . To see how a continuous anharmonic potential describes the x-dependence of  $\langle d \rangle$  and  $\langle d_A \rangle$  as given by the CAM, we fit numerical simulation results obtained with LJ potential for these quantities to  $1 - (1 - x)^p$  and  $1 - (1 - x)^{p-1}$  (see Figure 3.7). These four figures are for different values of  $K_A/K_B$  and for a given value of the transverse layer rigidity. For a fixed layer rigidity  $K_T/K_B$ , as the ratio  $K_A/K_B$  decreases, the value of p increases and the agreement between simulations and CAM results becomes better because expansion of the small atom costs very small energy similar to the hard sphere case. Note that in the CAM it does not cost any energy

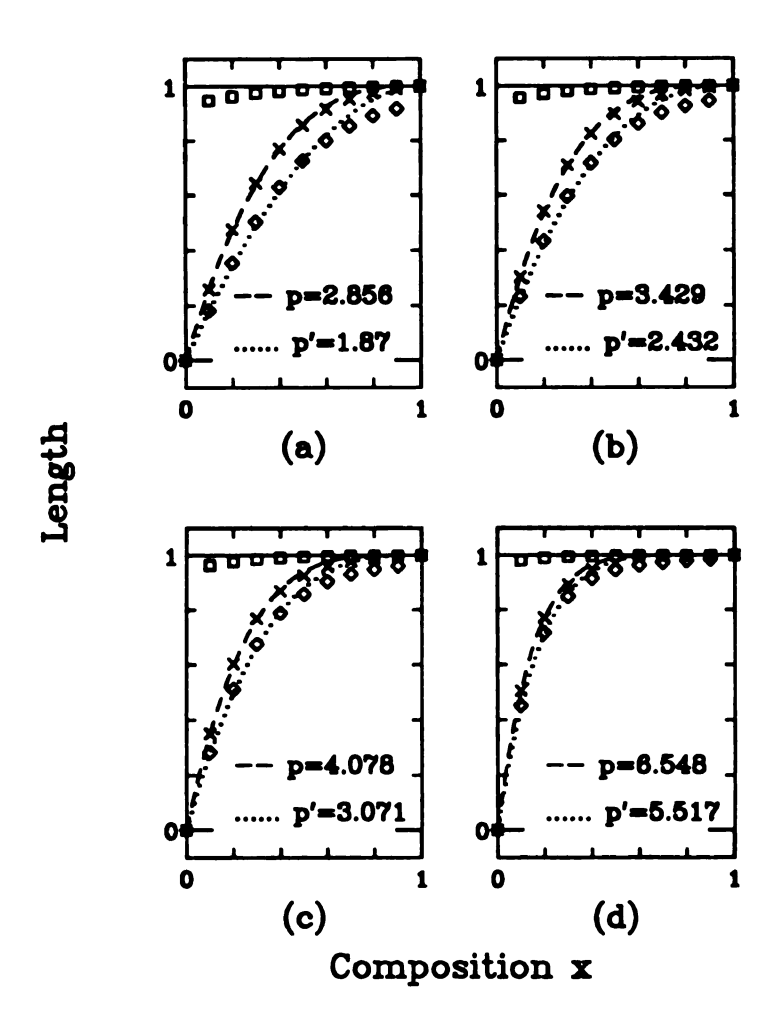


Figure 3.7: Comparison of the simulation results obtained with the LJ potential model to the catchment area model,  $\langle d \rangle = 1 - (1-x)^p$ . Four different values of  $K_A/K_B$  are used [(a) 0.1, (b) 0.07, (c) 0.05, and (d) 0.02];  $K_T/K_B = 0.1$ .

to expand the small atoms. Also we find that for a fixed  $K_A/K_B$ , p increases with the transverse layer rigidity  $K_T/K_B$ . Thus, the parameter p somehow incorporates the effects of transverse layer rigidity of the host layers and different intercalant compressibilities.

In Figure 3.7, we find that the mean gallery separation (d) obtained in the LJ potential model (simulation results) fits the curve  $1 - (1 - x)^p$  well even if the simulation results are slightly below the CAM curve for values of x > 0.5. Similarly, the simulation results for  $(d_A)$  fit rather well the analytic form  $1 - (1-x)^{p-1}$  for x < 0.5 and there are some deviations for x > 0.5. There is also deviation for  $(d_B)$  in the small x limit. Several conclusions can be drawn from Figure 3.7. First, each figure shows smaller deviation in the total average gallery spacing than an average gallery spacing associated with each intercalant (A or B). This can be explained by the probability of contributions of average spacing of each intercalant to  $\langle d \rangle$ . Namely, as  $x \to 1(0)$ , the contribution of small (large) intercalants to the total average gallery spacing becomes small. Secondly, the gallery expansion of our system is smaller than that for the hard sphere model because expansion of the small intercalants to  $h_B^0$  costs finite amount of energy unlike the hard sphere model. Therefore the height of an A-atom is somewhere between  $h_A^0$  and  $h_B^0$ , not exactly  $h_B^0$ . In real systems, it is possible for the intercalants to expand or compress within the healing length because the intercalants have finite compressibilities. We believe that if experiments can be performed for the average gallery spacing of each intercalant, the results will be closer to that obtained via the anharmonic potential model. The CAM somehow incorporates two important physical effects, the compressibility ratio of the two atoms and the transverse layer rigidity. However, it is strictly valid in the limit  $K_A/K_B=0$ . For finite  $K_A/K_B$ ,  $\langle d_B \rangle$  deviates from 1 and  $\langle d_A \rangle$  is less than 1 in

the limit  $x \to 1$  and these deviations become less significant as the layers become more rigid.

There is an improved form of the CAM to be denoted as the generalized catchment area model [12]. Since the expansion of atoms costs energy, the equilibrium length of a small atom lies somewhere between  $h_A^0$  and  $h_B^0$  which can be considered by introducing an additional parameter,  $\alpha$ , for  $\langle d_A \rangle$  besides p. The parameter  $\alpha$  is the value of  $\langle d_A \rangle$  in the limit  $x \to 1$ .

$$\langle d_A \rangle = \alpha (1 - (1 - x)^{p'}),$$
 (3.41)

where p' = p - 1. The effect of the softening of hard sphere model for a large atom has been considered. A single large impurity (B atom) has height  $\beta$  and is surrounded by a soft catchment area of small atoms with area p' = p - 1 with height  $\alpha$ . If a large atom is surrounded by one or more large atoms, its normalized height is 1. Therefore,

$$\langle d_B \rangle = 1 - (1 - \beta)(1 - x)^{p'}.$$
 (3.42)

From the relation  $\langle d \rangle = (1-x)\langle d_A \rangle + x \langle d_B \rangle$ , we get

$$\langle d \rangle = \alpha (1 - (1 - x)^p) + (1 - \alpha) * x - (1 - \beta) x (1 - x)^{p'}. \tag{3.43}$$

Figure 3.8 shows an excellent agreement with numerical simulations of LJ model. Let us compare the parameters p' of CAM with that of the generalized CAM. The generalized CAM allows for A(B) atoms inside the catchment area to have intermediate heights  $\alpha(\beta)$ . Therefore, within this model, relaxation of A atoms propagates to a larger distance than that in the CAM. This explains the larger values of p' (therefore p) in the modified CAM compared to those obtained in the CAM.

The generalized CAM obeys the following relation which can be obtained from Eqs. (3.41) and (3.42).

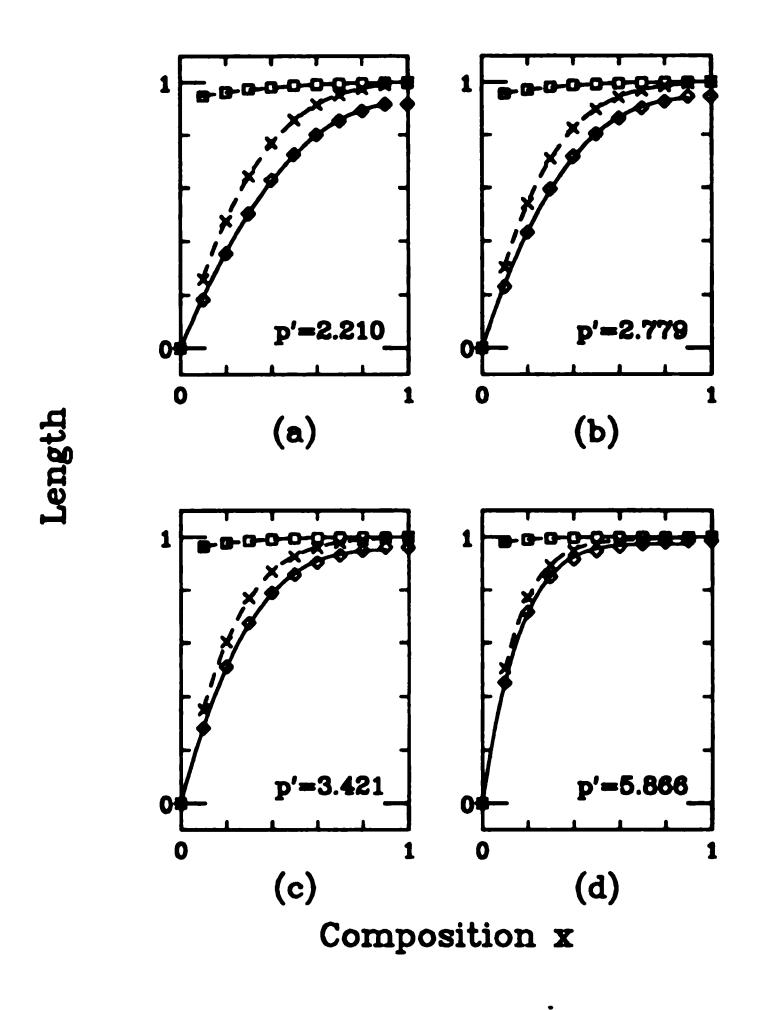


Figure 3.8: Same as Figure 3.7 except that simulation results are fitted with Eq. (3.41) and Eq. (3.42). The dimensionless catchment area (p' = p - 1) is in the figure. Parameters  $(\alpha, \beta)$  for  $(d_A)$  and  $(d_B)$  are as follows. (a) (0.922, 0.937), (b) (0.940, 0.944), (c) (0.952, 0.950), and (d) (0.973, 0.964).

$$\frac{d_A(x)}{d_A(1)} = \frac{d_B(x) - d_B(0)}{1 - d_B(0)}. (3.44)$$

Figure 3.9 is a plot of this relation with LJ simulation data. As  $K_A/K_B$  decreases, the LJ results show deviation from the relation because the generalized CAM treats the softness of large and small atoms in a symmetric way whereas in the case of LJ simulation, the asymmetric shape of anharmonic potential gives different amount of expansion and contraction. This suggests that the effect of the softness of the large and small atoms should be considered differently. As  $K_A/K_B$  decreases, this effect is more pronounced as we see from the figure.

Although we have compared the generalized CAM with LJ simulation keeping  $K_T/K_B$  fixed and varying  $K_A/K_B$ , we believe similar agreement between the two will be obtained for different  $K_T/K_B$  but fixed  $K_A/K_B$ .

#### 3.7 Conclusion

In summary, we have studied the gallery expansion of ternary intercalated systems within anharmonic potential models. We find that the anharmonicity is important in layered ternary systems, especially for low concentration of small intercalants (i.e.  $x \to 1$ ). When the compressibilities of the two intercalants are the same, one obtains Vegard's law within a harmonic model. On the other hand, the inclusion of anharmonicity gives rise to deviations from Vegard's law. These deviations increase with increase in the transverse layer rigidity. Effective medium approximation appears to be adequate for small anharmonicity, and in the limit of small and large layer rigidity. The results of the "Catchment Area Model" can be understood within a Lennard Jones model and simple generalization to the CAM can be made to fit the gallery expansion obtained within LJ model very well.

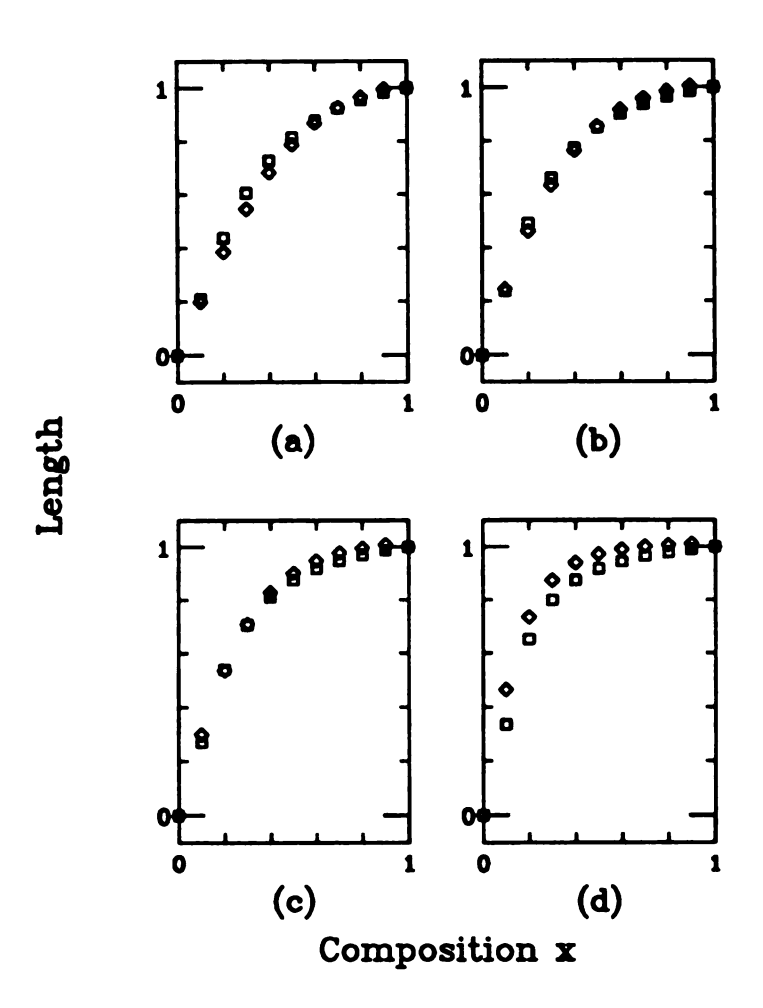


Figure 3.9: Plot of Eq. (3.44) by using LJ simulation results of  $\langle d_A \rangle$  and  $\langle d_B \rangle$ .

# **Bibliography**

- [1] F. S. Galasso, Structure and Properties of Inorganic Solids (Pergammon, New York, 1970).
- [2] L. Vegard, Z. Phys. 5, 17 (1921).
- [3] Y. Cai and M.F. Thorpe, Phys. Rev. B 46, 15879 (1992).
- [4] J. B. Thompson, in Researches in Geochemistry, Vol. II, ed. by P. H. Abelson, (wiley, New York, 1967) p. 340.
- [5] J. R. Dahn, D. C. Dahn, and R. R. Haering, Solid State Comm. 42, 179 (1982).
- [6] J. E. Fisher and H. J. Kim, Phys. Rev. B 35, 3295 (1987).
- [7] S. A. Solin and H. Zabel, Adv. Phys. 37, 87 (1988).
- [8] P. C. Chow and H. Zabel, Phys. Rev. B 38, 12837 (1988).
- [9] D. Medjahed, R. Merlin, and R. Clarks, Phys. Rev. B 36, 9345 (1987).
- [10] W. Jin and S. D. Mahanti, Phys. Rev. B 37, 8647 (1988).
- [11] H. Kim, W. Jin, S. Lee, P. Zhou, T. J. Pinnavaia, S. D. Mahanti, and S. A. Solin, Phys. Rev. Lett. 60, 2168 (1988); S. Lee, S. A. Solin, W. Jin and S. D. Mahanti, in Graphite Intercalation Compounds: Science and Technology, Ed. by

- M. Endoh, M. S. Dressellhaus and G. Dressellhaus, p. 41 (Materials Research Society, 1988).
- [12] M. F. Thorpe, Phys. Rev. B 39, 10370 (1989); unpublished.
- [13] S. Lee, H. Miyazaki, S. D. Mahanti, and S. A. Solin, Phy. Rev. Lett. 62, 3066 (1989).
- [14] M.F. Thorpe, W. Jin, and S.D. Mahanti, Phys. Rev. B 40, 10294 (1989); Disorder in Condensed Matter Physics, Ed. by J.A. Blackman and J. Tagüeña, p.22 (Clarendon, Oxford, 1991); M.F. Thorpe and S.D. Mahanti, Lectures given at NATO Summer School, "Chemical Physics of Intercalation II", Chateau de Bonas, France, 1992; Lectures given at the 7th International School on Condensed Matter Physics, Varna, Bulgaria, 1992.
- [15] Y. Cai, J. S. Chung, M. F. Thorpe and S. D. Mahanti, Phys. Rev. B 42, 8827 (1990).
- [16] Hyangsuk Seong, Jean S. Chung, and S. D. Mahanti, Bull. Am. Phys. Soc. 35, 781 (1990); preprint.
- [17] N. Bernardes, Phys. Rev. 112, 1534 (1958).
- [18] C. Kittel, Introduction to solid state physics, (5th ed., McGraw-Hill, 1977)
  p. 77.
- [19] S. Feng, M. F. Thorpe, and E. Garboczi, Phys. Rev. B 31, 276 (1985).
- [20] W. M. Press, B. P. Flannery, S. A. Teukolsky, and W. T. Vettering, Numerical Recipes (Cambridge University Press, 1986) p. 301.
- [21] T. Horiguchi, J. Math. Phys. 13, 1411 (1972).

# Chapter 4

# Structure of 2-Dimensional (2D) Repulsive Screened Coulomb Systems/ Model Intercalation Compounds

#### 4.1 Introduction

Structural and dynamic properties of systems with competing interactions continue to be one of the most interesting areas of condensed matter physics [1]. Of particular interest over the past decade has been the study of structural properties of binary and ternary graphite intercalation compounds (GICs) [2, 3]. The interplay between intercalant-intercalant interactions and graphite-intercalant interactions are ultimately responsible for the intercalation process. Furthermore, depending on these competing interactions which are naturally sensitive to the choice of intercalants and their planar densities, various structural features appear. Considerable amount of experimental [2, 3] and theoretical [4] works have helped in elucidating many of the interesting physical properties of these systems. The stage  $n \geq 2$  GICs have provided rich sources for the study of structural properties and phase transitions in two dimensions. However, one area where a detailed microscopic

understanding is still lacking is the incommensurability of stage- $n(n \ge 2)$  GICs containing Cs, Rb, and K atoms as intercalants. We address this issue by probing the structure of domains and domain walls using Molecular Dynamics (MD) simulations and then propose a simple model for the low temperature structure of the alkali GICs. Although both X-ray and neutron diffraction studies have been crucial to the elucidation of the structure, in this chapter we will consider only X-ray diffraction experiments since both yield the same results on structures. In addition, quasi-elastic and inelastic neutron scattering studies have been of great importance for understanding the dynamics of GICs and will be discussed in chapters 6 and 7.

### 4.2 Physical Systems

Pure graphite is characterized by a layered structure, originating from a strong covalent bonding of the carbon atoms in the plane and weak Van der Waals coupling between the planes. The in-plane C-C bond length is  $1.42\text{\AA}$ , and the interlayer spacing is  $3.35\text{\AA}$  (see the upper panel in Figure 4.1). The planes are arranged together in the sequence ABA and are related to each other by the translation vector  $\mathbf{g} = (2\mathbf{a} - \mathbf{b})/3$ , where  $\mathbf{a}$  and  $\mathbf{b}$  are basis vectors of the graphite unit cell. Under appropriate conditions of graphite temperature and alkali vapor pressure [5], intercalation of alkali atoms into the graphite interlayer spacings occurs. The intercalated atoms lead to three main structural changes of the graphite hosts. First, 'staging' where the alkali atoms intercalate in a regular fashion so that an intercalated layer is followed by a constant number (n) of graphite planes, i.e. stage-n GICs are characterized by a stacking sequence of graphitic and intercalant layers in which the neighboring intercalant layers are separated by n graphitic layers (see the lower panel in Figure 4.1). Second, alkali layers are always flanked by equivalent car-

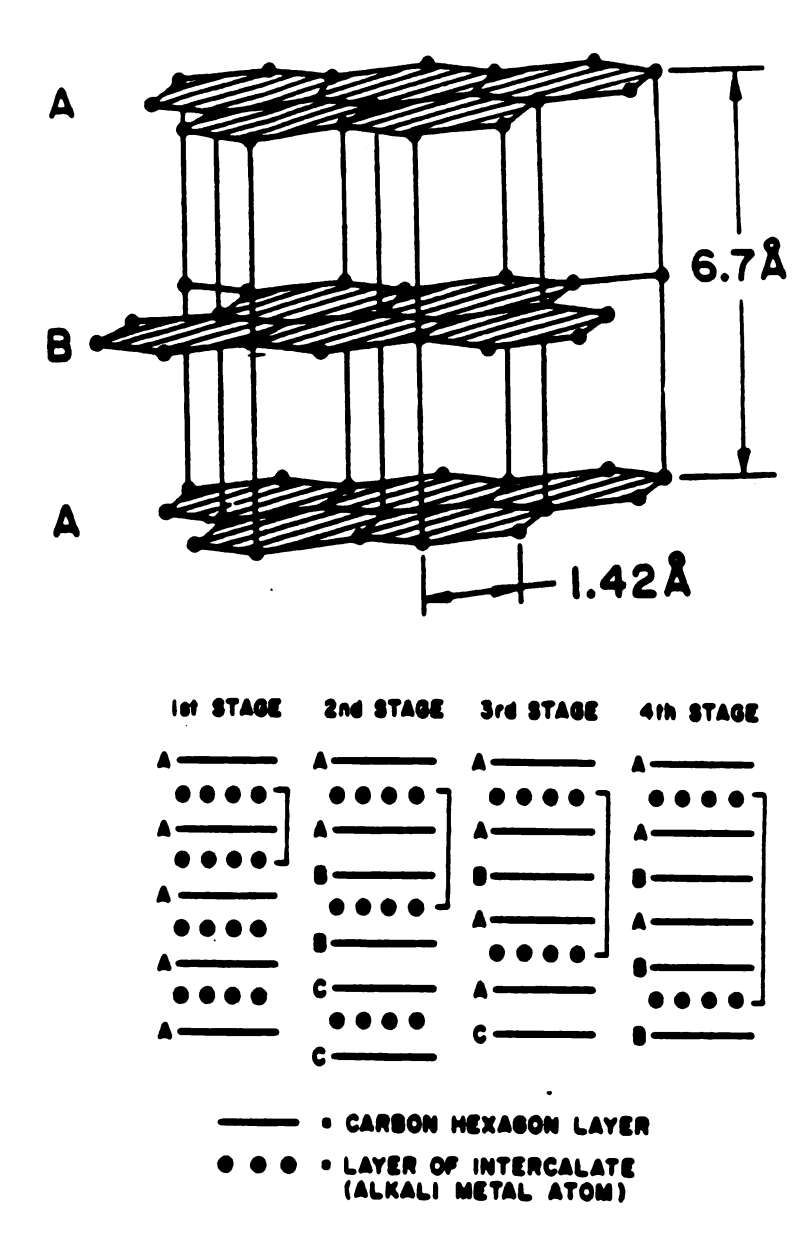


Figure 4.1: Upper panel is a structure of graphite. Lower panel shows stacking sequence of carbon and alkali layers.

bon planes, thereby causing a rearrangement of the stacking order of the graphite. Third, the interlayer spacing of adjacent graphite planes increases considerably (e.g. from 3.35  $\mathring{A}$  to 5.71  $\mathring{A}$  for Rb) upon intercalation, while the in-plane structure of the graphite remains almost unaffected. During intercalation, approximately one electron per alkali atom is transferred to the graphite. Experiments indicate that these extra electrons not only compensate for the charge of the remaining ionic alkali layers but also screen them [6]. The intercalant ions interact predominantly via screened Coulomb repulsion and feel an effective one particle corrugation potential produced by the graphite layers. Thus, these systems exhibit a competition between two length scales, periodicity of the substrate corrugation potential and the average separation between the intercalant ions controlled by their planar density  $(\rho)$ . In addition, there is also a competition between two energy scales, the interaction energy/particle and the depth of the corrugation potential which is determined by  $\rho$  and the strength of the interparticle interaction.

In stage-1 GICs of K, Rb, and Cs, the intercalants form a commensurate triangular  $(2 \times 2)R0^{\circ}$  structure where  $R0^{\circ}$  and  $(2 \times 2)$  imply that the unit cell vectors of the intercalant superlattice are parallel to the graphite unit cell (a, b) and are twice as large. The layer stoichiometry is  $AC_8$ , where A stands for the intercalant and C for the carbon (note there are two carbon atoms per graphite unit cell). This gives  $\rho = 1/4$  (in units of 1/area of the graphite unit cell). In contrast, structures of stage-n ( $n \ge 2$ ) systems are more intriguing. Chemical stoichiometry of these compounds is in general  $AC_{12n}$  and the layer stoichiometry is  $AC_{12}$ , giving  $\rho = 1/6$ . In the absence of the corrugation potential, the ground state is a triangular lattice with an arbitrary orientational epitaxy angle  $\phi$  (measured with respect to graphite reciprocal lattice vector  $\mathbf{a}^*$ -axis, also known as Novaco-McTague angle [7]). A question

of fundamental interest is the effect of corrugation both on the intercalant structure and the intercalant dynamics.

The liquid state structure in stage-2 compounds is well understood through careful MD work of Moss et al. [8, 9, 10] and Chen et al. [11] in terms of a highly structured liquid close to the liquid-solid phase transition. The nature of the solid structure is, however, not as well understood although qualitative models have been proposed by Clarke et al. [12, 13] for  $AC_{24}(A = Cs, Rb, \text{ and } K)$  in terms of different types of commensurate domains separated by discommensurations (domain walls). Also Ginzburg-Landau models have been proposed to understand the domain structure [14]-[17]. From X-ray diffraction measurements in  $CsC_{24}$  and  $RbC_{24}$ , Clarke et al. [12, 13] suggested the coexistence of commensurate  $(\sqrt{7} \times \sqrt{7})$  and  $(2 \times 2)$ regions. They explained their diffraction results for Cs by postulating the coexistence of  $(\sqrt{7} \times \sqrt{7})$  R $\phi$  domains with  $\phi = (+/-)19.11^{\circ}$ . The commensurate domains were of size  $\sim 40$ Å containing about 30 Cs atoms along with narrow domain walls oriented parallel to the graphite (110) directions (see Figure 3 in ref. [12]). They, however, neither discussed the precise nature of the domain walls nor analyzed the spatial distributions and relative amounts of  $(\sqrt{7} \times \sqrt{7})$  and  $(2 \times 2)$  domains, the latter being determined by the density constraint. In the case of RbC24, it was not quite clear whether  $(2 \times 2)$  domains were present or not.

Following the suggestions of Clarke et al. [12], several theoretical studies based on Ginzburg-Landau theory of discommensuration in the incommensurate phase were carried out pointing out the importance of third order terms in stabilizing the  $(\sqrt{7} \times \sqrt{7})$  domains [14]-[17]. These theories were able to explain the observed Novaco-McTague angle  $\phi$  and intensities of the higher order superlattice reflections semiquantitatively, although they did not address the structure of the domain walls

in detail. As we will show later, domain and domain wall sizes in these systems are comparable and one should therefore also know the microscopic structure of the walls.

#### 4.3 Potential Model

MD simulations were carried out for  $RbC_{24}$  using the potential model of Ref. [11]. The one particle corrugation potential in this model was obtained by Moss *et al.* [8] by comparing the liquid structure factor  $S(\mathbf{k})$  with X-ray experiment and is given by

$$V_1(\mathbf{r}) = -2K[2\cos(2\pi x/a)\cos(2\pi y/\sqrt{3}a) + \cos(4\pi y/\sqrt{3}a)]. \tag{4.1}$$

with 2K = 0.9 (in units of  $300k_B$ ) i.e.  $2K/k_B = 270K$ , and  $a = 2.46\text{\AA}$  which is the graphite unit cell constant. The two-body potential is given by

$$V_2 = q^2 \sum_{ij} \exp(-\Gamma r_{ij}) / r_{ij}, \tag{4.2}$$

with  $q = 4.8028 \times 10^{-10}$  esu and  $\Gamma = 0.49 \mathring{A}^{-1}$ .

The above potential has successfully reproduced the liquid structure data at 250K. Our MD simulations using constant energy algorithms agree with the earlier results of Chen et al. [11]. Before discussing the solid structure results, let us discuss some energetics. The strength of the corrugation potential as measured by  $V_1^{saddle} - V_1^{min} = 1080 \text{K}$  i.e. we are in the strong to intermediate corrugation limit for T < 300 K. The energy/particle for different commensurate structures are 17742K  $(\sqrt{3} \times \sqrt{3})$ ; 9825K  $(2 \times 2)$ ; 4476K  $(2 \times 3)$ ; 3114K  $(\sqrt{7} \times \sqrt{7})$ . Although the  $(2 \times 3)$  structure has the correct layer density, the lower energy of the  $(\sqrt{7} \times \sqrt{7})$  structure favours the latter.

We can generalize this problem by changing parameters which appear at Eqs. (4.1) and (4.2). When 2K=0, the system corresponds to a purely 2D repulsive screened Coulomb system. As 2K is increased, the effect of host layers (or substrates) increases and how the physical properties change with 2K will be discussed in chapters 5-7. As we change  $\Gamma$ , the interaction between intercalants (or adsorbates) varies from purely Coulomb ( $\Gamma=0$ , long range) interaction to highly screened Coulomb ( $\Gamma\to\infty$ , very short range) interaction. This chapter will focus on a system with 2K=0.9 and  $\Gamma=0.49$  appropriate for stage-2 Rb GIC [11].

#### 4.4 Details of Molecular Dynamics Simulations

MD simulations were performed with 216 and with 864 Rb ions distributed to insure a planar density of  $\rho=0.0318$  Rb ions/ $\mathring{A}^2$  for the stage-2  $RbC_{24}$  system. In addition to this planar density, we have also studied a 301 particle system with a slightly smaller density of  $\rho$  (0.0311 Rb ions/ $\mathring{A}^2$ ) which corresponds to the stage-2  $RbC_{24.57}$  system to see the effect of change in the density on the ground state structure. MD simulations were carried out using a sixth order Gear predictor-corrector algorithm [16] to solve the Newton's equations with periodic boundary conditions. The time step was taken to be 0.0029 picosecond (ps) and typical equilibration times of at least 350 ps were used for 216- and 301-particle systems and 1 nanosecond (ns) for 864-particle systems, respectively. The energy/ion was noted to be conserved to 99.994% accuracy over 150 ps run for these systems. The range of the two-body potential was kept within a circle of radius 27.06 $\mathring{A}$  centered on any Rb ions. The results remained essentially the same when a larger cut off radius was used.

Most of the simulations were carried out in the temperature range 100 K < T < 300 K and in some cases we cooled down the system to as low as 3 K. The 216-particle

system was initially heated from a triangular structure and allowed to melt and to equilibrate. It was then slowly cooled in temperature intervals of 10K through the transition region. Finally the cooled solid was slowly heated to see whether liquid-solid transition showed hysteresis or not. For the  $RbC_{24.57}$  system we chose a different initial configuration in order not to bias our simulations towards any particular ordered structure as its ground state. For this system we started from a random configuration; this corresponded to an extremely hot nonequilibrium system. The system was cooled down rather quickly to 300K from the initial nonequilibrium temperature of  $\sim 10^4 \text{K}$  and was allowed to equilibrate at that temperature for sufficiently long time. We then slowly cooled the system by temperature intervals of 10K until the ground state was reached. It turned out to be a Periodic Domain Wall solid. This solid was then slowly heated to probe the solid-liquid transition. For these systems, all results of cooling and heating runs were compared to ensure that thermal equilibrium was achieved.

Here we report our results for two different temperatures, 250K (liquid) and 3K (solid) [18]. The study of the melting transition will be given in chapter 5 [19] and dynamics of these systems will be studied in chapters 6 and 7.

### 4.5 Structural Properties

The structure of simple monatomic fluids is characterized by a set of distribution functions for the atomic positions, the simplest of which is the pair distribution function g(r) which gives the probability of finding a pair of atoms a distance r apart.

$$g(\mathbf{r}) = \frac{A}{N^2} \langle \sum_{i} \sum_{j \neq i} \delta(\mathbf{r} - \mathbf{r}_{ij}) \rangle \tag{4.3}$$

where A is the area of the MD cell, N is the number of Rb ions in the cell and the angular brackets imply a time average. In Figure 4.2 (a) and (b) we give the spherically averaged real space pair distribution function g(r) for the solid and the liquid, respectively. Clearly, the liquid is strongly perturbed by the host layer at this temperature and is **structured**, as noted earlier by Fan et al. [9] and Chen et al. [11] following the earlier suggestion by Parry [20] for  $CsC_{24}$ .

The solid phase g(r) shows three distinct peaks at 2.19, 2.53, and 2.97 in units of graphite unit cell length and these can be related to distances of 2,  $\sqrt{7}$ , and 3, respectively [21]. A similar three-peak structure was obtained from a Monte Carlo study by Plischke et al. [22] and suggests that the system may show coexisting domains of  $(\sqrt{7} \times \sqrt{7})$  and  $(2 \times 2)$  consistent with the picture proposed by Clarke et al. [12] for CsC24. The positions of the intercalants joined by lines connecting nearest neighbours using Voronoi polyhedra constructions [23] are shown in Figure 4.3 (a) and (b) corresponding to two different concentrations of Rb atoms ( $RbC_{24}$  and  $RbC_{24.57}$ ). In contrast to the picture of Clarke et al. for  $CsC_{24}$  (presence of large domains of  $(\sqrt{7} \times \sqrt{7})$  structure containing about 30 atoms oriented in different directions and separated by narrow domain walls of unknown atomic structure), we see placquettes of  $(\sqrt{7} \times \sqrt{7})$  structure consisting mostly of 7 atoms (we will call these nano-domains) for RbC<sub>24</sub> (Figure 4.3 (a)). The intersection of three such placquettes forms a triangular placquette of  $(2 \times 2)$  structure containing 3 atoms. The walls between two  $(\sqrt{7} \times \sqrt{7})$  nano-domains consist of  $(2 \times 3 \times \sqrt{7})$  triangular placquettes which give rise to the peak near 3 in g(r). These domain walls should also give a peak corresponding to r near  $\sqrt{13} = 3.6$  which we also find in g(r) (see Figure 4.2(b)). Our MD simulations give a picture rather similar to the one suggested by Zabel et al. [24] for  $RbC_{24}$  (see their Figure 1 and figures in ref. [25]).

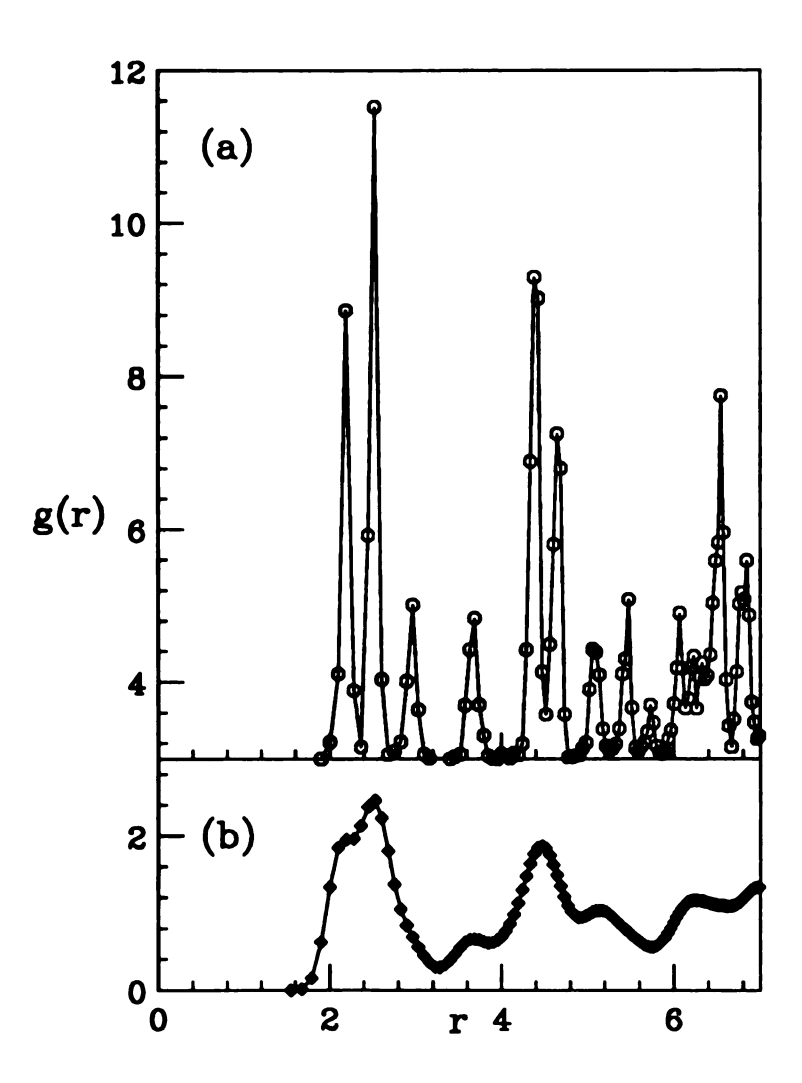


Figure 4.2: Pair correlation function g(r) for  $RbC_{24}$  as a function of r (in units of graphite lattice constant  $a=2.46\text{\AA}$ ) (a) for the solid at 3K (upper panel) for the 216 particle system and (b) for the liquid at 250K (lower panel). Note that the zero for the solid is 3.

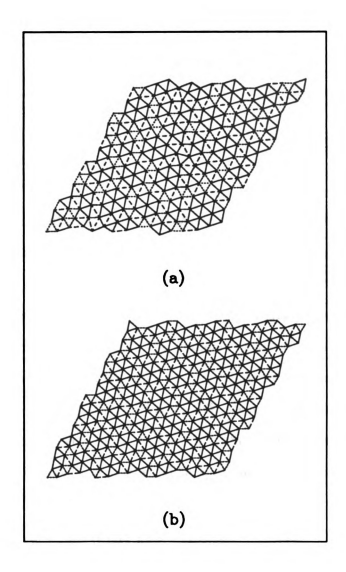


Figure 4.3: Low temperature solid structure of (a)  $RbC_{24}$  and (b)  $RbC_{24.57}$ . The solid, dotted, and dashed lines correspond to the nearest neighbor distances near  $\sqrt{7}$ , 2, and 3 (in units of graphite lattice constant), respectively.

In fact, by choosing a slightly smaller density of Rb ions we see a perfectly ordered arrangement of  $\sqrt{7} \times \sqrt{7}$  domains with  $(2 \times 3)$  domain walls.

To compare the MD results with X-ray diffraction measurements we calculate the structure factor  $S(\mathbf{k})$  for the atomic positions given in Figure 4.3 (a). The static structure factor is defined as follows,

$$S(\mathbf{k}) = \frac{1}{N} \left\langle \left| \sum_{j} e^{i\mathbf{k} \cdot \mathbf{r}_{j}(t)} \right|^{2} \right\rangle, \tag{4.4}$$

where  $\mathbf{r}_j(t)$  is the position of the j-th particle at time t. The structure factor for the solid phase (216 particle system) is given in Figure 4.4. Our MD simulation shows two prominent peaks ( $I_1$  and  $I_2$ ) at the same magnitude of wave vector  $k_p = 1.21 \text{Å}^{-1}$  but different angles with respect to the graphite reciprocal lattice vector  $\mathbf{a}^*$ -axis. The angle associated with the dominant peak  $I_1$ , denoted as  $\phi$ , is 10.2° whereas that associated with the weak peak  $I_2$  which we denote as  $\psi$  is 35.8°. The strengths of these two peaks are 0.52 and 0.052, respectively. There is a third peak  $I_3$  ( $k = 1.40 \text{Å}^{-1}$ , angle with the  $\mathbf{a}^*$ -axis is 7.6°) which is very weak (strength 0.015) and will not be discussed any further. The  $k_p$  values and angles of the two strong peaks measured from the graphite  $\mathbf{a}^*$ -axis are given in Table 4.1 along with the available experimental values and predictions of the Periodic Domain Wall Model to be described in the next section.

Clarke et al. [12] saw two peaks similar to  $I_1$  and  $I_2$  in  $CsC_{24}$  (1 and 2 in their notation in ref. [12]). The corresponding  $k_p$  and angles  $\phi$  and  $\psi$  are given in the Table 4.1. In addition, they also saw a peak as strong as  $I_1$  (1' in their notation) which originated from the rotational equivalent of  $I_1$  corresponding to the Novaco McTague angle  $-\phi$ . The origin of the low intensity peak  $I_2$  was ascribed by Clarke et al. to the inter-domain scattering associated with the coexistence of two

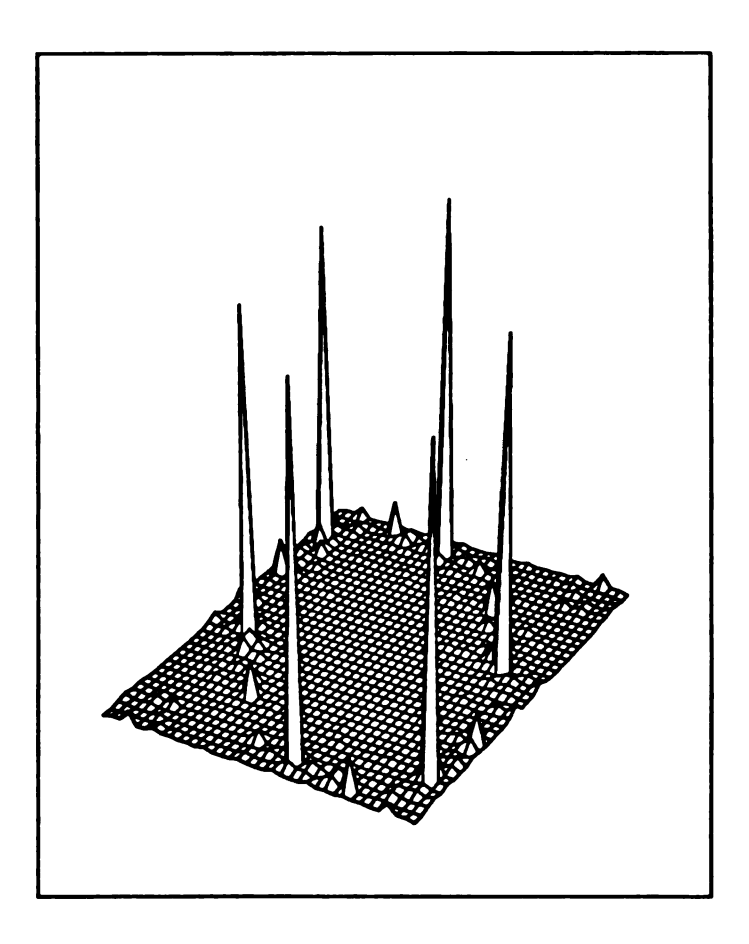


Figure 4.4: Structure factor S(k) for k in the  $k_x$ - $k_y$  plane for  $RbC_{24}$  at 3K obtained from MD simulations for the 216 particle system. Only the dominant peaks  $I_1, I_2$  (see Ref. [18]) and their six-fold symmetry counterparts are clearly visible.

Table 4.1: Comparison of angles and peak positions of S(k) between Experiment (EXP), Molecular Dynamics (MD), and Periodic Domain Wall Model (PDW) (see text).  $\phi = \text{Novaco McTague angle}$ ;  $\psi = \text{angle of the peak produced by inter-domain scattering (angle of <math>I_2$  in Ref. [13]);  $k_p$  is the magnitude of k at angles  $\phi$  and  $\psi$ .

	$\phi \ (\psi)$			$k_p$		
	EXP	MD	PDW	EXP	MD	PDW
$RbC_{24}$	10.1 (35.5)	10.2 (35.8)	11.5(33.3)*	1.22	1.21	1.19*
$CsC_{24}$	14.5 (28)	? (?)	14.5(27.6) <sup>b</sup>	1.16	?	1.15 <sup>b</sup>

<sup>•</sup> for L=M=1  $(RbC_{24.57})$ 

different orientations of  $(\sqrt{7} \times \sqrt{7})$  commensurate domains. Our MD simulations show only one orientation of these domains (either 1 or 1') thus indicating that it is not necessary to invoke domains with different orientations to explain the origin of the  $I_2$  peak. It is sufficient to have domain walls, in our case the two domains sandwiching a wall being simply shifted with respect to one another by two units of a graphite lattice vector. For  $RbC_{24}$  the dominant peak  $I_1(k_p = 1.22 \mathring{A}^{-1}, \phi = 10.1^\circ)$  [12] is in good agreement with our MD results. The lower intensity peak  $(I_2)$  for this system was not discussed in Ref. [13] but the corresponding  $k_p$  and the angle  $\psi$  agree very well with the X-ray diffraction results of Rousseaux et al. [27].

The liquid state  $S(\mathbf{k})$  at 250K (in Figure 4.5) shows clearly the effect of graphite host layer with the dominant anisotropic peak at  $k = 1.2 \text{Å}^{-1}$  corresponding to a corrugated liquid [26]. The inset in Figure 4.5 shows the S(k) averaged over angle. The sharp peak near  $3 \text{Å}^{-1}$  is a result of the graphite corrugation potential.

b for L=2, M=1  $(CsC_{26.1})$ 

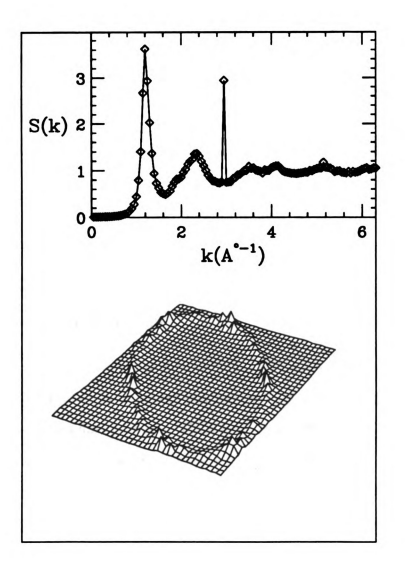


Figure 4.5: The liquid structure factor  $S(\mathbf{k})$  for  $\mathbf{k}$  in the  $k_x$ - $k_y$  plane for  $RbC_{24}$  near  $T\!=\!250\mathrm{K}$  shows an anisotropic ridge due to the effect of corrugation. The inset is S(k) averaged over angle.

#### 4.6 Periodic Domain Wall Model

To understand more about the physical origin of the two peaks discussed in the previous section, we propose a Periodic Domain Wall (PDW) model which consists of periodic arrays of commensurate ( $\sqrt{7} \times \sqrt{7}$ ) domains of total width 2L (all of same orientation) interspersed by domain walls of width M (in units of 2a). The domain walls consist of (2 × 3) regions and the region where three domains meet consists of a triangular array of (2 × 2) structure (see Figure 4.3(b)). For arbitrary (L, M) the super-lattice unit cell is obtained by joining the centers of the ( $\sqrt{7} \times \sqrt{7}$ ) domains and the unit cell vectors are given by

$$\mathbf{A} = 2(2\mathbf{L} + \mathbf{M})\mathbf{a} + \mathbf{L}\mathbf{b},\tag{4.5}$$

$$\mathbf{B} = -\mathbf{L}\mathbf{a} + (5\mathbf{L} + 2\mathbf{M})\mathbf{b},\tag{4.6}$$

where  $\mathbf{a} = a\hat{x}$  and  $\mathbf{b} = (a/2)\hat{x} + (\sqrt{3}a/2)\hat{y}$ ,  $\hat{x}$  being a unit vector along the (10) direction of a graphite in real space and  $\hat{y}$  being a unit vector perpendicular to  $\hat{x}$  in a right handed coordinated frame. The size of super-cell is  $a\sqrt{21L^2 + 18ML + 4M^2}$ . One often considers this as the domain size due to unknown nature of the narrow domain-wall structure. However, in our case, domain is clearly defined and its size is obtained by putting M=0 i.e.  $aL\sqrt{21}$ . The reciprocal lattice vectors corresponding to the super-lattice unit cell vectors are

$$\mathbf{K}_{A} = \frac{2\pi(5L+2M)}{a(21L^{2}+18LM+4M^{2})}(\hat{x}-\frac{3L+2M}{\sqrt{3}(5L+2M)}\hat{y}), \tag{4.7}$$

$$\mathbf{K}_{B} = -\frac{2\pi L}{a(21L^{2} + 18LM + 4M^{2})} (\hat{x} - \frac{9L + 4M}{\sqrt{3}L} \hat{y}). \tag{4.8}$$

The density in the PDW model is determined by (L, M). The number  $(N_{Rb})$  of Rb ions in the super-cell is  $3L(L+M)+M^2$  where as the number  $(N_C)$  of Carbon atoms in it is  $2(21L^2+18ML+4M^2)$ . Therefore, we can obtain a planar density from  $N_{Rb}$ 

and  $N_C$  for given (L, M). Also  $m = N_C/N_{Rb}$  can be used for the nomenclature of stage- $n \ge 2$  GICs as  $AC_{nm}$  where A stands for the intercalants. In this model one goes from the commensurate  $(\sqrt{7} \times \sqrt{7})$  structure (M=0, arbitrary L) whose layer stoichiometry is  $AC_{14}$  to the commensurate (2 × 2) structure (arbitrary M, L=0) corresponding to  $AC_8$ .

Our MD simulations suggest that  $RbC_{24}$  can be described very well by adding a small number of Rb atoms to the PDW model with L=M=1 (this corresponds to the stoichiometry  $RbC_{24.57}$ ). To check this idea, we studied a 301 particle system with density of Rb ions corresponding to  $RbC_{24.57}$ . Figure 4.3(b) gives its low temperature structure. The structure factor for the defect-free case has been calculated exactly and the corresponding values of  $k_p$ , angles, and the strengths of the two peaks  $I_1$  and  $I_2$  are respectively (1.19, 1.19) $\mathring{A}^{-1}$ ; (11.5°, 33.3°); (0.573, 0.137) (see Table 4.1). The larger value of the intensity of the  $I_2$  peak in the PDW model (0.137) for  $RbC_{24.57}$  compared to the MD results (0.052) for  $RbC_{24}$  is due to the perfect ordering of the Rb ions in the PDW model.

We find by actual calculation that  $\phi$  (the Novaco-McTague angle) and  $\psi$  (the angle of the peak produced by inter-domain scattering, angle of  $I_2$  in Ref. [13]) satisfy the relation

$$\sin \psi = \sqrt{3}\sin(30 - \phi),\tag{4.9}$$

for the PDW model with M=1 and arbitrary L. In the limit L  $\rightarrow \infty$ , this relation gives  $\phi = \psi = 19.1^{\circ}$  i.e., the two peaks merge with each other for the commensurate  $(\sqrt{7} \times \sqrt{7})$  case. In Figure 4.6, we plot  $\psi$  and  $\phi$  for different values of  $k_p$  which is a measure of the layer density and is directly related to L and M by the reciprocal lattice vectors. This finding confirms that the appearance of the peak  $I_2$  originally

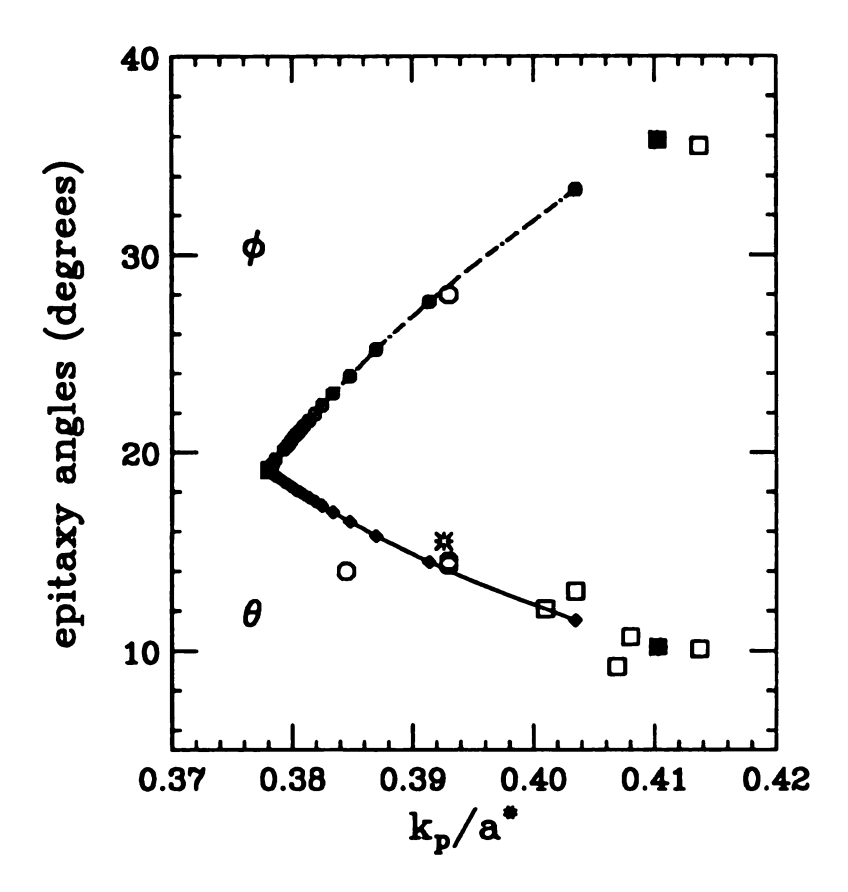


Figure 4.6: Novaco McTague angle  $\phi$  and the epitaxy angle  $\psi$  corresponding to the peak produced by inter-domain scattering as functions of domain size L with M=1 obtained within periodic domain wall model. Here,  $k_p$  along the x-axis varies as L and M change. Solid squares are our MD simulation results for  $RbC_{24}$ . White circles (squares) are various experimental results [2, 15] for  $RbC_{24}(CsC_{24})$ . A starlike symbol is an experimental result for  $CsC_{36}$ .

noted by Clarke et al. [12] is unrelated to the presence of domains of commensurate  $(\sqrt{7} \times \sqrt{7})$  region with two different orientations, namely  $\pm 19.11^{\circ}$ . Indeed, such configurations which generally require the Rb ions to be located closer than 2a in the regions between the domain walls (if we stick to the layer density of  $RbC_{12}$ ) are energetically unfavorable in view of the strongly repulsive two body potential between these ions. Furthermore, the  $CsC_{24}$  results of Clarke et al. [12] can be approximated by the L=2, M=1 PDW model which corresponds to a stoichiometry  $CsC_{26.1}$ , and gives  $k=1.15 \mathring{A}^{-1}$ ,  $\phi=14.5^{\circ}$ ,  $\psi=27.6^{\circ}$  in excellent agreements with the experimental values  $1.16 \mathring{A}^{-1}$ ,  $14.5^{\circ}$ , and  $28^{\circ}$  respectively. The corresponding intensities in the PDW model are respectively 0.568 and 0.144 and the number of Cs atoms in a domain is 19.

### 4.7 Summary and Conclusion

In summary, (i) the corrugation potential obtained by comparing the structure factor with X-ray scattering experiment in the liquid state can be successfully applied to the study of the low temperature microstructure in alkali GICs. The success of the chosen potential is confirmed by the agreement between the experimental  $S(\mathbf{k})$  and that obtained from our simulations for  $RbC_{24}$ . (ii) We also find that the simulated  $S(\mathbf{k})$  for the stage-2 GIC closely agrees with the experimental  $S(\mathbf{k})$  for stage-3 systems [13]. This observation confirms our original assumption concerning weak interlayer coupling and effective two-dimensionality of these alkali GICs. (iii) Simulations suggest that the real space structure of the Rb intercalants consists of thick domain walls lining the domains with length scales comparable to the domain walls. (iv) Finally, our  $S(\mathbf{k})$  calculations for the L=2, M=1 PDW model which recognizes the importance of the domain walls shows remarkable agreement with

experimental  $S(\mathbf{k})$  for the stage-2 Cs GIC. This last success indicates that the PDW model describes very well the main features of the low temperature structure of the stage-2 and higher GICs of Rb and Cs.

## **Bibliography**

- Competing Interactions and Microstructures: Statics and Dynamics, R. LeSar,
   A. Bishop, R. Hefner, eds., Springer (1988).
- [2] Graphite Intercalation Compounds, Vol 1: Structure and Dynamics, H. Zabel and S. A. Solin, eds. Springer Series on Topics in Current Physics, Springer (1990).
- [3] S. A. Solin and H. Zabel, Advances in Physics, 37, 87 (1988).
- [4] S. A. Safran, Solid State Physics vol. 40, ed. by H. Ehrenreich, and D. Turnbull, Academic Press (NY) (1987).
- [5] P.C. Eklund, Intercalation in Layered Materials, ed. M.S. Dresselhaus, Plenum, New York, p163 (1986).
- [6] J.E. Fisher, Physica, 99B, 383, (1980).
- [7] A. D. Novaco and J. P. McTague, Phys. Rev. Lett. 38, 1286 (1977).
- [8] S. C. Moss, et al., Phys. Rev. Lett. 57, 3191 (1986).
- [9] J. D. Fan, Omar A. Karim, G. Reiter, and S. C. Moss, Phys. Rev. B 39, 6111 (1989).
- [10] J. D. Fan, George Reiter, and S. C. Moss, Phys. Rev. Lett. 64, 188 (1990).

- [11] Zhuo-Min Chen, Omar A. Karim, and B. Montgomery Pettitt, J. Chem. Phys. 89(2), 1042 (1988).
- [12] Roy Clarke, J. N. Gray, H. Homma, and M. J. Winokur, Phys. Rev. Lett. 47, 1407 (1981).
- [13] M. J. Winokur and R. Clarke, Phys. Rev. Lett. 54, 811 (1985).
- [14] Y. Yamada and I. Naiki, Jour. Phys. Soc. of Japan, 51, 2174 (1982).
- [15] M. Suzuki and H. Suematsu, Jour. Phys. Soc. of Japan 52, 2761 (1983).
- [16] M. P. Allen and D. J. Tildesley, Computer Simulations in Liquids, Clarendone, Oxford (1987).
- [17] M. Suzuki, Phys. Rev. B 33, 1386 (1986).
- [18] Hyangsuk Seong, Surajit Sen, Tahir Çağin, and S. D. Mahanti Phys. Rev. B 45, 8841 (1992).
- [19] Hyangsuk Seong, S. D. Mahanti, Surajit Sen, and Tahir Çağin, Phys. Rev. B 46 (1992).
- [20] G. Parry, Mat. Sci. Eng. 31, 99 (1977).
- [21] Surajit Sen, Tahir Çağin, Hyangsuk Seong, and S. D. Mahanti, Recent Developments in Computer Simulation Studies in Condensed Matter Physics IV, ed. by D. P. Landau et al., Springer (1991).
- [22] M. Plischke and W. D. Leckie, Can. J. Phys. 60, 1139 (1982).
- [23] G.F. Voronoi, J. Reine, Angew. Math. 134, 198 (1908).
- [24] H. Zabel, et al., Phys. Rev. Lett. 57, 2041 (1986).

- [25] S. C. Moss and R. Moret in Ref.2.
- [26] H. Zabel, A. Magerl, J. J. Rush, and M. E. Misenheimer, Phys. Rev. B 40, 7616 (1989).
- [27] F. Rousseaux, R. Moret, D. Guerard, and P. Lagrange, Phys. B 42, 725 (1990);
  F. Rousseaux, et al., Synth. Met. 12, 45 (1985).

## Chapter 5

# Melting of a Repulsive Screened Coulomb System in 2D - Effect of Corrugation

#### 5.1 Introduction

Physical properties of two-dimensional (2D) solids and liquids and the nature of the solid-liquid transition continue to be of theoretical and experimental interest since the dislocation- and disclination-mediated melting ideas of Kosterlitz and Thouless [1], Nelson and Halperin [2], and Young [3]-[6]. The nature of the melting transition (whether first order driven by grain boundary melting [7] or continuous driven by unbinding of above topological defects) and the existence of the intermediate 'hexatic phase' with quasi long-range positional order and long-range bond orientational order sandwiched between the '2D solid' phase and the '2D isotropic liquid' phase are still uncertain [4].

In real physical systems such as atoms adsorbed on 2D substrates or intercalation compounds with sufficiently weak interlayer interaction which renders these systems quasi two-dimensional, the dominant effect of the substrate is the periodic corrugation potential. The latter affects the structures of both the solid and the liquid phases and the solid-liquid phase transition [2, 8, 9]. In particular, one has to take into account both the commensurability of the periodic potential and the strength of the corrugation. In the limit of weak corrugation, Nelson and Halperin [2] have argued that for an incommensurate potential the spatial variation of the Novaco-McTague angle [10] gives rise to a new elastic constant ( $\gamma$ ) in addition to the two usual Lamé constants ( $\lambda$  and  $\mu$ ) associated with a 2D isotropic elastic solid. The elastic constant  $\gamma$  determines the energy related to the spatial variation of the bond angle field in the presence of a finite substrate potential. Thus the corrugation potential acts as a field which couples to the bond orientational order parameter. Consequently, one has only the dislocation unbinding transition and the disclination unbinding transition is washed out just as a ferromagnetic transition gets washed out in the presence of a uniform magnetic field. For intermediate to strong incommensurate corrugation potential the precise nature of the transition is not known (see below the discussion in the lattice-gas limit).

When the corrugation potential is commensurate, the nature of the melting transition is profoundly affected. For coarse substrate mesh, the Kosterlitz-Thouless picture becomes inappropriate and even for a weak substrate potential a lattice-gas picture describes the solid-liquid phase transition [2]. For sufficiently fine substrate corrugation, the commensurate solid undergoes a transition to a floating solid phase which then melts through dislocation unbinding. In this case the disclination unbinding transition is also washed out. In the limit of strong corrugation potential the system of course behaves like a lattice gas [11]. Even in this case Nelson and Halperin speculated that one could have a melting process similar to that for a continuum model if the corrugation mesh size was sufficiently small. Thus one expects to see very different melting behaviour depending on the strength

and the periodicity of the corrugation potential. If on the other hand the melting transition is determined by the grain boundary condensation [7] one would like to know the effects of the corrugation on the grain boundary formation and hence on the transition.

Physical systems such as physisorbed rare gas atoms on graphite [6, 12, 13],  $H_2(D_2)$  on graphite [14], and graphite intercalation compounds [15] fall in the weak to intermediate corrugation strength limit. In these systems the wavelength of the corrugation potential, a, is typically  $r(\sqrt{3} \le r \le \sqrt{7})$  times smaller compared to the systems periodicity  $(\Lambda_0)$  in the absence of corrugation. We do not know of any real physical system where  $a \gg \Lambda_0$ . Thus to understand the full scope of melting on a corrugated surface for different corrugation strengths and different substrate periodicities it is necessary to undertake a systematic simulation study of the melting phenomena for systems with different densities and different strengths of the corrugation.

Recently, Vives and Lindgard [16] have carried out extensive Monte Carlo simulations on a commensurate  $(\sqrt{3} \times \sqrt{3})$  Lennard-Jones (LJ) system to study the nature of the transition and the decay of translational and bond orientational correlations as a function of the strength of corrugation. They have also extended these calculations to the incommensurate case appropriate for the  $H_2(D_2)$ /graphite system [17] although the major emphasis in this work was to understand the low temperature structure. Earlier, Abrahams and his collaborators carried out extensive simulation studies of the rare gas atoms physisorbed on graphite [9]. These simulation studies were on LJ systems. In this chapter, we use Molecular Dynamics (MD) simulations to study the role of incommensurate corrugation potential for a 2D system of atoms interacting via a repulsive Yukawa potential, a realistic representation of intercala-

tion compounds where the intercalants are charged objects. It should be noted here that screened Coulomb systems, such as the one addressed here, take significantly more computation time (due to the exponential form of the interaction) compared to the LJ and other (algebraic) "short range" systems. Although we expect some general characteristics of Lennard-Jones and repulsive Yukawa systems to be similar, it is of interest to compare the detailed structure and the nature of the transition in these two potential systems [18].

The arrangement of the chapter is as follows. In Sec. 5.2 we introduce three different systems. The temperature dependence of different physical quantities are studied for these systems in Sec. 5.3. Finally, in Sec. 5.4 we summarize the important results of the present work and discuss its implications vis-a-vis earlier work on LJ and related systems.

### 5.2 Physical Systems

Details of potential of the system and MD simulations were discussed in chapter 4. Here, we introduce three systems which will be studied for 2D melting. MD simulations have been performed with 216 Rb ions distributed to ensure a planar density of 12 Carbons/Rb (corresponding to the stage-2  $RbC_{24}$  system), i.e., 0.0318 Rb ions/ $A^2$ . We call this system as system II. Starting from this system, we construct two other systems. System I (2K = 0 in Eq. (4.1)) has the same density as system II but without any corrugation potential. By Comparing results of the systems I and II, we can study the effects of corrugation on various physical properties. The ground state structure of the system I is an equilateral triangular structure. In addition to these two systems, we have also studied a 301-particle system (system III) with a slightly smaller Rb density (0.0311 Rb ions/ $A^2$ ) which corresponds to

the stage-2  $RbC_{24.57}$  stoichiometry. The ground state of the system III turns out to be a perfectly ordered periodic domain wall (PDW) structure [19] where hexagonal placquettes consisting of 7 Rb ions (nano domains) are periodically arranged, separated by a periodic array of domain walls (see Figure 4.3(b)). The ground state of III is commensurate whereas that of II is incommensurate. Note however that even in the commensurate case, only the atoms at the center of the  $\sqrt{7} \times \sqrt{7}$  domains sit at the minima of the single particle potential and the other atoms are displaced from these minima, but very slightly [20]. Various types of PDW structures were extensively discussed in chapter 4. The ground state of  $RbC_{24}$  (system II) can be described by the above PDW structure with additional (about 2.2% more) Rb ions occupying interstitial sites (see Figure 4.3(a)). We will refer to these additional Rb atoms as atomic (distinct from topological) defects. The effect of these atomic defects on physical properties, particularly low energy excitations will be discussed in chapter 7. The reason for choosing these two systems with close densities is to see whether the melting process and related thermodynamic quantities are sensitive to the atomic defects.

#### 5.3 Thermodynamic Properties

We discuss the melting of the systems II and III and compare their melting process with that of a corrugation free system (system I), the usual triangular solid. Temperature dependence of energy, bond orientational order parameter, its angular susceptibility, topological defects, and translational diffusion constant will be studied to monitor melting of these three systems.

#### 5.3.1 Energy vs. Temperature

In Figure 5.1, we give the temperature dependence of the potential energy (total energy- $k_BT$ ) per particle as a function of T both for the heating and the cooling runs. In the absence of the corrugation potential (2K = 0), there is a rapid change in this energy in the temperature range 195K < T < 200K. The transition is most likely first order as seen in previous MD simulation of other physical systems (LJ systems [9, 21],  $1/r^n$  systems [22] and  $e^{-\Gamma r}/r$  system [23], Weeks-Chandler-Anderson (WCA) system [24] which is a truncated version of the LJ system). The absence of hysteresis might be due to either the small size of our systems or weak first order nature of the transition. We note here that the earlier MD simulation studies of a repulsive screened Coulomb were carried out for smaller (100 particles) systems in the absence of corrugation and showed hysteresis effects [23]. The details of the equilibration time at different temperatures in this study are not available but it is possible that the observation of hysteresis might be the result of nonequilibrium effects.

If we assume that the system I shows a first order transition and take the slopes of the energy vs T above 210K and below 190K, then we find the change in entropy associated with this first order transition to be  $\Delta S/k_B=0.23$  which agrees rather well with the earlier simulation results on other systems. As seen in Figure 5.1, the effect of corrugation is drastic; in contrast to the corrugation-free case (system I), the potential energy changes smoothly for both systems II and III in the temperature range 190K < T < 230K, although there is some indication of a slope change near 220K. To make sure whether there is actually a solid-liquid phase transition in systems II and III, we must calculate other physical quantities which are sensitive to this transition. In addition, one must increase the strength of the corrugation

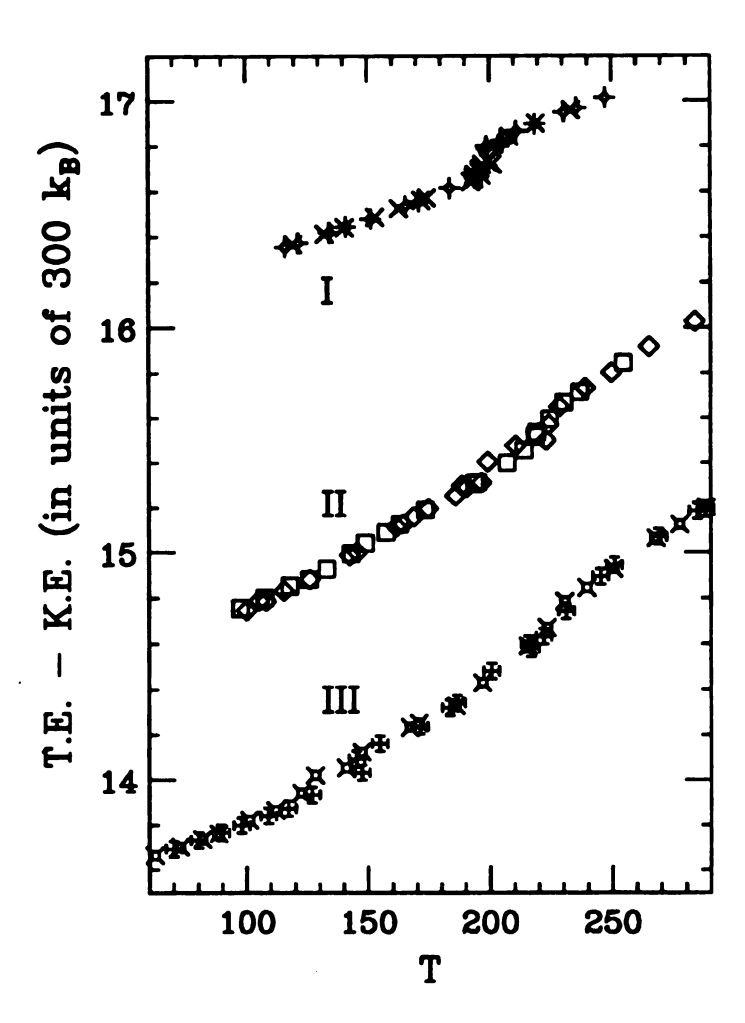


Figure 5.1: Potential energy vs. temperature with and without corrugation potential. Energy is measured in units of  $300k_B$  and the temperature in units of Kelvin. System I corresponds to  $RbC_{24}$  without corrugation (2K=0), system II corresponds to  $RbC_{24}$  with corrugation (2K=0.9), and system III corresponds to  $RbC_{24.57}$  with corrugation (2K=0.9). 2K is a measure of the strength of the corrugation potential (see Eq. (4.1)). For all these three systems both cooling and heating results are shown.

systematically to see how the corrugation alters the nature of the melting transition.

### 5.3.2 Bond Orientational Order Parameter

Since it is difficult to investigate the melting transition by calculating the positional correlation function for small systems, one usually monitors the temperature dependence of the bond orientational order parameter (BOOP) and its associated susceptibility. Strandburg, Zollweg and Chester [25] introduced the BOOP by defining a quantity  $\psi_6$  as

$$\psi_6 = \frac{1}{N} \left| \sum_{lj} \frac{e^{i6\theta_{lj}}}{n_l} \right|,\tag{5.1}$$

where the sum on l is over all the N particles, and the sum on j is over the nearest neighbours of a particular particle l,  $n_l$  being the number of such nearest neighbours defined by the standard Voronoi construction. The angle  $\theta_{lj}$  is the orientation of the bond joining the particles l and j measured with respect to a given fixed axis.

In Figure 5.2 we plot  $\psi_6$  as a function of T for systems I and II. In the corrugation-free case there is a rapid decrease in the order parameter between 190K and 200K whereas in the presence of corrugation the change in the order parameter appears to be less abrupt and the transition temperature is somewhere between 210K and 230K. In addition, the order parameter in the solid phase is larger in the corrugation-free case. This can be easily understood by recalling the ground state structure of these systems. The system without corrugation has a perfect triangular lattice structure at T=0K for which  $\psi_6$ =1 whereas in the system with corrugation the domain walls reduce the strength of this order parameter. The nonzero value of the order parameter in the liquid phase of system I is due to finite-size and periodic boundary condition because  $\psi_6$  should vanish in the thermodynamic limit. In the presence of the corrugation potential of hexagonal symmetry  $\psi_6$  should be nonzero even in

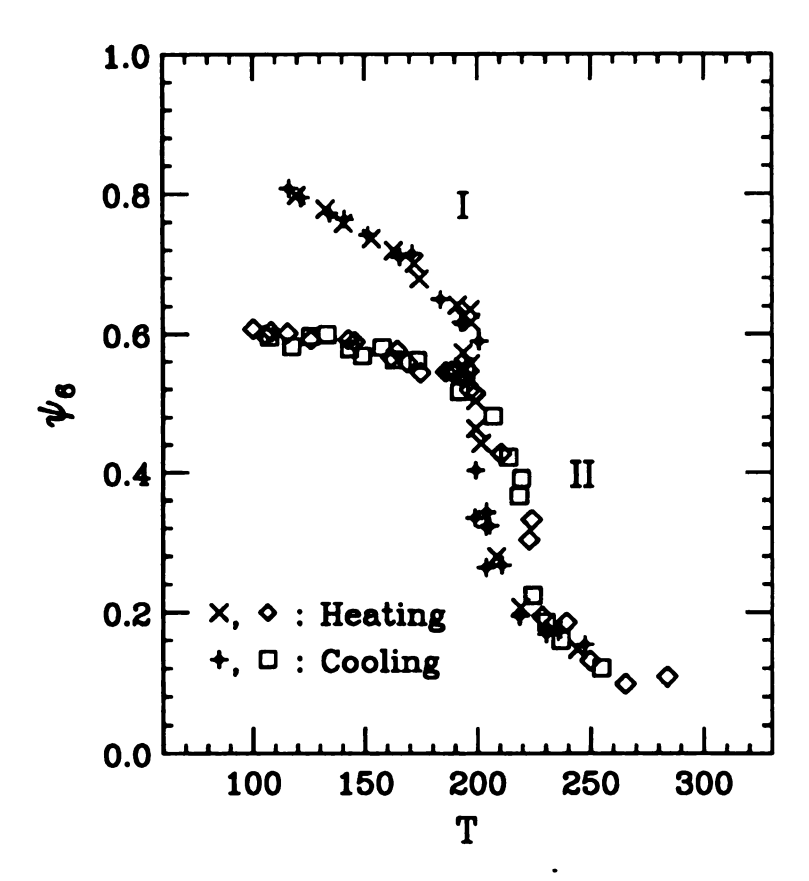


Figure 5.2: The bond orientational order parameter  $\psi_6$  as a function of temperature for systems I and II (see Figure 5.1 captions for explanations). Both heating and cooling run results are shown.

the thermodynamic limit. We however note that in our finite system simulations (with periodic boundary conditions), for temperature above 240K the residual order parameter is independent of the strength of the corrugation suggesting that the influence of finite size effects in the calculation of  $\psi_6$  is large.

### 5.3.3 Angular Susceptibility

To further probe the nature of the transition and to obtain the transition temperature more accurately we have calculated the susceptibility associated with the BOOP. We define the angular susceptibility  $\chi_6$  as

$$\chi_6 = N[\langle |\psi_6|^2 \rangle - \langle |\psi_6| \rangle^2]/k_B T. \tag{5.2}$$

In Figure 5.3, we give the temperature dependence of  $\chi_6$  for the two systems discussed in the previous paragraph. In the corrugation-free system, the susceptibility increases rapidly with decreasing T and shows a dramatic (almost discontinuous) drop between 200K and 195K. This is the same temperature range where the order parameter shows a rapid change (Figure 5.2) thereby suggesting that the transition is most likely first order. From our finite size simulation we cannot conclusively state that the transition is indeed first order. In the absence of an observable hysteresis we cannot rule out a sharp but continuous transition. Glasser and Clark [24] in their extensive MD simulation studies of a truncated LJ system found a nearly discontinuous drop in  $\chi_6$  as a function of increasing density (temperature being held constant) indicating a first order transition. They however did not discuss the hysteresis issue.

In the presence of corrugation the behaviour of the susceptibility is much more intriguing. For the  $RbC_{24}$  system (system II),  $\chi_6$  is relatively small and is a smooth function of temperature showing a very broad peak near 230-240K. There is not

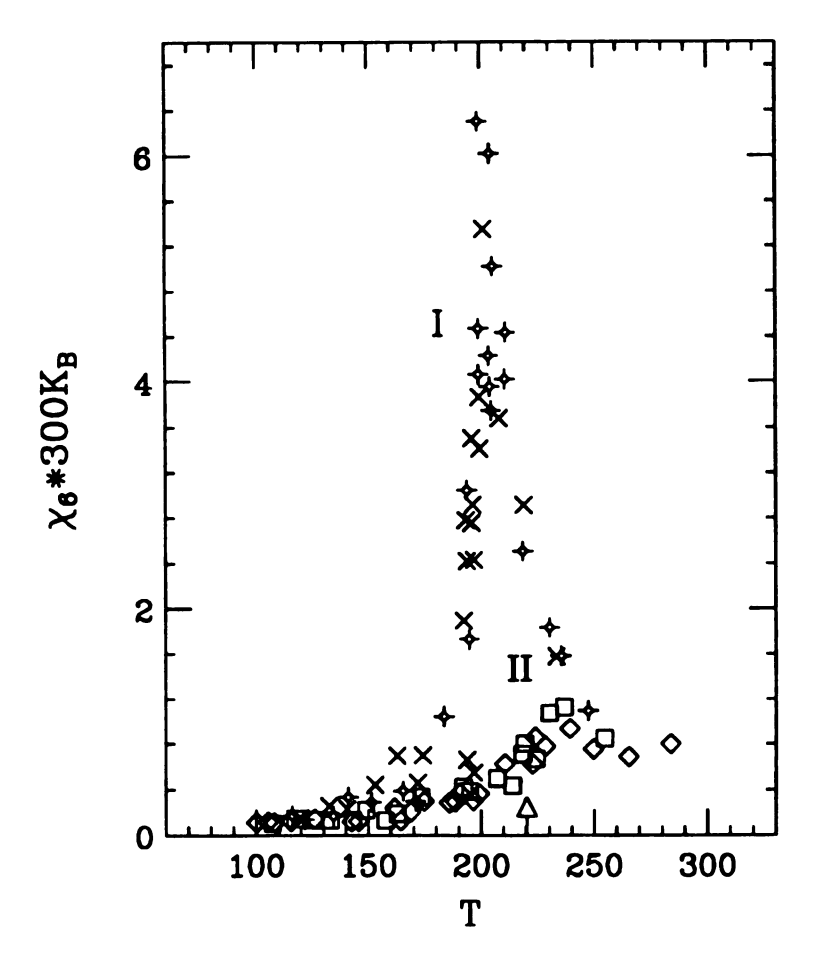


Figure 5.3: The angular susceptibility  $\chi_6$  (see Eq. 5.2 for the definition) vs. temperature for systems I and II (see Figure 5.1 captions for explanation). Heating and cooling run results are shown.

much action near the temperature where the order parameter shows a rapid drop at 200K < T < 220K (indicated by an arrow). Clearly the melting transition of this domain wall solid is very different from that of a simple triangular solid (system I). In order to pin down the precise nature of the transition it will be necessary to carry out extensive Monte Carlo simulations in larger systems covering the transition region and also the region where the susceptibility shows a peak.

One plausible physical argument we can give to explain the temperature dependence of  $\psi_6$  and  $\chi_6$  in the domain wall solid case is the following [26]. As we increase the temperature, the region near the domain walls starts to soften or 'melt' (~ 200K); this leads to a rapid decrease in the long range bond orientational order. However above this transition there is still sufficient short range orientational correlation inside each triangular domain and the peak in  $\chi_6$  can be thought of as a second 'melting' of these highly correlated small triangular lattice clusters of  $\sqrt{7} \times \sqrt{7}$  domains, the transition region being broadened by finite size effects. The fact that this broad peak is seen at temperature  $\sim 240 ext{K}$  which is higher than  $200 ext{K}$ where the corrugation-free  $\sqrt{6} \times \sqrt{6}$  triangular solid melts can be understood by the following simple argument. Ordinarily a  $\sqrt{7} \times \sqrt{7}$  triangular solid in the absence of corrugation will melt at a temperature lower than 200K because of lower energy compared to the  $\sqrt{6} \times \sqrt{6}$  case whose melting temperature is about 200K. However in the presence of a strong corrugation potential the melting temperature will be increased from this value and it is possible that the melting temperature is near 240K where one sees the broad peak in  $\chi_6$ . In fact, Vives and Lindgard [16] in their MC simulation study of a commensurate LJ system found an increase in the melting transition temperature with an increase in the strength of the corrugation.

Since the ground state of RbC24 can be described by a perfectly ordered PDW solid with a few additional Rb atoms (defects) and since it is reasonable to expect that the order parameter, the susceptibility and the nature of the transition might be affected by these defects, we have studied the temperature dependence of  $\psi_6$  and  $\chi_6$  for the stage-2  $RbC_{24.57}$  (system III) whose ground state structure is shown in Figure 4.3(b). In fact, one can study the melting properties of a whole class of PDW solids where the widths of the domains and domain walls can be systematically varied by simply changing the planar Rb concentration [19]. This can in principle tell us how the nature of the melting transition changes as we introduce domain walls into the system. For  $RbC_{24.57}$  where the  $\sqrt{7} \times \sqrt{7}$  triangular domains contain 7 atoms separated by  $2 \times 3 \times \sqrt{7}$  walls, the order parameter at low temperatures is slightly larger than RbC24 [see Figure 5.4(a)] consistent with the presence of additional defect atoms in the latter system. For the former we see a phase transition (rapid decrease of  $\psi_6$ ) near T=230K [Figure 5.4(a)] with a peak in the susceptibility  $\chi_6$ [see Figure 5.4(b)] at a higher temperature ( $T \sim 240$ K). This is qualitatively similar to that shown by the system II. Thus we conclude that the peak in orientational susceptibility above the melting transition temperature appears to be a general property of the melting of domain wall solids. The removal of defects makes the susceptibility peak in the system III slightly more pronounced compared to the system II. But in both cases the peak intensity is about 3-5 times smaller than the corrugation free case.

### 5.3.4 Topological Defects

To further explore the effect of corrugation on melting we have studied the temperature dependence of the concentration of local topological defects (LTDs) which are bound pairs and quartets of 5- and 7-fold coordinated atoms both in the pres-

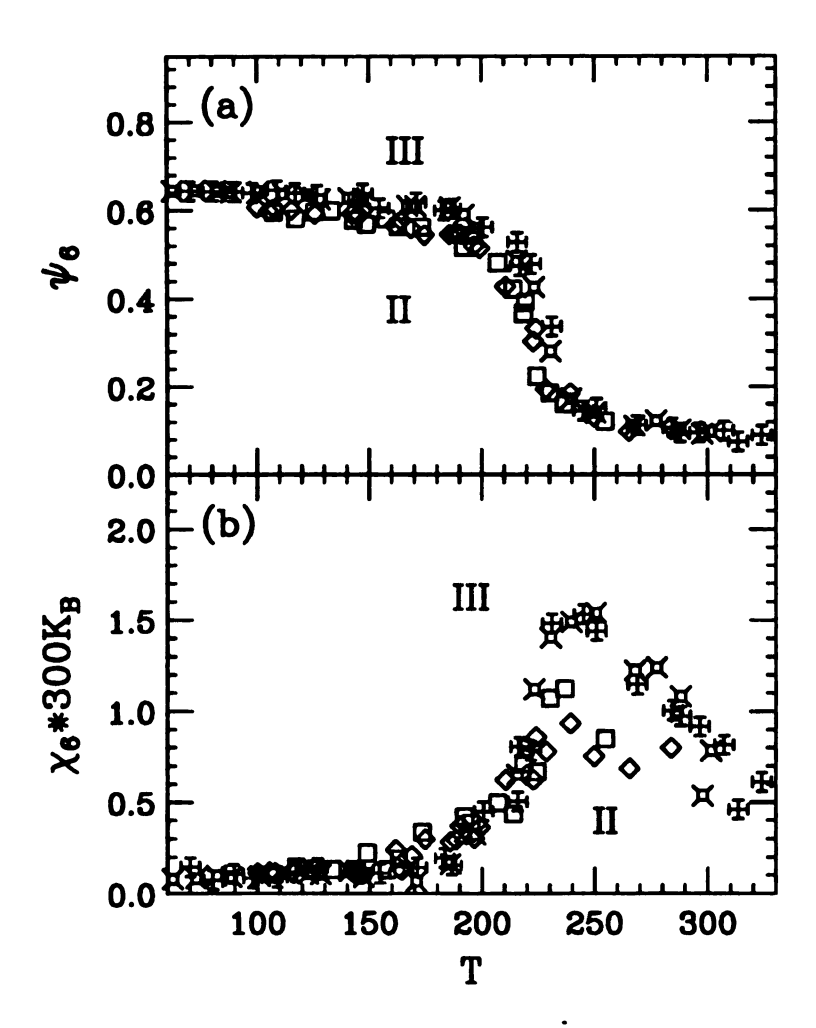


Figure 5.4: Temperature dependence of (a) bond orientational order parameter  $\psi_6$  for systems II and III and (b) corresponding angular susceptibility  $\chi_6$ . See Figure 5.1 captions for the description of different systems. Both heating and cooling runs are shown.

ence and the absence of corrugation (see Figure 5.5). We use the standard Voronoi polyhedra construction to obtain the number of 5, 6, and 7 fold coordinated atoms. It appears that the effect of corrugation on the density of these LTDs is marginal excepting in the transition region. In the transition region, the temperature dependence of the LTD density  $\rho_D$  is smoother for the corrugation case (see Figure 5.6) indicating a continuous transition. One interesting observation is that in the solid phase (T < 195K) and in the liquid phase (T > 250K)  $\rho_D$  is weakly dependent on the corrugation strength (2K). The corrugation potential has a strong effect on the defect density only in the transition region. When 2K=0, we see that the rate of increase of  $\rho_D$  with temperature,  $d\rho_D/dT$ , is maximum at T=200K which is also the maximum of  $\chi_6$ . In contrast, for 2K=0.9 i.e. for the system II,  $d\rho_D/dT$  is maximum near T=220K whereas  $\chi_6$  peaks at  $T \sim 240\text{K}$ , again indicating a basic difference between the melting characteristics of a triangular solid in the absence of corrugation and those of a domain wall solid in the presence of corrugation.

### 5.3.5 Translational Diffusion Constants

Finally, the translational diffusion constant D using the relation  $\langle r^2 \rangle = 4Dt$  has been calculated to monitor the solid-liquid transition and the effect of the corrugation on the diffusion rate. In contrast to its effect on the density of topological defects, corrugation profoundly affects the diffusion rate (see Figure 5.7). The nearly first order nature of the transition in the corrugation free case is seen as a dramatic increase in D at about 200K. On the other hand, in the presence of corrugation D starts to increase rather slowly near the transition temperature (T=220K), seems to flatten slightly near 240K where there is a peak in the orientational susceptibility, and finally increases linearly with T. The drastic reduction in D in the liquid phase in the presence of corrugation can be understood in terms of an additional

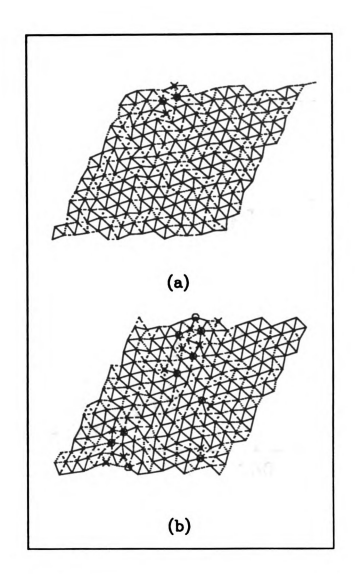


Figure 5.5: Topological defects (5- and 7-fold coordinated atoms) (a) in a solid and (b) a liquid state obtained by using Voronoi polyhedra construction.

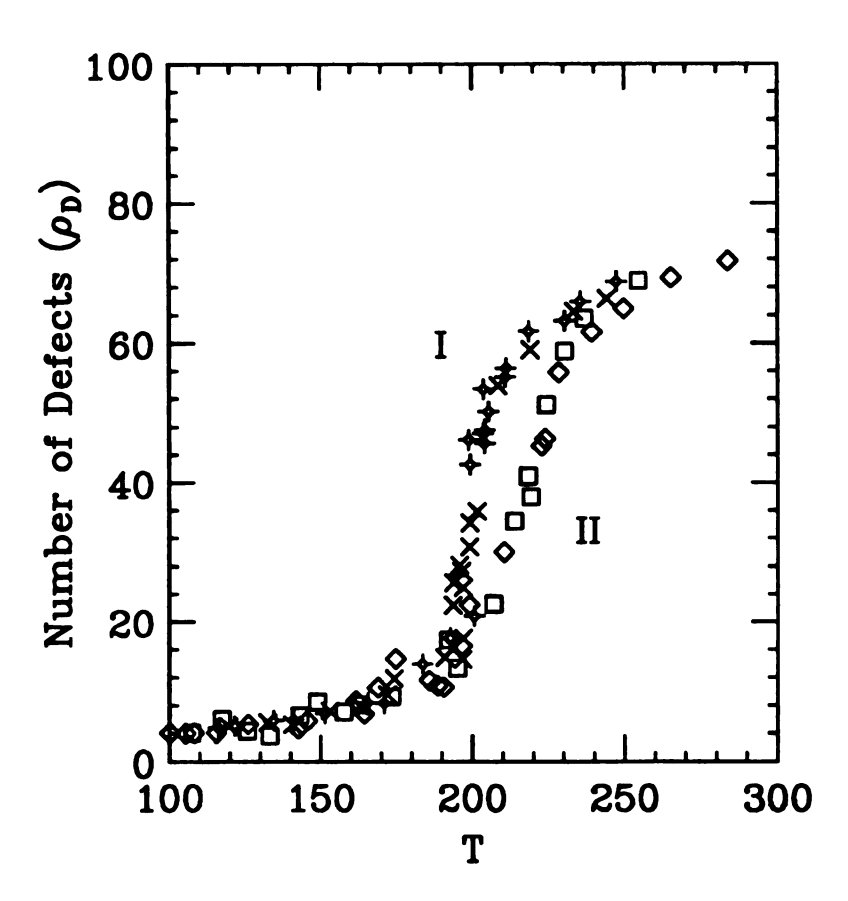


Figure 5.6: The number of disclinations (topological defects, 5- and 7-fold coordinated atoms) vs. temperature. Observe the sharp increase in the number of disclinations near 200K for system I (without corrugation) and smooth increase near 220K for the system II (with corrugation). Different symbols refer to heating and cooling runs.

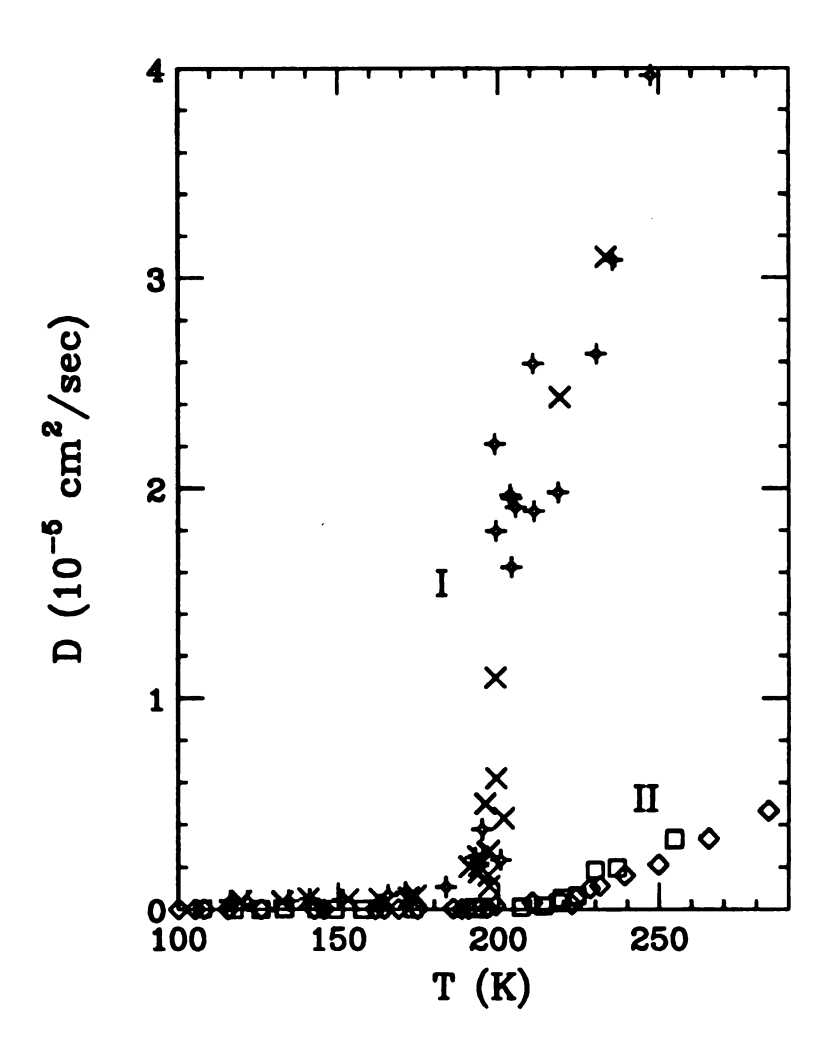


Figure 5.7: Diffusion constant D vs. temperature for system I (without corrugation) and system II (with corrugation). Both heating and cooling runs are shown.

activation process involving the corrugation potential. Using the parameters of our potential we estimate the energy barrier associated with the corrugation potential to be 1080K. The experimental value of the activation energy obtained from the diffusion measurements is  $\sim 0.063$  eV (756K) which is about a factor 2/3 of the single particle activation barrier. The net activation energy is of course a combination of the single particle and interaction potential. More detailed temperature dependent study of the diffusion rate D in the liquid phase is required to quantitatively determine the true activation energy. Further details of the diffusion and the nature of the dynamics will be discussed in chapter 6.

# 5.4 Summary and Discussion

In summary, we have carried out extensive MD simulations of the melting and freezing transitions of a 2D repulsive Yukawa system in the presence of (strong) incommensurate corrugation potential. This model describes rather well the physical properties of stage n ( $n \ge 2$ ) graphite intercalation compounds and similar systems where the intercalants are charged objects interacting with a screened Coulomb potential. The parameters we have chosen are appropriate for stage-2 Rb GIC. Before comparing our simulation results with experiments in stage-2 Rb GIC we summarize some of our general observations.

The triangular lattice structure of the corrugation-free solid changes to a periodic domain wall structure in the presence of a (strong) incommensurate corrugation potential. The size of the domains and domain walls depend on the strength of the corrugation potential and the intercalant density. Whereas the former (triangular solid) undergoes a sharp (perhaps discontinuous) melting/freezing transition, the latter (PDW solid) shows a smooth transition. The transition temperature increases

in the presence of corrugation. Such an observation was also made by Vives and Lindgard [16] in their Monte Carlo study of the melting of  $\sqrt{3} \times \sqrt{3}$  commensurate LJ systems. In the absence of corrugation, we find that the rapid decrease in the bond orientational order parameter  $\psi_6$  and the peak in the corresponding susceptibility  $\chi_6$  occur at the same temperature. In contrast, in the presence of the corrugation potential,  $\chi_6$  does not show any structure (discontinuity or peak) at the temperature where  $\psi_6$  shows a rapid decrease, but has a rather broad weak peak several degrees above this temperature. We have given a physical explanation of this behaviour in terms of the melting of a domain wall solid.

The temperature dependence of  $\chi_6$  for the corrugation-free system shows a sharp  $\lambda$ -like peak. The ratio of the half width  $\Delta T$  to the transition temperature T i.e.  $\Delta T/T=0.1$ . Recently Glasser and Clark [24] have carried out extensive MD simulations on a truncated LJ system (WCA system) and have studied the melting transition at a constant T but as a function of density  $(\rho)$ . They also find a sharp change (actually a discontinuity) in  $\chi_6$  near the melting transition indicating a discontinuous transition, very much like what we have seen as a function of temperature at constant density. The half width of their peak in  $\chi_6$  vs  $\rho$ ,  $\Delta \rho/\rho_c=0.22$ . In contrast to our MD results, the MC results (for LJ systems) of Vives and Lindgard [16] in larger systems (N=2700) show an extremely broad peak in  $\chi_6$  and appreciable hysteresis, most likely due to nonequilibrium effects. Although our system size is small, our results are for well equilibrated systems as indicated by near agreement of the heating and cooling runs. Because of the above difficulties we are unable to compare the sharpness of the susceptibility peak (as a function of temperature) in the corrugation free limit for repulsive Yukawa and LJ systems.

Finally we would like to compare our simulation results with available experi-

ments. It is not possible to directly measure the bond orientational order parameter and the associated susceptibility. The former can be indirectly measured from the anisotropy of the X-ray (or neutron) diffraction peaks in the "solid phase". Zabel and coworkers [27, 28] measured the intensity of the superlattice peak as a function of temperature using neutron diffraction. They find a continuous transition from the solid to the liquid phase at about 165K in stage-2  $RbC_{24}$ . Our simulation results agree with this except that our transition temperature is about 220K. This is due to (1) finite size effect and (2) limitations in the potential model that we have used. In fact, Moss and coworkers [29, 30] have used a different 2-body potential (but the same 1-body potential as used here) and find the transition temperature to be somewhere near 160K. However they did not carry out a careful T-dependent study of different physical quantities as we have done here. By comparing the two different 2-body potentials in the region of physical interest we find that the Moss et al.'s potential is slightly weaker than ours. This might explain the difference in the transition temperature discussed above.

# **Bibliography**

- J. M. Kosterlitz and D. J. Thouless, Progress in Low Temperature Physics, Vol. VII-B, ed. by D. F. Brewer (North-Holland, Amsterdam), p.373.
- [2] D. R. Nelson and B. I. Halperin, Phys. Rev. B 19, 2457 (1979).
- [3] A. P. Young, Phys. Rev. B 19, 1855 (1979).
- [4] K. J. Strandburg, Rev. Mod. Phys. 60, 161 (1988).
- [5] R. J. Birgenau and P. M. Horn, Science 232, 329 (1986), N. Grieser et. al., Phys. Rev. Lett. 59, 1706 (1987).
- [6] Q.M. Zhang and J. Z. Larese, Phys. Rev. B 43, 938 (1991).
- [7] S. T. Chui, Phys. Rev. Lett. 48, 933 (1982).
- [8] W. A. Steele (Private communication).
- [9] F. F. Abraham, Adv. Phys. 35, 1 (1986); F. F. Abraham, Phys. Rev. B 28, 7338(1983); ibid B 29, 2824 (1984).
- [10] A.D. Novaco and J.P. McTague, Phys. Rev. Lett. 38, 1286 (1977).
- [11] L. K. Runnels, Phase Transitions and Critical Phenomena, ed. by C. Domb and M. S. Green, (Academic Press, New York, 1972), Vol 2, p.305.

- [12] M. J. Colella and R. M. Suter, Phys. Rev. B 34, 2052 (1986).
- [13] K. L. D'Amico, J. Bohr, D. E. Moncton, and D. Gibbs, Phys. Rev. B 41, 4368 (1990).
- [14] J. Cui and S. C. Fain, Jr., Phys. Rev. B 39, 8628 (1989).
- [15] S. C. Moss and R. Moret, Graphite Intercalation Compounds, Vol 1, Structure and Dynamics, ed. by H. Zabel and S. A. Solin, (Springer Series on Topics in Current Physics, Springer (1990).
- [16] E. Vives and Per-Anker Lindgard, Phys. Rev. B 44, 1318 (1991).
- [17] E. Vives and Per-Anker Lindgard, (private communication).
- [18] Recently structural phase transition (from BCC to FCC) and melting transition for a 3-dimensional repulsive Yukawa system has been studied extensively by M.
  O. Robbins, K. Kremer, and G. S. Grest, Jour. Chem. Phys. 88, 3286 (1988).
- [19] Hyangsuk Seong, S. Sen, T. Cagin, and S. D. Mahanti, Phys. Rev. B 45, 8841 (1992).
- [20] The structure of the PDW solid is quite similar to the one proposed by J. Cui and S. C. Fain, Jr. (see Ref. [14]) for the  $\lambda$ -phase of  $D_2$ /graphite where  $\sqrt{3} \times \sqrt{3}$  domains and  $\sqrt{3} \times 1$  walls are periodically arranged. One should also note that all the  $D_2$  molecules do not sit at the hexagon centers as in the PDW model (see Ref. [17]).
- [21] C. Udink and J. van der Elsken, Phys. Rev. B 35, 279 (1987).
- [22] P. Vashishta and R. K. Kalia, Melting, Localization, and Chaos, ed. by. R. K. Kalia and P. Vashishta, North Holland (New York) 1982, p.43.

- [23] H. Chen, P. Dutta, D. E. Ellis, and R. Kalia, Jour. Chem. Phys. 85(4), 2232 (1986).
- [24] M. Glasser, Ph. D thesis, University of Colorado (1991).
- [25] K. J. Strandburg, J. A. Zollweg. and G. V. Chester, Phys. Rev. B 30, 2755 (1984).
- [26] There is an alternate way of looking at the melting transition (suggested to us by Prof. S. Jayaprakash of Ohio State University) i.e. in terms of condensation of defects which are in this case domain walls. One can visualize preexisting elemental √7 × √7 triangular placquettes in the liquid phase above the solid-liquid transition. The region between these placquettes (domain walls) can be thought of as defects which then order below a critical temperature. For the system size we have studied, the number of these defects is small (by about a factor of 7) compared to the number of atoms and therefore one sees a rather broad transition region. To test this interesting idea one has to study the melting of the PDW solid for larger systems and see if the transition region sharpens with the size of the system.
- [27] H. Zabel, A. Magerl, J. J. Rush, and M. E. Misenheimer, Phys. Rev. B 40, 7616 (1989).
- [28] J. D. Fan, George Reiter, and S. C. Moss, Phys. Rev. Lett. 64, 188 (1990).
- [29] S. C. Moss, et al., Phys. Rev. Lett. 57, 3191 (1986).
- [30] J. D. Fan, Omar A. Karim, G. Reiter, and S. C. Moss, Phys. Rev. B 39, 6111 (1989).

# Chapter 6

# Dynamics of 2D Repulsive Screened Coulomb Fluids on a Corrugated Surface

### 6.1 Introduction

Excepting for a short discussion on the diffusion constant, we have been until now concerned with equilibrium (static) properties of 2D systems. Next two chapters will focus on the question of dynamics. Dynamics of homogeneous fluids in three dimension is well understood [1]-[3]. In recent years there has been considerable interest in understanding the dynamic (and thermodynamic) properties of fluids subjected to different types of external constraints [4]-[11]. Examples of such systems are: two dimensional fluids in the presence of external corrugation potential as in intercalation compounds [6]-[9], premelted surface fluid phase [10], and fluids in porous media [11]. One expects the particles in the fluid phase to exhibit different types of dynamic behavior in different length and time scales due to the inhomogeneous nature of these external constraints. An extreme example is the solid-like dead layer formed near the constraining walls when a fluid flows through a mesoporous medium. Here one expects to see the coexistence of solid-like and fluid-like

dynamics.

Dynamic properties of physical systems can be studied by time correlation functions and their Fourier transforms which can be directly obtained from neutron or light scattering experiments. In neutron scattering experiments thermal neutrons are directed onto the fluid with an incident wave vector  $\mathbf{k}_i$  and energy  $E_i$  and the scattered neutrons are measured as a function of the wave vector  $\mathbf{k}_f$  and energy  $E_f$ . One measures the scattering cross section ( $\sigma$ ) as a function of  $\mathbf{q} = \mathbf{k}_f - \mathbf{k}_i$  and  $h\nu = E_f - E_i$ . The cross section directly relates to the dynamic structure factor  $S(\mathbf{q}, \nu)$  [1, 7]. Even if the fluid is in a state of macroscopic equilibrium, spontaneous microscopic fluctuations in the local density occur in the system due to thermal excitations, and these fluctuations give rise to the above dynamic scattering. Usually in thermal neutron scattering [12] from fluids, density fluctuations in space and time lead to characteristic  $\mathbf{q}$  and  $\nu$  dependence of  $S(\mathbf{q}, \nu)$ .

In this chapter we address the dynamics of a specific class of layered systems, namely 2D fluids subjected to a periodic corrugation potential whose strength can be tuned. Physical realizations of such systems whose dynamics has been extensively probed experimentally are graphite intercalation compounds (GICs) [6]. Zabel and coworkers [7, 8] have carried out neutron scattering experiments in alkali metal GICs for which the substrate corrugation potential produced by the graphite layer on the alkali intercalants is strong. However, to study the evolution of the dynamics from a homogeneous fluid to a lattice-fluid, we change the strength of the periodic corrugation potential from 2K = 0 to 2K = 0.9 (see Eq. (4.1) of chapter 4 for definition of 2K) through intermediate values, 0.15, 0.36, 0.55, and 0.75, the value of 0.9 appropriate for stage-2 Rb GIC. See chapter 4 for the the details of potentials and Molecular Dynamics (MD) simulations. Here we study larger systems with 864

particles and concentrate on the properties of the liquid state obtained by averaging over the directions of the scattering wave vector in the calculation of correlation functions.

To understand the dynamics of fluid systems in detail, we study different correlation functions such as van Hove correlation function, velocity auto-correlation function, intermediate scattering function, and dynamic structure factor. These will be defined in the following sections and we will discuss how these functions are affected by changing the strength of the corrugation potential (i.e. in going from a simple homogeneous liquid to a GIC system).

## 6.2 Time Correlation Functions in Real Space

An equilibrium density-density time correlation function was first introduced by van Hove [13] to discuss the density fluctuation in a liquid. It is given by

$$G(\mathbf{r},t) = \frac{1}{N} \langle \sum_{i=1}^{N} \sum_{j=1}^{N} \delta(\mathbf{r} + \mathbf{r}_{j}(0) - \mathbf{r}_{i}(t)) \rangle, \tag{6.1}$$

where  $\mathbf{r}_i(t)$  is the position of the *i*-th particle at time t and the angular brackets imply time average. Physically,  $G(\mathbf{r},t)d\mathbf{r}$  is proportional to the probability of finding a particle i in a region  $d\mathbf{r}$  around a point  $\mathbf{r}$  at a given time t that there was a particle j at the origin at time t = 0. The function  $G(\mathbf{r},t)$  can be separated into two terms, usually called the "self"(s) and "distinct"(d) parts, i.e.

$$G(\mathbf{r},t) = G_s(\mathbf{r},t) + G_d(\mathbf{r},t), \tag{6.2}$$

where

$$G_s(\mathbf{r},t) = \frac{1}{N} \langle \sum_{i=1}^N \delta(\mathbf{r} + \mathbf{r}_i(0) - \mathbf{r}_i(t)) \rangle, \qquad (6.3)$$

$$G_d(\mathbf{r},t) = \frac{1}{N} \langle \sum_{i \neq j}^N \delta(\mathbf{r} + \mathbf{r}_j(0) - \mathbf{r}_i(t)) \rangle. \tag{6.4}$$

From the above equation we find that  $G_s(\mathbf{r},0) = \delta(\mathbf{r})$  and  $G_d(\mathbf{r},0) = \rho g(\mathbf{r})$ , where  $g(\mathbf{r})$  is a pair distribution function which gives the probability of finding a pair of atoms a distance  $\mathbf{r}$  apart. For isotropic fluids, both  $G_s$  and  $G_d$  are functions of the scalar quantity  $\mathbf{r}$ .

### 6.2.1 $G_s(\mathbf{r},t)$ for Typical Systems

Before discussing the space and time dependence of  $G_s(\mathbf{r},t)$  for a corrugated fluid, let us review what is known about this quantity for simple physical systems. For an ideal gas, a diffusing atom, and a harmonic oscillator, it is found that the self part of the function is a Gaussian in r [1, 14]. Furthermore, it is rigorously true for any dynamical system as  $t \to 0$ , because the atoms behave as if they are free. Therefore, one usually assumes that the spatial dependence of  $G_s(\mathbf{r},t)$  is approximated by a Gaussian [12],

$$G_s(\mathbf{r},t) = \left(\frac{1}{2\pi\alpha(t)}\right)^{d/2} e^{-r^2/2\alpha(t)},\tag{6.5}$$

where d is the dimension of the system. The mean square displacement gives a physical meaning to  $\alpha(t)$ , i.e.,

$$\langle (\mathbf{r}(t) - \mathbf{r}(0))^2 \rangle = \int d\mathbf{r} r^2 G_s(\mathbf{r}, t) = \alpha(t) d, \tag{6.6}$$

namely  $\alpha(t)d$  is the mean square displacement after a time t for d-dimensional system [see Appendix C for the proof of Eq. (6.6)]. There are some cases for which  $\alpha(t)$  is known exactly. For free particles using  $\mathbf{r}(t) - \mathbf{r}(0) = t\mathbf{p}/m$ , one finds that

$$\alpha(t) = \frac{k_B T t^2}{m},\tag{6.7}$$

where T and p are respectively the temperature and the momentum of the free particle. For a diffusing Brownian particle of mass m

$$\alpha(t) = 2D(t - \frac{Dm}{k_B T}),\tag{6.8}$$

which is obtained easily from the equation of Brownian motion (i.e. Langevin equation), D being the diffusion constant [14]. For harmonic phonons in solids, one obtains

$$\alpha(t) = \frac{2k_BT}{m} \int_0^\infty d\omega Z(\omega) \frac{1 - \cos \omega t}{\omega^2},\tag{6.9}$$

where  $Z(\omega)$  is the normalized density of phonon states. Eq. (6.9) recovers the free particle result when we expand  $\cos wt$  in powers of small t and keep the leading term. However, at long times this does not increase continuously but approaches a finite limit. In fact, this particular feature distinguishes a solid from a liquid and a gas.

We know explicit forms of  $\alpha(t)$  for short and long times for a simple liquid. However, for intermediate times considerable deviation from a Gaussian behaviour occurs. Except for small times, the Gaussian form also does not hold for a particle diffusing in a solid where the particle stays mainly at discrete positions determined by the lattice. Egelstaff and Schofield [14] constructed a simple  $\alpha(t)$  for intermediate time t which recovers the correct short and long time behavior for a liquid. The expression for  $\alpha(t)$  is given by

$$\alpha(t) = 2D[(t^2 + c^2)^{1/2} - c], \tag{6.10}$$

where c is a parameter characteristic of the model. An easy way to study the dynamics for intermediate times is through MD simulations.

### 6.2.2 Self-Diffusion Constant

A macroscopic quantity which characterizes the diffusion processes in a one-component fluid is the self-diffusion constant D. By looking at the mean square displacements of particles, one can study the diffusion process. Figure 6.1 shows trajectories of a tagged particle for various strengths of the corrugation potential but for a fixed temperature. The figure clearly shows that the motion of a particle is confined as the strength of the corrugation potential increases. In a given time interval, particles of the 2K = 0 system can diffuse much farther than those of the 2K = 0.9 system. For a 2D system, the diffusion constant D is defined as,

$$D = \lim_{t \to \infty} \frac{(\Delta \mathbf{r})^2}{4t}.$$
 (6.11)

To see how D approaches its  $t \to \infty$  limit, we have calculated a time dependent diffusion coefficient D(t)

$$D(t) = \frac{(\Delta \mathbf{r})^2}{4t}. ag{6.12}$$

Figure 6.2 shows the time dependence of the D(t) for various strengths of corrugation potential near 250K. Whereas for the 2K = 0 and 0.15 systems D(t) increases very slowly, for the rest of the systems D(t) decreases even more slowly as time goes on. These different trends might be understood by looking at the barrier height  $\Delta$  (in units of  $k_B$ ) of the corrugated potential. For T near 250K, the first two systems are at temperature higher than  $\Delta$  (0 for 2K = 0 and 180K for 2K = 0.15), whereas  $\Delta$ 's for the other systems are larger than 250K (see Table 6.1). This t-dependence of D(t) might tell us something about the anomalous behaviour of diffusion in 2D systems resulting from the long time tail of the velocity auto-correlation function [15]. To clear up this question, we need to study (1) larger size of the systems so

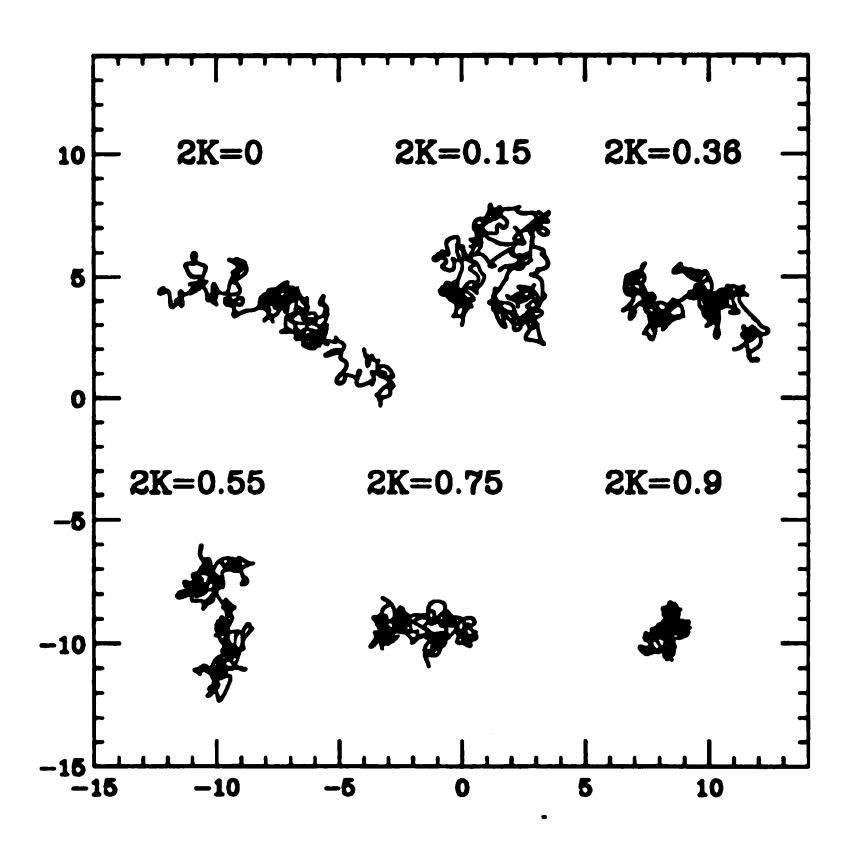


Figure 6.1: Trajectories of tagged particles during about 100ps for various 2K at a temperature near 250K.

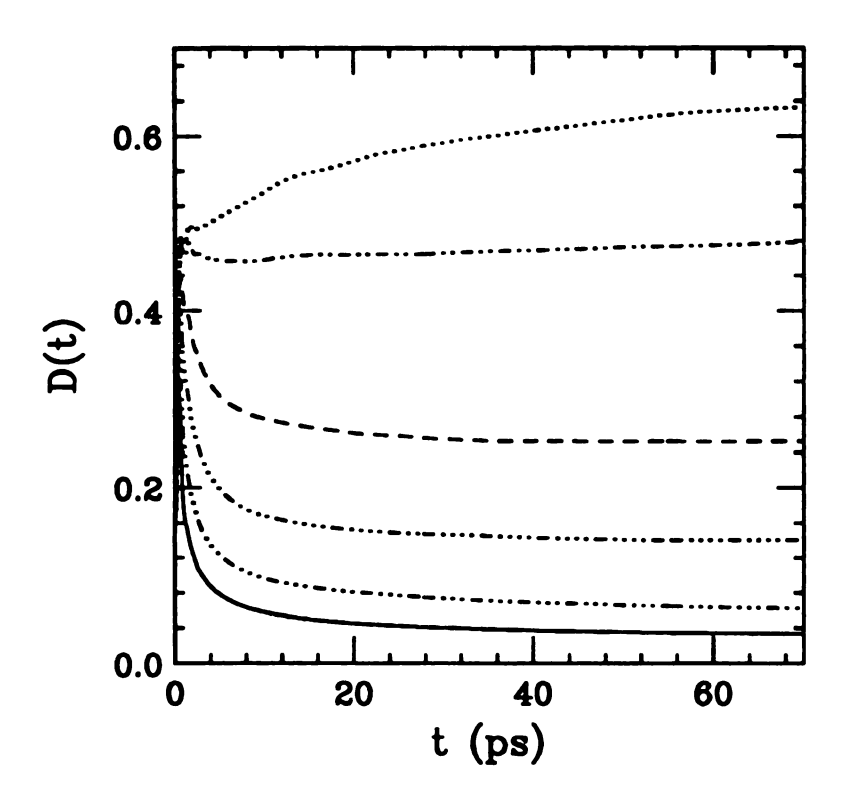


Figure 6.2: Time dependent diffusion coefficient at about 250K. From top to bottom curve, 2K = 0, 0.15, 0.36, 0.55, 0.75, and 0.9.

Table 6.1: Barrier height  $(\Delta)$  from the various corrugation potentials, the temperature (T) of corresponding systems, and the diffusion constant (D) obtained from mean square displacement (and D obtained from velocity auto-correlation function) for different 2K.

2 <i>K</i>	Δ	T (Kelvin)	$D(10^{-4}cm^2/sec)$
0	0	254	0.633 (0.616)
0.15	180	253	0.479 (0.479)
0.36	432	251	0.253 (0.254)
0.55	660	254	0.141 (0.141)
0.75	900	256	0.062 (0.070)
0.9	1080	248	0.033 (0.036)

that our  $\langle r^2 \rangle$  calculations are not affected by periodic boundary conditions and (2) carry out longer time runs to see this 'long' time behavior. However, in our present MD simulation studies, we do not approach this long time behavior.

Diffusion constant also can be obtained from the time integral of the velocity auto-correlation function (VAF). The VAF is not directly measured in scattering experiments and the most direct method of determining the VAF is actually MD simulations. It reveals molecular motions on a microscopic time scale where dynamical details occurring over intervals of  $\sim 10^{-13}$ sec in real time can be resolved. Since the interval is comparable to the molecular collision time, one is effectively probing features of dynamical behavior most sensitive to the details of the interactions.

The VAF is related to the diffusion constant as follows,

$$(\Delta \mathbf{r})^2 = 2dDt \tag{6.13}$$

$$= \int_0^t \mathbf{v}(t')dt' \cdot \int_0^t \mathbf{v}(t'')dt'' \tag{6.14}$$

$$= 2t \int_0^t ds \langle \mathbf{v}(s) \cdot \mathbf{v}(0) \rangle - 2 \int_0^t s ds \langle \mathbf{v}(s) \cdot \mathbf{v}(0) \rangle, \qquad (6.15)$$

where d in Eq. (6.13) is a dimension of the system. In the limit of large t, we get

$$D = \frac{1}{d} \lim_{t \to \infty} \int_0^t ds \langle \mathbf{v}(s) \cdot \mathbf{v}(0) \rangle. \tag{6.16}$$

The 4-th column of Table 6.1 shows diffusion constants for various strengths of the corrugation potential. The first numbers obtained from the mean square displacements agree very well with the second ones (given inside the parenthesis) obtained from the integration of the VAF. To carry out the numerical integration accurately in Eq. (6.16), each point is joined smoothly and the interpolated values are used in the integration.

In addition to the diffusion constant obtained from the time integral of the VAF, the latter's time dependence conveys a large amount of information about the dynamics of a particle in the real time domain. To understand this t-dependence, let us study the VAF in more detail. The normalized VAF is defined by

$$Z(t) = \frac{\langle \sum_{i} \mathbf{v}_{i}(t) \cdot \mathbf{v}_{i}(0) \rangle}{\langle \sum_{i} \mathbf{v}_{i}(0) \cdot \mathbf{v}_{i}(0) \rangle}.$$
(6.17)

Figure 6.3 shows the VAF for various values of 2K near 250K. As in an ordinary liquid, Z(t) shows an oscillatory t-dependence with decreasing amplitude resulting from the diffusive dynamics. The effect of corrugation at least up to  $t \sim 1$ ps is to decrease the area under the positive part and increase that under the negative part. This makes a major contribution to the overall decrease in D with increasing corrugation strength. The characteristic time dependence of Z(t) can be described broadly with three regimes, short time, intermediate time, and the long time behavior.

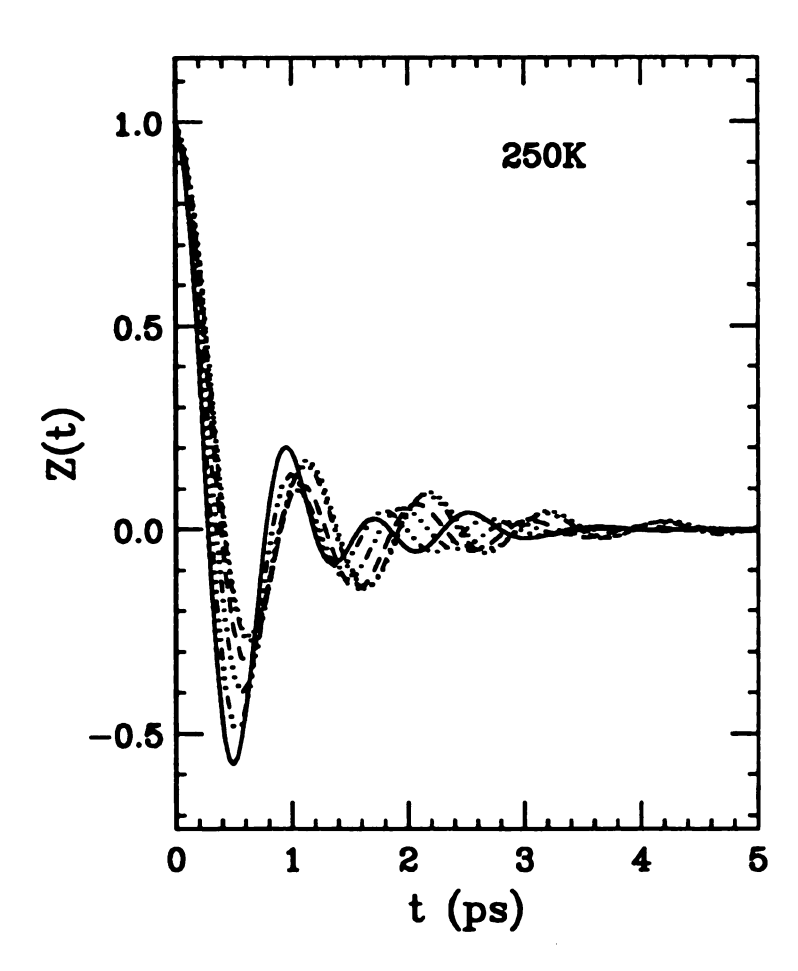


Figure 6.3: Velocity auto-correlation functions for various 2K near 250K. From the solid (bottom) curve, 2K = 0.9, 0.75, 0.55, 0.36, 0.15, and 0.

Short-time behavior of the VAF can be studied by Taylor series expansion, i.e.

$$\mathbf{v}_{i}(t) = \mathbf{v}_{i}(0) + \dot{\mathbf{v}}_{i}(0)t + \frac{1}{2}\ddot{\mathbf{v}}_{i}(0)t^{2} + \cdots$$
 (6.18)

Multiplying by  $v_i(0)$  and taking a canonical ensemble average we obtain

$$\langle \mathbf{v}_i(t) \cdot \mathbf{v}_i(0) \rangle = \langle v_i^2 \rangle + \frac{1}{2} \langle \ddot{\mathbf{v}}_i \cdot \mathbf{v}_i \rangle t^2 + \cdots$$
 (6.19)

$$= \langle v_i^2 \rangle - \frac{1}{2} \langle \dot{v_i}^2 \rangle t^2 + \cdots$$
 (6.20)

$$= \langle v_i^2 \rangle (1 - \frac{1}{2} \Omega_0^2 t^2 + \cdots), \tag{6.21}$$

where  $\Omega_0^2 = \langle |\mathbf{F}|^2 \rangle / 2mk_BT$ . Time reversal symmetry makes the odd terms in t vanish. The short time VAF is related to the mean square acceleration (or force) which is one of the basic properties of the VAF and provides information about the interaction between particles, single particle potential, and certain structural properties of the fluid. Clearly increasing the strength of corrugation potential increases  $\Omega_0^2$  resulting in a faster decrease in Z(t) starting from Z(0) = 1.

For homogeneous liquids, it is known that the intermediate time behavior of Z(t) is quite sensitive to the temperature and the density. At low density, VAF usually decays monotonically which implies the absence of many body correlation effects. As the density increases, a minimum in the VAF occurs indicating a resonant behavior or the presence of memory effects (which produce correlations between random force and velocity) in the system. Z(t) for hard spheres decreases monotonically as a function of t, with a weak but well-defined tail up to about thirty mean collision times. At higher density, VAF shows a strong oscillation qualitatively reminiscent of a damped oscillator and takes on negative values. This behavior can arise from the tagged particle being confined in a cage formed by its immediate neighbors. Negative Z(t) means that at time t a particle moves in opposite direction to that at time t = 0. Therefore, Z(t) describes a "back scattering" effect, a result of collisions between

nearest neighbors which leads to a reversal of velocity into a relatively narrow range of angles. There is a long time tail controlled by hydrodynamic conservation laws, but we are not concerned with this issue in this thesis.

We studied Z(t) for various temperatures for a fixed density. These results are equivalent to those fixing the temperature and changing the density. The rationale for this assertion is that at a given temperature, a system can change from a liquid state to a solid state by increasing its density just as one can obtain a solid state by lowering its temperature at a fixed density. Figure 6.4 is the VAF of 2K = 0.9 system for various temperatures T at a fixed density. Z(t) at high T (similar to low density) clearly shows weaker oscillations compared to that at low T (similar to high density). The weaker oscillatory t-dependence gives a larger positive value for Z(t) over time which corresponds to a higher diffusion constant.

## 6.3 Intermediate Scattering Function

Spatial Fourier transform of the density correlation function is more interesting to study because it can be measured in a laboratory.  $F(\mathbf{q},t)$ , the spatial Fourier transform of  $G(\mathbf{r},t)$ , is called the intermediate scattering function and this quantity is measured by neutron spin-echo technique [16].  $F(\mathbf{q},t)$  can be separated into two parts just like  $G(\mathbf{r},t)$ , namely, the self term  $(F_s(\mathbf{q},t))$  and the distinct term  $(F_d(\mathbf{q},t))$ .

$$F(\mathbf{q},t) = \int G(\mathbf{r},t)e^{i\mathbf{q}\cdot\mathbf{r}}d\mathbf{r}$$

$$= \frac{1}{N}\sum_{l,m}e^{i\mathbf{q}\cdot(\mathbf{r}_{l}(t)-\mathbf{r}_{m}(0))}$$

$$= \frac{1}{N}\sum_{m}e^{i\mathbf{q}\cdot(\mathbf{r}_{m}(t)-\mathbf{r}_{m}(0))} + \frac{1}{N}\sum_{l\neq m}e^{i\mathbf{q}\cdot(\mathbf{r}_{l}(t)-\mathbf{r}_{m}(0))}$$

$$= F_{s}(\mathbf{q},t) + F_{d}(\mathbf{q},t). \tag{6.22}$$

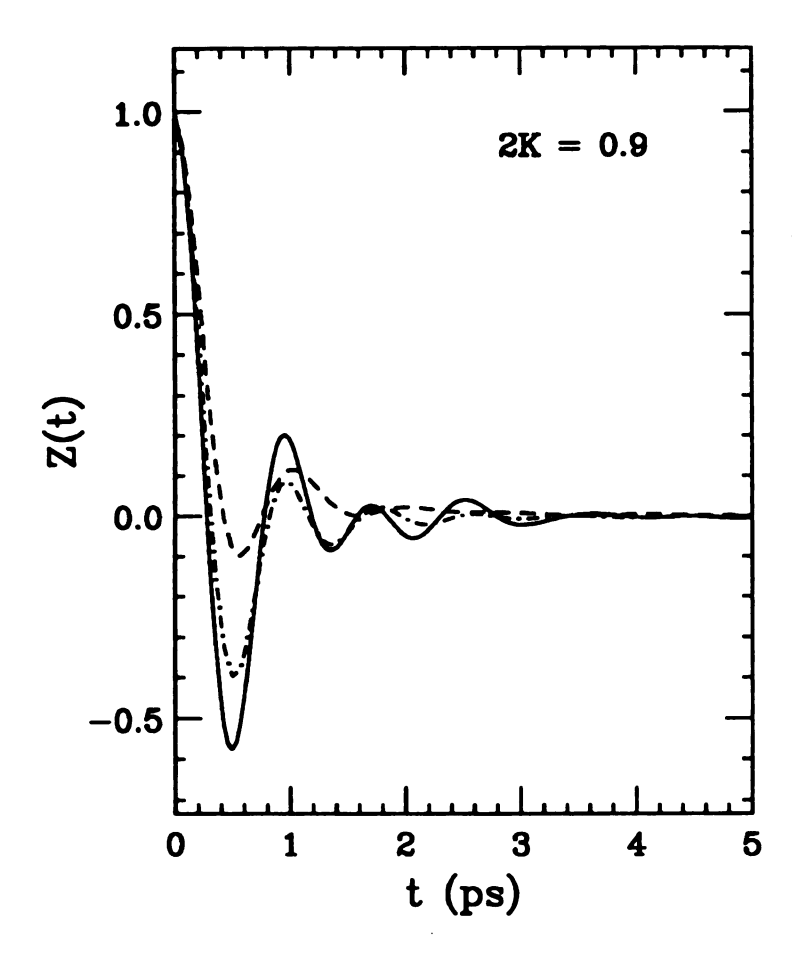


Figure 6.4: Velocity auto-correlation functions for various temperatures for 2K = 0.9. From bottom to top curve, temperature is about 250, 400, and 1450 Kelvin.

The self part describes a tagged particle motion and the distinct part describes the correlated motion. Figures 6.5-6.7 give the time dependence of  $F_s(q,t)$  for different values of q (=0.4, 1.2, and  $4\mathring{A}^{-1}$ ). Each figure has six curves which correspond to different strengths of the corrugation potential. First, let us understand the q-dependence of  $F_s(q,t)$ . For a simple homogeneous liquid such as the 2K=0 system,  $F_s(q,t)$  has the following form for small q,

$$F_{\bullet}^{D}(q,t) = e^{-Dq^{2}t}. (6.23)$$

In contrast to that for a homogeneous fluid,  $F_s^H(q,t)$  of a single harmonic oscillator with frequency  $\omega_0$  shows an oscillatory behavior and never decays. The amplitude of oscillation increases as q increases.

$$F_s^H(q,t) = e^{-\frac{k_B T}{m\omega_0^2} q^2 (1 - \cos \omega_0 t)}.$$
 (6.24)

The oscillatory behaviour of  $F_s(q,t)$  for 2K=0.9 at short times (Figures 6.5-6.7) is real and it grows as q increases. This is an effect of the corrugation which results in a harmonic oscillator-like dynamics of the tagged particle.

Now, let us focus on one of three figures (Figure 6.6) and discuss the time-dependence of  $F_s(q,t)$  for different 2K (the three figures 6.5-6.7 show qualitatively similar time-dependence, so one figure is enough for the purpose of this discussion). For very short times, these curves show no difference regardless of 2K which can be understood via a Taylor expansion of  $F_s(\mathbf{q},t)$  for short times [1].

$$F_s(\mathbf{q},t) = \sum_{n=0}^{\infty} \frac{t^{2n}}{(2n)!} F_s^{(2n)}(\mathbf{q},0)$$
 (6.25)

$$= 1 - \omega_{0s}^2 \frac{t^2}{2!} + \omega_{0s}^2 \omega_{1s}^2 \frac{t^4}{4!} - \omega_{0s}^2 \omega_{1s}^4 \frac{t^6}{6!} + \cdots, \tag{6.26}$$

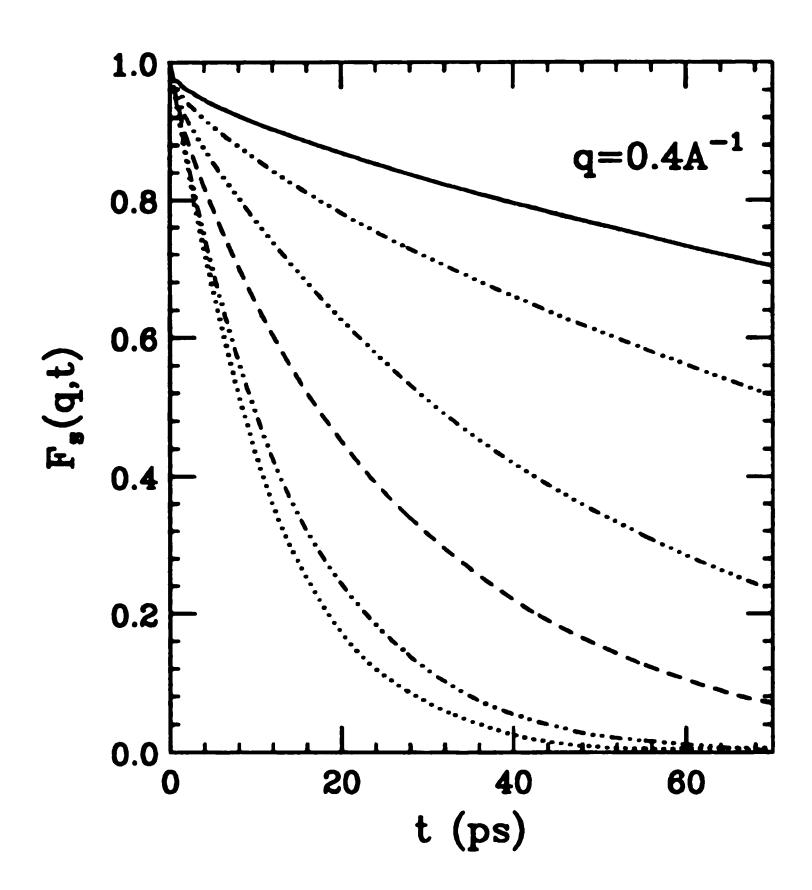


Figure 6.5: The self part of the intermediate scattering functions at  $q = 0.4 \text{\AA}^{-1}$  for different strengths of the corrugation potential. From the top curve, 2K = 0, 0.15, 0.36, 0.55, 0.75, and 0.9.

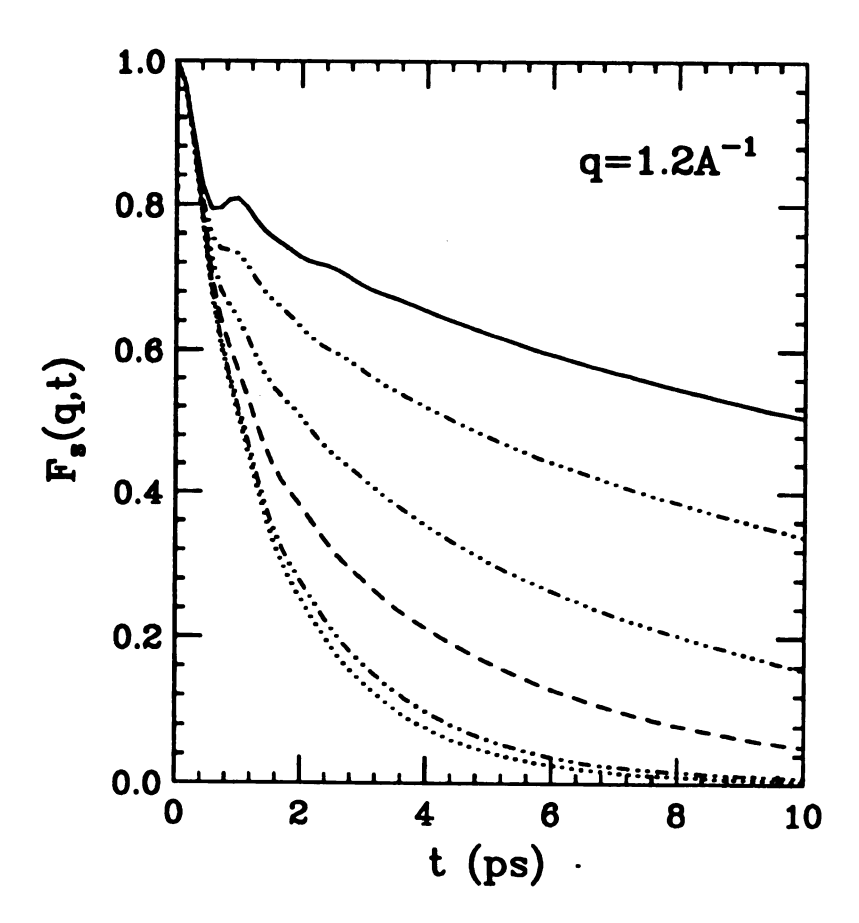


Figure 6.6: same as Figure 6.5 except  $q = 1.2 \mathring{A}^{-1}$ .

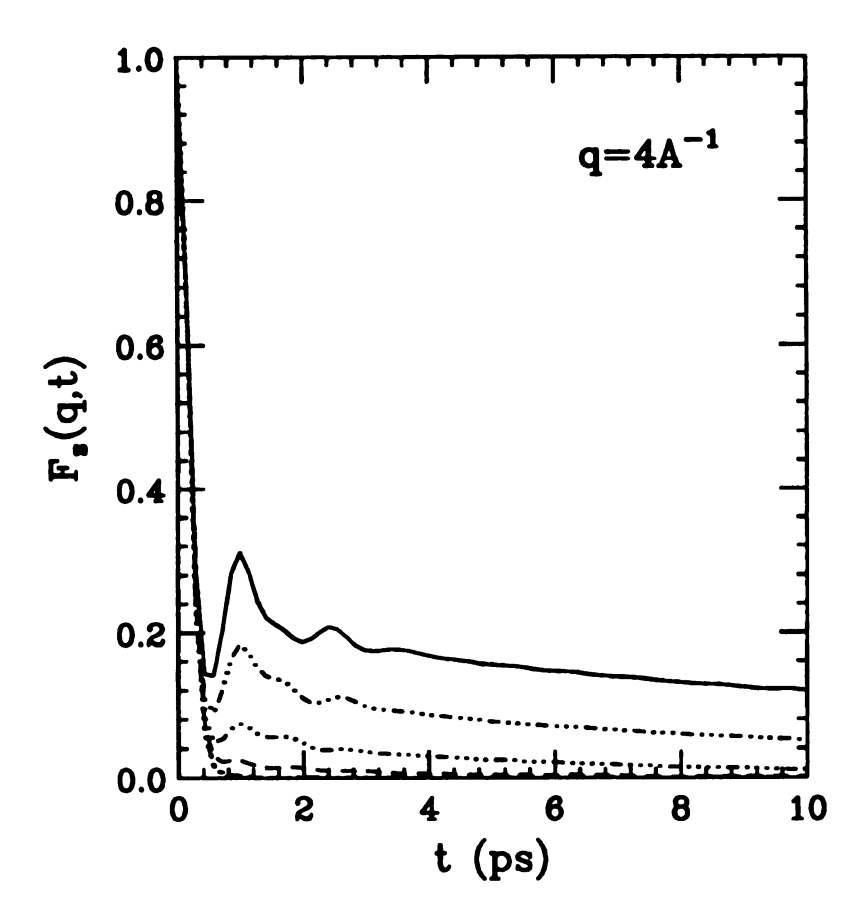


Figure 6.7: same as Figure 6.5 except  $q = 4 \mathring{A}^{-1}$ .

where

$$\omega_{0s}^2 = q^2 \frac{k_B T}{m}, (6.27)$$

$$\omega_{1a}^2 = \omega_{0a}^2 d + \Omega_0^2, \tag{6.28}$$

$$\Omega_0^2 = \frac{1}{2mk_BT}\langle |\mathbf{F}|^2 \rangle, \tag{6.29}$$

where d is the dimension of the system and  $\mathbf{F}$  is the total force acting on the particle. Eq. (6.27) clearly states that the short time behavior of  $F_s(q,t)$  is independent of the interparticle potential. Actually, this fact is easily understood because for a very short time the tagged particle cannot feel the existence of other particles and the effect of single particle potential, so it is moving like a free particle described by its average kinetic energy, or equivalently by the temperature (T) of the system through equipartition theorem. Compare the coefficient of the  $t^2$  term which involves only  $k_BT$  with that of the VAF (Eq. (6.21)) where the coefficient of the  $t^2$  term already involves the mean square acceleration. This implies that velocities of particles reach equilibrium faster than their coordinates.

At intermediate time scales, interparticle interactions start to contribute to the correlation function. We can clearly see the effect of the interaction potential on  $F_{\bullet}(q,t)$ . Also, as the strength of the corrugation potential increases, the function becomes oscillatory and also decays slowly. As will be discussed later, the oscillatory motions give rise to broad peaks at finite frequencies in the dynamic structure factor.

The decay of the  $F_s(q,t)$  with time slows down as the strength (2K) of the corrugation potential increases. Recall that the  $F_s(q,t)$  of a harmonic oscillator [14] with angular frequency  $\omega_0$  does not decay (see Eq. (6.24)). The system with corrugated potential can be approximated by a harmonic oscillator model except that the barrier height for this system is finite unlike the harmonic oscillator. Once a particle gets trapped near the minima of the corrugation potential, it takes some

time for the particle to overcome the barrier of the corrugation potential. This life time depends on how high the barrier is compared with the energy of the particle. The intermediate scattering function which relaxes rather slowly in the presence of a strong corrugation potential does not decay completely within our total MD run time. Therefore, finite MD run time corrections should be considered seriously in calculations of the Fourier transform of time correlation functions. This will be discussed in detail in the following section which deals with the incoherent dynamic structure factor.

# 6.4 Incoherent Dynamic Structure Factor

In general the dynamic structure factor  $S(q,\nu)$  which is time-Fourier transform of F(q,t) (see Eq. (6.22)) is related to the differential neutron scattering cross section [1, 7].

$$\frac{d^2\sigma}{d\Omega dE'} = \frac{d^2\sigma}{d\Omega dE'}\bigg|_{coh} + \frac{d^2\sigma}{d\Omega dE'}\bigg|_{coh}$$
(6.30)

$$= \frac{\sigma k'}{4\pi k} NS(q,\nu) + \frac{\sigma_s k'}{4\pi k} NS_s(q,\nu), \qquad (6.31)$$

where

$$S(q,\nu) = \int_{-\infty}^{\infty} F(q,t)e^{-i2\pi\nu t}dt,$$
(6.32)

$$S_{s}(q,\nu) = \int_{-\infty}^{\infty} F_{s}(q,t)e^{-i2\pi\nu t}dt. \tag{6.33}$$

Here, subscripts coh and s are abbreviations for the coherent and the incoherent (or self) respectively, E' is the final neutron energy, k and k' are the initial and the final neutron wave numbers, N is the total number of particles in the target. By varying the isotopic composition of the sample or by using polarized neutrons, it is possible to measure the incoherent and the coherent cross sections separately which

describe single particle and collective dynamics, respectively. The accessible wave numbers in inelastic neutron scattering experiments lie typically between 0.1 and 15  $\mathring{A}^{-1}$ , which is the same range of q that is usually studied in MD simulations.

Before we discuss our simulation results for various 2K, let us briefly review the experimental results. Zabel and coworkers [7, 8] have carried out neutron scattering (both quasi-elastic and inelastic) experiments in stage-2 alkali metal GICs in the fluid phase of the intercalants for a range of q values between 0.75 and  $4\mathring{A}^{-1}$ . The three most significant observations in their experiments are: (1) a diffusive central peak indicating liquid-like dynamics, (2) a broad finite frequency peak ( $\nu \sim 1 \text{ THz}$ ) whose intensity grows with the scattering wave number q, and (3) an extremely narrow resolution limited central peak whose width is considerably smaller than that of the diffusive central peak. Zabel et al. [7, 8] associated the narrow quasi-elastic central peak with a 'solid-like' dynamics, characteristics of a domain-wall solid above the melting temperature. Fan et al. [9] tried to understand the origin of this 'solidlike' response by carrying out MD simulations for  $RbC_{24}$  using a model consisting of a repulsive screened Coulomb system in the presence of a graphite corrugation potential. From the long-time behaviour of the self intermediate scattering function  $F_s(q,t)$ , Fan et al. argued that the resolution limited narrow central peak was caused by a 'solid-like' structure with a life time ~ 26ps. However, the microscopic nature of this structure, sensitivity of this life time to the MD run time and to the strength of the corrugation was not addressed in their study. Thus, what causes this extremely narrow peak in the dynamic structure factor still remains an intriguing question.

To understand the physical origins of (2) and (3) above, and how these and the diffusion rate depend on the corrugation strength and the scattering wave number

q, we have carried out extensive MD simulations in a similar repulsive screened Coulomb system but by changing the strength of the corrugation systematically and taking into account the effects of finite MD run times in our analysis. To our knowledge, this is the first study of the spectral evolution of the dynamic structure factor as one goes from a 2D homogeneous fluid (uncorrugated system) to a 2D lattice-fluid (strongly corrugated system), the corrugation potential dominating the dynamic behavior of the latter system. From our q dependent studies, we show that the observations (2) and (3) are intimately connected and are important signatures of a lattice-fluid. We also show that the anomalously narrow central peak is a characteristic of a single particle dynamics in the presence of a corrugation potential. In the absence of corrugation, as we approach the solid from the liquid phase, some of the fluid particles get trapped in a cage-potential but this does not give rise to a narrow central peak. In addition, we analyze and explain how the diffusive central peak of the incoherent dynamic structure factor narrows as one goes from a homogeneous fluid to a lattice-fluid and how the intensity of finite frequency peak changes with q.

From  $S_s(q,\nu)$  in the liquid state, one can extract the diffusion constant in the hydrodynamic limit [1, 3, 14]. However, neutron scattering experiment is not a direct way to obtain the diffusion constant if the sample is a dominant coherent-scatterer like Rb in  $RbC_{24}$  system. In this case, one uses an approximation [17] which relates  $S(q,\nu)$  to  $S_s(q,\nu)$  through the relation  $S_s(q,\nu) = S(\bar{q},\nu)$  where  $\bar{q} = q/\sqrt{S(q)}$  and S(q) is the static structure factor. This approximation is reasonable only when vibrational motions (Brillouin peaks) are well separated from the central peak of  $S_s(q,\nu)$ . MD simulation is a good method to avoid this approximation because using MD it is possible to calculate  $S_s(q,\nu)$  directly. In this section, we will focus

on the  $S_s(\mathbf{q}, \nu)$  to study the single particle dynamics. Different systems such as a classical harmonic oscillator, a simple fluid (2K = 0), and systems under the effect of the corrugation potential (host layers or substrates) are considered and results will be compared with one another to understand the effects of the corrugation on the single particle dynamics in 2D.

#### 6.4.1 Classical Harmonic Oscillator

As a guide to understand the liquid dynamic structure factor in the presence of external corrugation potential and how it evolves from the dynamics of a solid, let us look at the dynamic response of a classical harmonic oscillator. When the temperature of a system is low enough, we can use harmonic approximations to study the dynamic response of the system. In the case of a single harmonic oscillator [14] with a vibrational frequency  $\nu_0$ , one has

$$S_H(q,\nu) = \exp(-y) \sum_{n=-\infty}^{\infty} \delta(\nu - n\nu_0) I_n(y) = \sum_{n=-\infty}^{\infty} \delta(\nu - n\nu_0) A_n(y),$$
 (6.34)

where  $y = k_B T q^2/m(2\pi\nu_0)^2$  and  $I_n(y)$  is the modified Bessel function of the first kind. The frequency  $\nu_0$  is given by  $\sqrt{C/m}/2\pi$ , where C is the second derivative of the potential at its minimum. If we apply this to the system with corrugation potential,  $\nu_0 = 0.982 \times \sqrt{2K}$  (THz). For n = 0,  $A_0(y) = 1$  for y = 0 and decreases with y (see Figure 6.8) whereas for n = 1  $A_1(y) = 0$  for y = 0 and increases with y (see Figure 6.9), namely, for a given 2K (i.e.  $\nu_0$ ) the spectral weight of the central peak (finite frequency peak) decreases (increases) as q increases. Furthermore, if we compare Figures 6.8 and 6.9 for a given y (i.e. T and q), we see that  $A_n(y)$  decreases as n (i.e.  $\nu$ ) increases. For small q,  $A_n(y)$  decreases very quickly with n and for large q,  $A_n(y)$  decreases with a Gaussian shape as a function of n (or

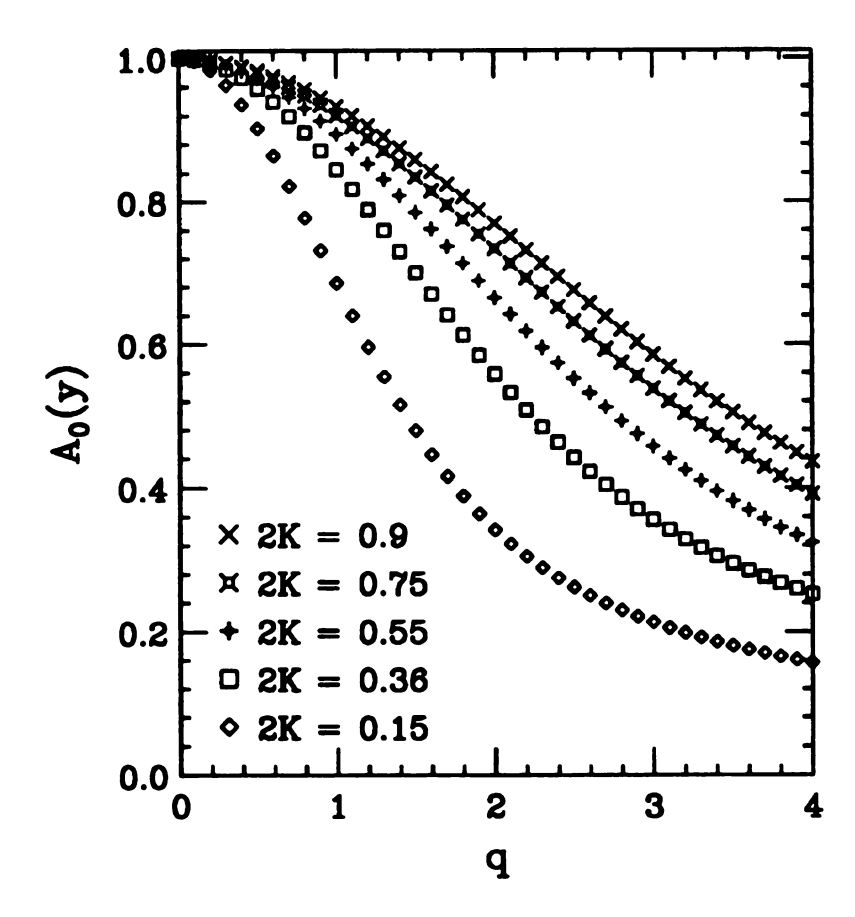


Figure 6.8: Spectral weight of the incoherent dynamic structure factor of a harmonic oscillator at  $\nu=0$  for various strengths of the corrugation potential. y in y-axis is  $k_B T q^2/m(2\pi\nu_0)^2$  where  $T=250 {\rm K}$  and m is mass for Rb.

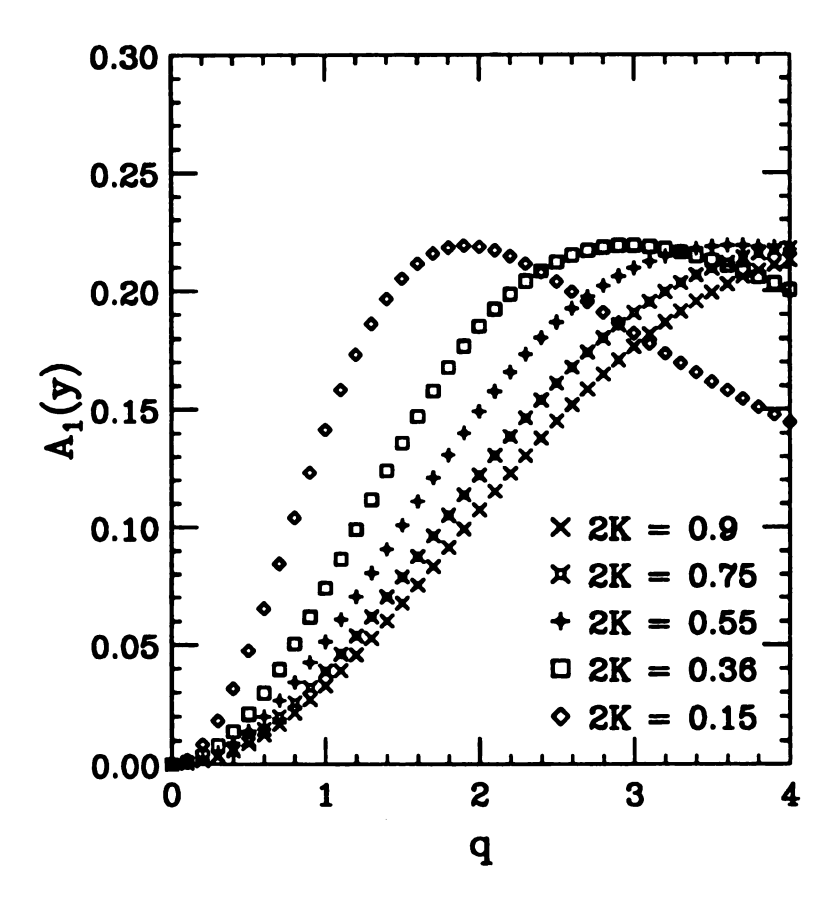


Figure 6.9: Spectral weight of the incoherent dynamic structure factor of a harmonic oscillator at  $\nu = \nu_0 = 0.982 \times \sqrt{2K}$  for various strengths of the corrugation potential. y in y-axis is  $k_B T q^2/m(2\pi\nu_0)^2$  where  $T=250 {\rm K}$  and m is mass of Rb.

 $\nu$ ) although the peaks occur at discrete values of  $\nu = n\nu_0$ , where n is an integer. Therefore, it is enough to consider only a few low frequency peaks of  $S_H(q,\nu)$ .

## 6.4.2 Corrugation-free System

Let us now discuss the dynamics of a corrugation-free (2K = 0) fluid. In Figure 6.10, we give  $S_s(q, \nu)$  vs.  $\nu$  for different values of q starting from q = 0.1 to q = 4 (in units of  $\mathring{A}^{-1}$ ) at T = 254K. The liquid to solid transition temperature for this system is about 200K [19]; thus we are not too far above the transition temperature.

In the small q and  $\nu$  limit, the incoherent dynamic structure factor has the well-known Lorentzian shape appropriate for a liquid. The Lorentzian form for  $S_s(q,\nu)$  is obtained by using the Gaussian approximation for the time dependent pair distribution function  $G_s(r,t)$ . The spatial Fourier transform of  $G_s(r,t)$  then becomes  $F_s(q,t) = e^{-Dq^2t}$ . Since time correlations in MD run are reliably known up to  $t_r$ , where  $2t_r$  is the total MD run time, we must consider this finite time range in calculating the time Fourier transform of  $G_s(r,t)$ . Taking the Fourier transform in the time interval  $(0, t_r)$ , we obtain

$$S_{s}(q,\nu) = \frac{2Dq^{2}}{\omega^{2} + (Dq^{2})^{2}} [1 - e^{-Dq^{2}t_{r}}\cos\omega t_{r}] + \frac{2\omega}{\omega^{2} + (Dq^{2})^{2}} e^{-Dq^{2}t_{r}}\sin\omega t_{r}, (6.35)$$

where  $\omega = 2\pi\nu$ . When  $t_r \to \infty$ , Eq. (6.35) recovers the well-known Lorentzian central peak,

$$S_{\bullet}(q,\nu) = \frac{2Dq^2}{\omega^2 + (Dq^2)^2}. (6.36)$$

Therefore, terms with cosine and sine in Eq. (6.35) are due to finite  $t_r$ . If we take  $\nu = 0$  in Eq. (6.35), then

$$S_{s}(q,\nu=0) = [1 - e^{-Dq^2t_r}] \times \frac{2}{Dq^2}.$$
 (6.37)

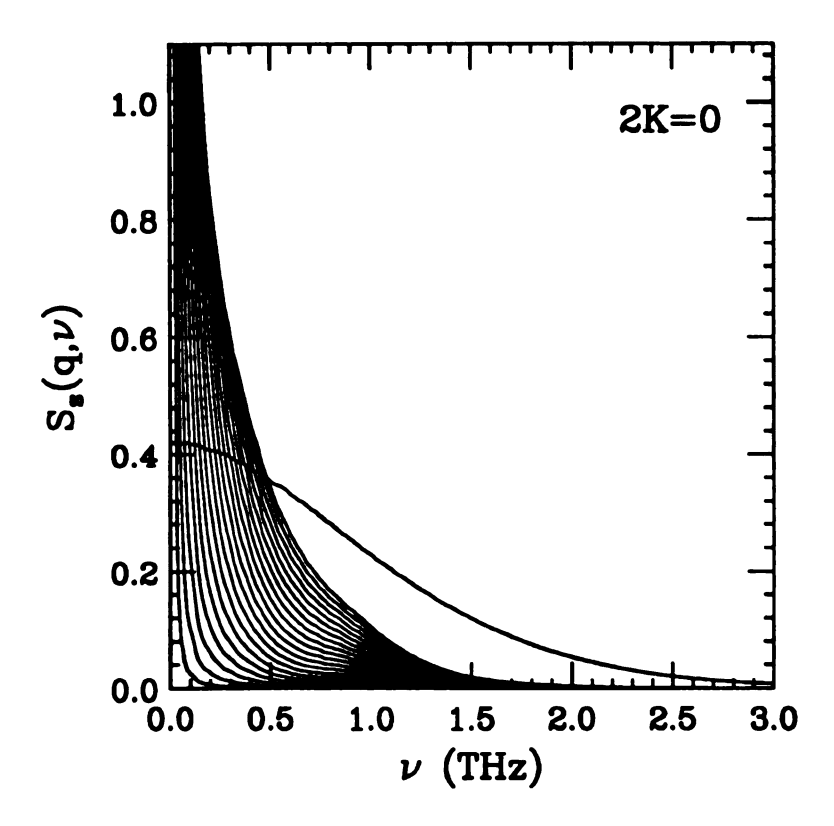


Figure 6.10: Incoherent dynamic structure factor vs. frequency for a system without corrugation (2K=0) in the liquid phase at 254K. Various curves are for different q (in  $\mathring{A}^{-1}$ ). q increases in steps of 0.1 from 0.1 to 2.0, excepting the broad curve which is for q=4 showing Gaussian-like response appropriate for a free particle.

When  $Dq^2t_r$  is less than or comparable to 1, it is important to take into account the effects of finite MD run time in obtaining the diffusion constant D from  $S_s(q,\nu)$ . For the system 2K=0, this correction term is negligible. However, the diffusion constant D decreases as 2K increases, therefore the correction factor becomes significant for large values of 2K.

By fitting  $S_s(q, \nu)$  calculated with coordinates obtained from MD simulation to Eq. (6.35), we can obtain diffusion constants. We repeat this fitting for various values of q from 0.1 to  $1\mathring{A}^{-1}$ . Figure 6.11 gives the q-dependence of D(q) for various strengths of the corrugation potential. The diffusion constant D is determined by extrapolating D(q) towards  $q \to 0$ . The value of D agrees well with that obtained from the relation  $\langle (\Delta \mathbf{r})^2 \rangle = 4Dt$  for large t, if we do not consider the value of D(q=0.1) seriously. Because q=0.1 corresponds to a length scale which is about half of the MD cell size (recall that periodic boundary condition is used), finite size effect is more serious when D is large.

Continuing with the discussions for a corrugation-free fluid, for intermediate values of q, we see a weak broad peak growing at finite frequency near 0.9THz (see Figure 6.10). The origin of this finite frequency peak can be ascribed to the dynamics of a particle trapped in the field of its nearest neighbors, the so called cage dynamics. As far as we know this is the first clear MD observation of the finite frequency cage dynamics in a 2D homogeneous fluid.

For large values of q, the central peak becomes a Gaussian which characterizes a "free" particle dynamics. Therefore, there is no qualitative distinction between diffusional and vibrational motion, both occurring on the same time scale. This dynamic structure factor at  $q = 4\mathring{A}^{-1}$  is Gaussian-like as expected for a homogeneous fluid at large values of q and there is no evidence of a narrow central peak as seen

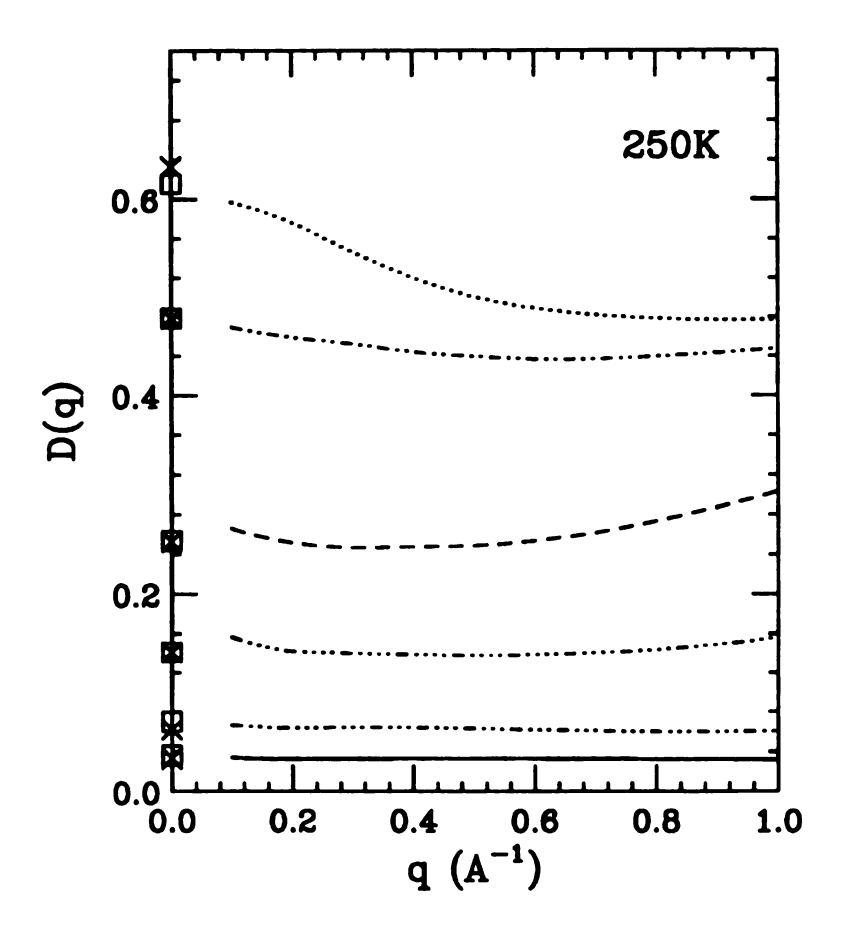


Figure 6.11: Diffusion coefficients from  $S_{\bullet}(q,\nu)$  as functions of q.  $D(q \to 0)$  approaches the value of D obtained from other methods (see Table 6.1). The symbols  $\times$  and  $\square$  at q = 0 are the values of D obtained from mean square displacements and the Fourier transform of the VAF, respectively.

in  $RbC_{24}$  neutron scattering experiments [20].

#### 6.4.3 Effect of a Strong Corrugation Potential

Now let us discuss the effect of a strong corrugation potential (2K = 0.9) on the dynamics of the fluid. Figure 6.12 gives  $S_s(q, \nu)$  for T=248K. To get a physical feeling for the strength of this corrugation, we find that the barrier height  $\Delta$  associated with only the single particle potential is 1080K. For this system the transition temperature from the liquid to the solid phase is about 220K [19]. Thus we are probing the dynamics of a highly correlated lattice-fluid since the intercalants spend considerable amount of time near the bottom of the single potential well. As we see in Figure 6.12, the spectra for 2K = 0.9 is drastically different from those for the 2K = 0 case (see Figure 6.10). The narrow central peak is indicative of Rb diffusion occurring on a time scale much slower than that of the lattice vibrations corresponding to the finite frequency peak. We find that as q increases, the height of the narrow central peak decreases while it broadens, and in addition the strength of the finite frequency peak increases. The diffusive Lorentzian central peak for small q narrows considerably in the presence of corrugation indicating a dramatic reduction in D. Fitting the spectrum to a Lorentzian with finite MD run time correction (Eq. (6.35)), which plays a very important role in this case, we obtain  $D = 0.03 \times 10^{-4} cm^2/sec$ . This value of D agrees well with a calculation of D from the relation  $\langle (\Delta \mathbf{r})^2 \rangle = 4Dt$  for large t.

When we increase q, a broad finite frequency peak (actually a doublet) grows near  $\nu \sim 1 \text{THz}$ . For large  $q \simeq 4$  i.e. when  $qa \gg 1$ , unlike the homogeneous fluid phase, the spectral function for the corrugated fluid deviates drastically from a Gaussian form. It has a narrow central peak sitting on the top of a broad central

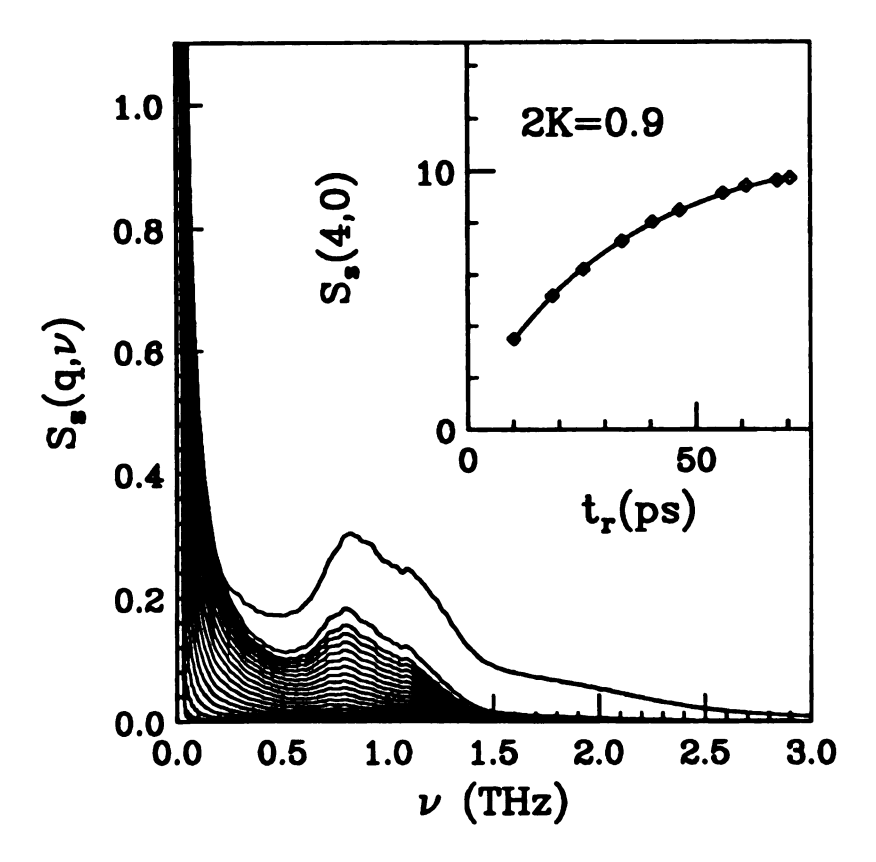


Figure 6.12: Incoherent dynamic structure factor in the liquid state (at 248K) vs. frequency for 2K = 0.9. Various curves are for different q's (in  $A^{-1}$ ) which are the same as in Figure 6.10. The uppermost curve (q = 4) is no longer a simple Gaussian. The inset gives intensities of the central peak at q = 4 as a function of the MD run time;  $2t_r$  is the total MD run time.

peak and in addition there is a broad finite frequency peak. These observations are in agreement with the inelastic neutron scattering measurements in  $RbC_{24}$  by Zabel et al. [8, 7, 21] and earlier MD simulation studies by Fan et al. [9] (see the following paragraph for more discussion).

For 0.75 < q < 2.2, Zabel et al. [7] could not fit their central peak to a single Lorentzian and suggested that the central peak actually consisted of two Lorentzians, one representing the usual liquid diffusion and the other (extremely narrow and resolution limited) corresponding to a 'solid-like' peak. For q = 4, the narrow solid-like central peak was still observed on the top of a broad liquid-like central peak [8]. Fan et al. [9] in their MD simulation study at 300K, find that  $S_s(q, \nu)$  has a very narrow central peak whose life time  $\tau$  is about 26 ps which is about half of their maximum MD run time (50ps). As discussed before, correlation functions in MD simulations can be reliably calculated up to about half the maximum MD run time. Therefore one has to take the value of  $\tau = 26$ ps with some caution. Furthermore, the precise physical origin of this narrow peak, whether due to collective or single-particle effects, was not probed by Fan et al..

To answer the questions posed above and to determine the sensitivity of  $\tau$  to the MD run time, we have analyzed  $S_s(q,\nu)$  in considerable detail and also by increasing the maximum MD run time up to  $\sim 140 \mathrm{ps}$ . We also find that for large q [21],  $S_s(q,\nu)$  shows a very narrow central peak suggesting that there is an additional contribution to the dynamic central peak beyond the usual liquid dynamics. Assuming the existence of a 'solid-like' component with life time  $\tau$  and allowing for the finite MD run time  $(2t_\tau)$  correction, we fit  $S_s(q=4,\nu=0)$  to  $C_1[1-e^{-t_\tau/\tau}]+C_2$ , where the contribution  $C_2$  comes from the usual fluid dynamics. Finite time correction to the second term is negligible because correlation function for a fluid dies out rather

rapidly for these large values of q. In Figure 6.12 (inset), we plot  $S_{\bullet}(4,0)$  vs.  $t_{\tau}(=18.53, 25.31, 33.8, 40.59, 46.53, 55.86, 60.95, 67.74, and 70.57 ps). The fact that the slope of this curve decreases with <math>t_{\tau}$  suggests that the narrow central peak is not a  $\delta$ -function. For a  $\delta$ -function time response with finite MD run time correction, the slope would have been linear. We find  $\tau=33.4$  ps which is slightly larger than 26 ps found by Fan et al. [9]. One reason for this difference is perhaps the lower temperature in our simulation than theirs and the other is the limitation in their (Fan et al.) MD run time.

## 6.4.4 Evolution of $S_s(q, \nu)$ with Strength of Corrugation

To see how the spectral function  $S_{\bullet}(q, \nu)$  evolves from 2K = 0 (homogeneous fluid) to 2K = 0.9 (lattice-fluid), we plot in Figure 6.13  $S_s(q,\nu)$  for  $q = 4.0 \mathring{A}^{-1}$  and  $0.4 \mathring{A}^{-1}$ for different values of 2K near 250K. For  $q = 4A^{-1}$ , i.e. in a short length scale  $(qa \gg 1)$ , the complex spectrum corresponding to 2K = 0.9 evolves to a Gaussian for 2K = 0 by modifying all the spectral characteristics. The finite frequency peak softens and broadens and the central peak broadens. The central and finite frequency peaks are no longer distinguishable from each other. For 2K = 0.15 ( $\Delta = 180K$ ) corresponding to the condition  $k_BT > \Delta$  (see Table 6.1 in page 117), the spectrum is close to a Gaussian but for 2K = 0.36 ( $\Delta = 432$ K) and larger i.e.  $k_BT < \Delta$ , a narrow central peak appears and its intensity grows with increasing strength of the corrugation and simultaneously a broad finite frequency peak starts to grow. When  $\Delta$  is increased still further (e.g. up to the lattice gas limit), we expect the central and finite frequency peaks to be narrow and approach a  $\delta$ -function. As we increase the temperature of a system with a nonzero 2K until the thermal energy of a tagged particle becomes larger than the barrier height  $\Delta$ , we find that the intensity of the finite frequency peak decreases and finally becomes indistinguishable with the

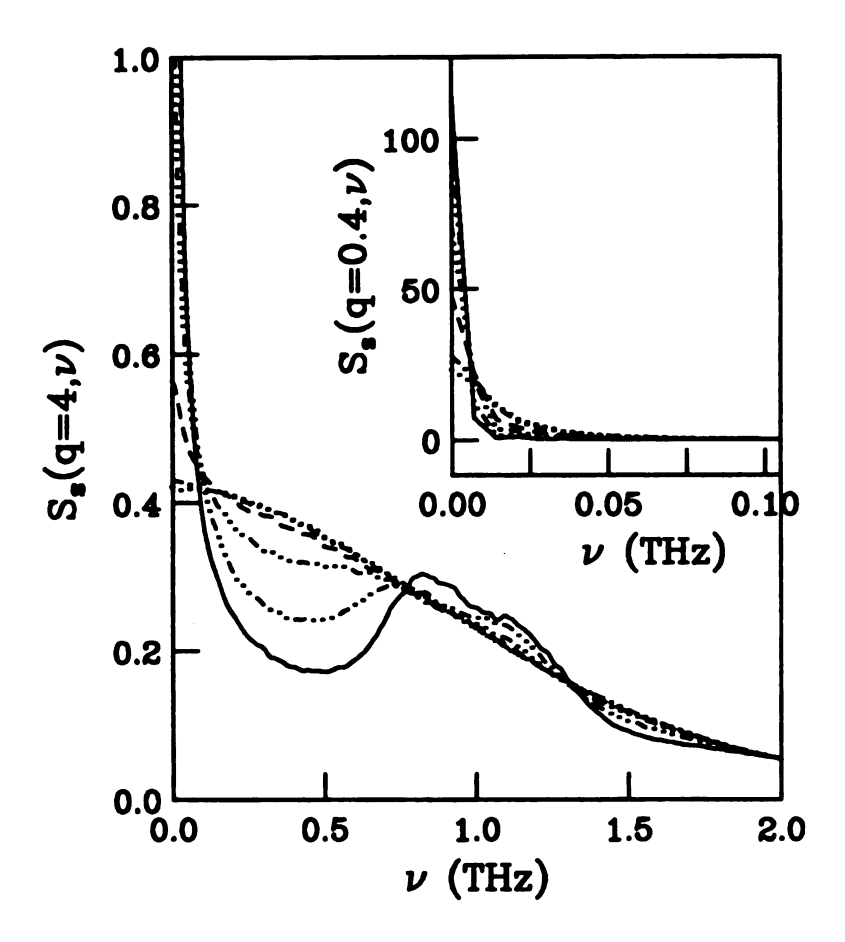


Figure 6.13: Incoherent dynamic structure factor vs. frequency for various strengths of the corrugation near 250K for  $q = 4\mathring{A}^{-1}$ . This finite frequency dynamics is due to the trapping of particles near the minima of the corrugation potential. At low frequency, we can clearly see the evolution of a sharp peak when the barrier height  $\Delta$  is higher than  $k_BT$ . Inset: Incoherent dynamic structure factor vs. frequency for various strengths of the corrugation near 250K at  $q = 0.4\mathring{A}^{-1}$ . This shows how diffusive motion slows down in the presence of the corrugation potential. We see a dramatic increase in the central peak intensity as 2K increases from 0 to 0.9.

broadening central peak and the overall shape approaches a Gaussian.

To probe the nature and origin of the resolution-limited central peak more precisely, we can go to a small wave vector. This is a distinct advantage of MD simulation over experiment where the coherent Rb scatterers preclude the probing of self correlation functions in long length scales. For q=0.4 (inset in Fig. 6.13), the entire spectrum consists of the central peak with vanishing weight in the finite-frequency peak. It can be fitted to a single Lorentzian with finite MD run time correction; its width narrows as we increase 2K. This corresponds to the slowing down of the diffusion in the presence of the corrugation potential and can be thought of as an effective mass enhancement of the diffusing intercalants caused by the corrugation potential. Within the accuracy of our calculation, there is no evidence of the very narrow 'solid-like' component due to corrugation potential in this long length scale. Thus a proper physical understanding of the origin of the 'solid-like' component must address this strong q—dependence.

A simple way to understand the origin of the narrow quasi-static central peak and the q-dependent intensity of both this and the finite frequency peak is to recall the dynamic response of a classical harmonic oscillator discussed in Sec. 6.4.1. The spectral weight of the finite frequency peak  $S_H(q, \nu = \nu_0)$  for a harmonic oscillator increases as q increases. Therefore, we understand why the finite frequency peak of 2K = 0.9 system increases as q increases. On the other hand, the spectral weight of the central peak,  $S_H(q,0)$ , decreases as q increases. For large q, even if the spectral weight of the central peak  $A_0$  decreases with q, we clearly see the narrow cental peak on top of a broad central peak. Here, we must compare the spectral weight of the narrow component with that of the fluid component of the central peak. We argue that there exists a crossover length scale characterized by a wave number

 $q^* = \sqrt{1/D\tau}$  where  $\tau$  is the average trapping time and D is the liquid diffusion rate, such that for  $q \gg q^*$ , the narrow solid-like component dominates the central peak whereas for  $q \ll q^*$ , the diffusive Lorentzian component is dominant. For the 2K = 0.9 system, we find  $q^* \approx 1$  which explains why for q = 0.4 we only see a single liquid-like diffusive peak whereas for q = 4 we see that the solid-like component dominates the spectrum. Precisely speaking,  $S_s(q = 0.4, \nu)$  is fitted with Eq. (6.35) within about 5%. If we treat this 5% difference as due to the solid-like response, the Lorentzian central peak is about 20 times bigger than the solid-like peak. On the other hand, for q = 4,  $S_s(q = 4, \nu = 0) = C_1[1 - e^{-t_r/\tau}] + C_2$ , where the contribution  $C_2$  comes from the usual fluid dynamics. We find that at 250K,  $C_1 = 10.2$  and  $C_2 = 0.84$ . Intensity ratio of the solid-like component and the liquid component is  $C_1(1 - e^{-t_r/\tau})/C_2 = 10.7$ . Therefore, in the incoherent dynamic structure factor at q = 4 for the system with 2K = 0.9 at 250K, the solid-like component is about 10 times stronger than the liquid-like component.

#### 6.5 Coherent Correlation Functions

A liquid is a dense medium where fluctuations occur continuously and spontaneously. Local perturbations from these fluctuations disturb the equilibrium state of the system. During its relaxation, each degree of freedom (or mode) of the system returns to its equilibrium. Those modes whose characteristic decay time is long compared with the molecular interaction time are the collective modes. These processes involve many particles and their relaxation time is proportional to the square of their characteristic wavelength which is large compared to the intermolecular distance (the life time of fluctuation is determined by a thermal diffusivity). The description of these long-lived collective phenomena constitutes the object of linear hydrodynamics.

To see the effect of corrugation on the collective dynamics in a 2D fluid, we consider the coherent intermediate scattering function F(q,t) and its Fourier transform which is called the coherent dynamic structure factor  $S(q,\nu)$ . F(q,t) and  $S(q,\nu)$  give a detail description of the collective modes in a fluid. First let us look at the short time behavior of the coherent intermediate scattering function,

$$F(\mathbf{q},t) = \sum_{n=0}^{\infty} \frac{t^{2n}}{(2n)!} F^{(2n)}(\mathbf{q},0)$$
 (6.38)

$$= F(\mathbf{q},0) - \omega_0^2 \frac{t^2}{2!} + \omega_0^2 \omega_1^2 \frac{t^4}{4!} - \omega_0^2 \omega_1^4 \frac{t^6}{6!} + \cdots, \qquad (6.39)$$

where  $F(\mathbf{q},0) = S(\mathbf{q})$  is the static structure factor and it gives us information about the interparticle potentials indirectly. Here,  $\omega_0^2$  is equal to  $\omega_{0s}^2$  in Eq. (6.25) which can be shown either by using the equation of continuity (mass conservation) or by simply calculating  $F^{(2)}(q,0)$  directly. Figures 6.14-6.16 give the 2K dependence of the coherent intermediate scattering function for  $q = 0.4, 1.2, \text{ and } 4\mathring{A}^{-1} \text{ near } 250\text{K}.$ The well defined oscillatory motion for  $q = 0.4 \text{\AA}^{-1}$  (Figure 6.14) is a signature of the collective mode (Brillouin peaks) which appears in the coherent dynamic structure factor  $S(q, \nu)$ . As we increase the strength of the corrugation 2K from 0 to 0.9, F(q,t) shows shorter period which leads to a shift of Brillouin peak position to higher frequency. For  $q = 1.2 \text{Å}^{-1}$  (Figure 6.15) which is very close to the value of q corresponding to the maximum of S(q), the large amplitude and the slow decay of F(q,t) is related to the strong spatial correlations that exist at this wavelength. However, the oscillatory behavior is nearly absent excepting for very large values of 2K. Figure 6.16 is quite similar to Figure 6.7 (which describes the incoherent dynamics) indicating that for  $q \sim 4 \mathring{A}^{-1}$ , namely for short wavelengths, the coherent and the incoherent density correlation functions are nearly identical telling that the self term in Eq. (6.22) dominates the pair terms in the intermediate scattering

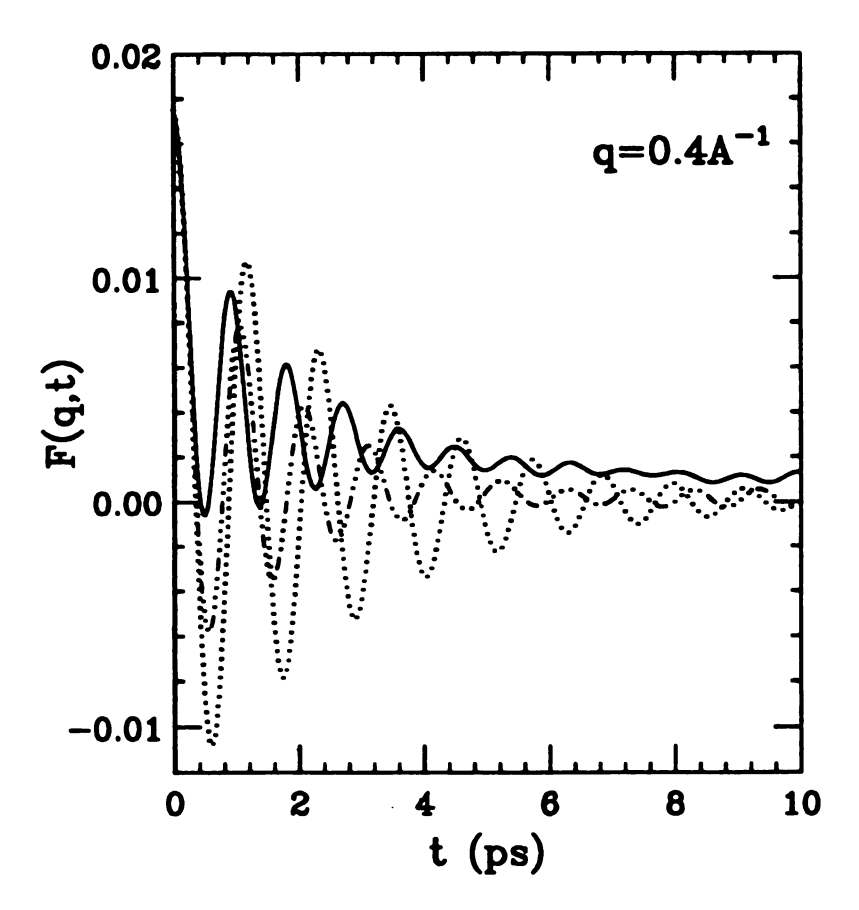


Figure 6.14: The intermediate scattering function at  $q=0.4 \mathring{A}^{-1}$  near 250K. From top (solid) curve, 2K=0.9, 0.55, and 0 (dotted curve).

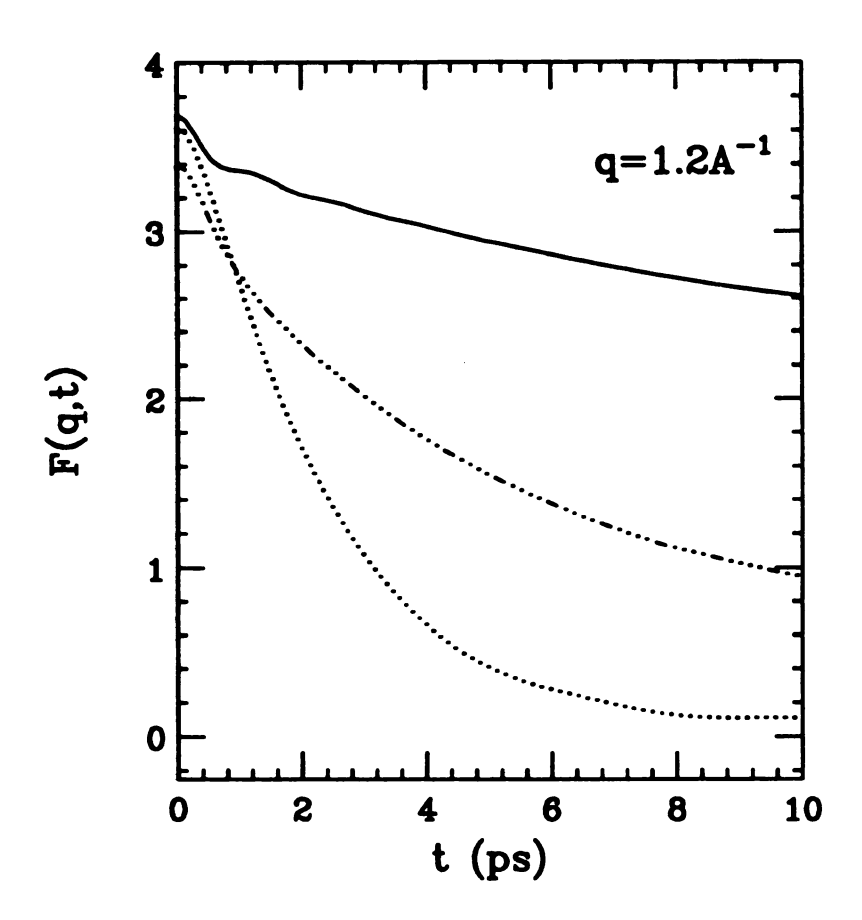


Figure 6.15: Same as Figure 6.14 except  $q = 1.2 \mathring{A}^{-1}$ 

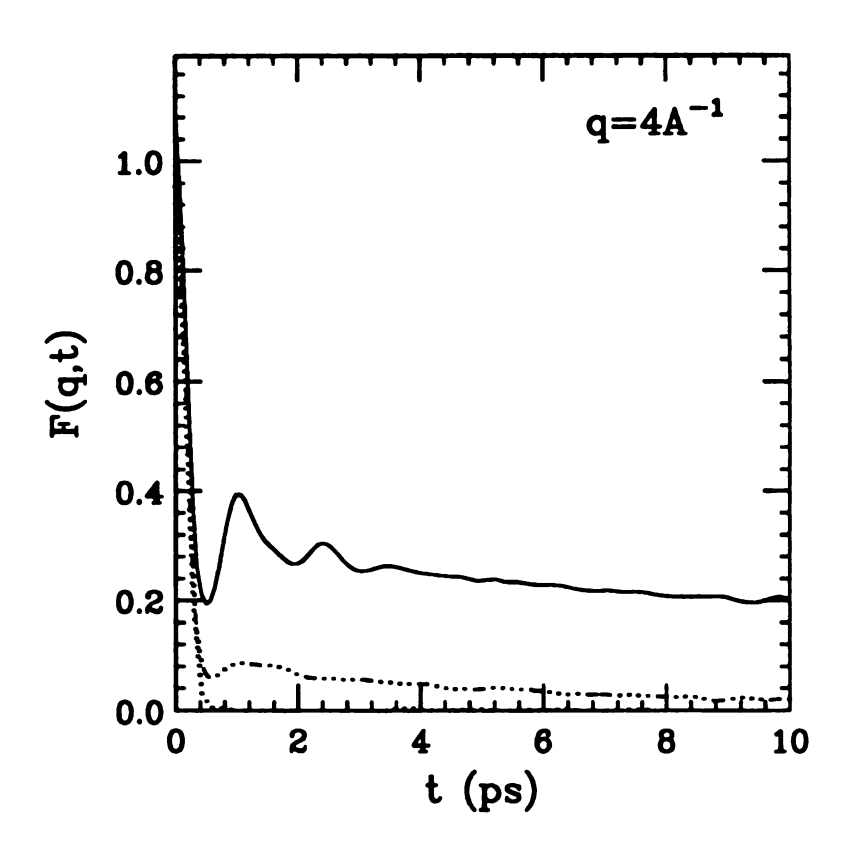


Figure 6.16: Same as Figure 6.14 except  $q = 4\mathring{A}^{-1}$ 

function.

Now, let us look at the coherent dynamic structure factor  $S(q,\nu)$  for different strengths of the corrugation potential (see Figures 6.17-6.19). At  $q=0.4 \mathring{A}^{-1}$ , we see the Rayleigh (central) peak and the Brillouin (finite frequency) peak. As we increase the strength of the corrugation, the Brillouin peak moves to a higher frequency and the peak intensity decreases. Simultaneously the central peak narrows and grows in intensity. The increasing frequency of the Brillouin peak indicates that the sound velocity increases in the presence of corrugation. At  $q=1.2\mathring{A}^{-1}$ , the strength of the Brillouin peak is negligible for all values of 2K, but the narrowing feature of the central peak persists. As we have mentioned before, at  $q=4\mathring{A}^{-1}$ , the incoherent and the coherent intermediate scattering functions are almost identical. Correspondingly  $S(q=4,\nu)$  is practically same as  $S_s(q=4,\nu)$  given in Figure 6.13. The reason that  $S(q,\nu)$  is more noisy than  $S_s(q,\nu)$  is simply because the angular averages were done exactly for  $F_s(q,t)$  (analytic integration) whereas for F(q,t), they were carried out numerical discrete summation.

Finally, let us study the sound velocity of the system by looking at the q dependence of the Brillouin peak which is the finite frequency peak in Figure 6.17. We can obtain more accurate information about the Brillouin peaks through the longitudinal current correlation function  $J_l(q, \nu)$  which is directly connected to  $S(q, \nu)$ . The relation is as follows:

$$F(q,t) = \frac{1}{N} \langle n_{\mathbf{q}}^*(0) n_{\mathbf{q}}(t) \rangle \tag{6.40}$$

$$J_{\alpha\beta}(q,t) = \frac{1}{N} \langle j_{\mathbf{q}\alpha}^*(0) j_{\mathbf{q}\beta}(t) \rangle, \qquad (6.41)$$

where

$$n_{\mathbf{q}}(t) = \sum_{l} e^{i\mathbf{q} \cdot \mathbf{R}_{l}(t)} \tag{6.42}$$

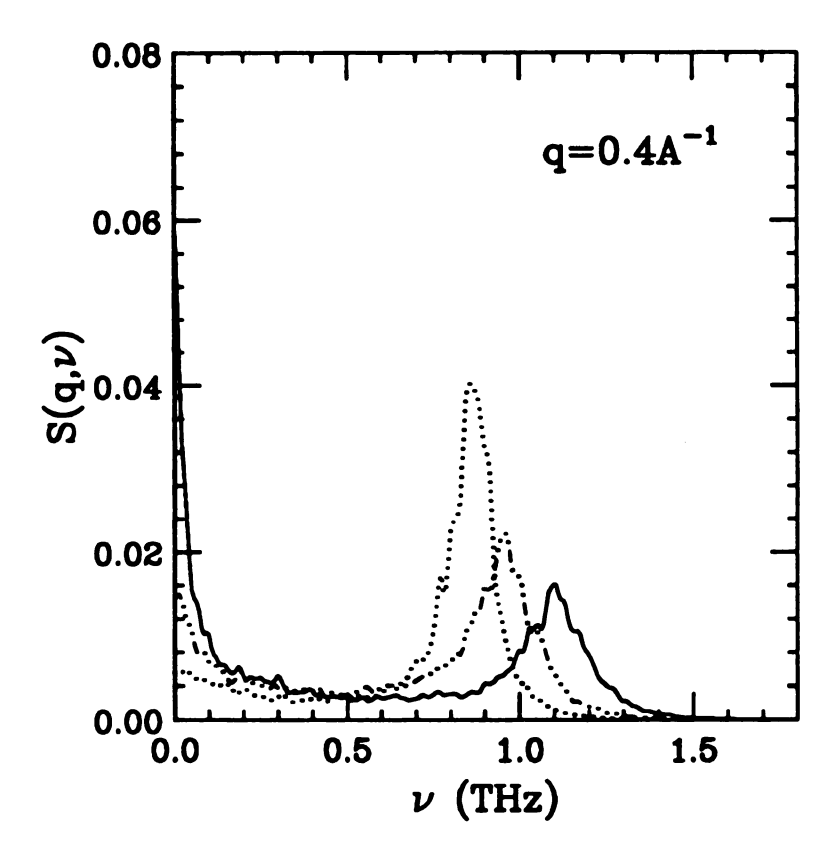


Figure 6.17: Dynamic structure factor for 2K = 0, 0.55, and 0.9 from left to right peak at finite frequency at  $q = 0.4 \mathring{A}^{-1}$ .

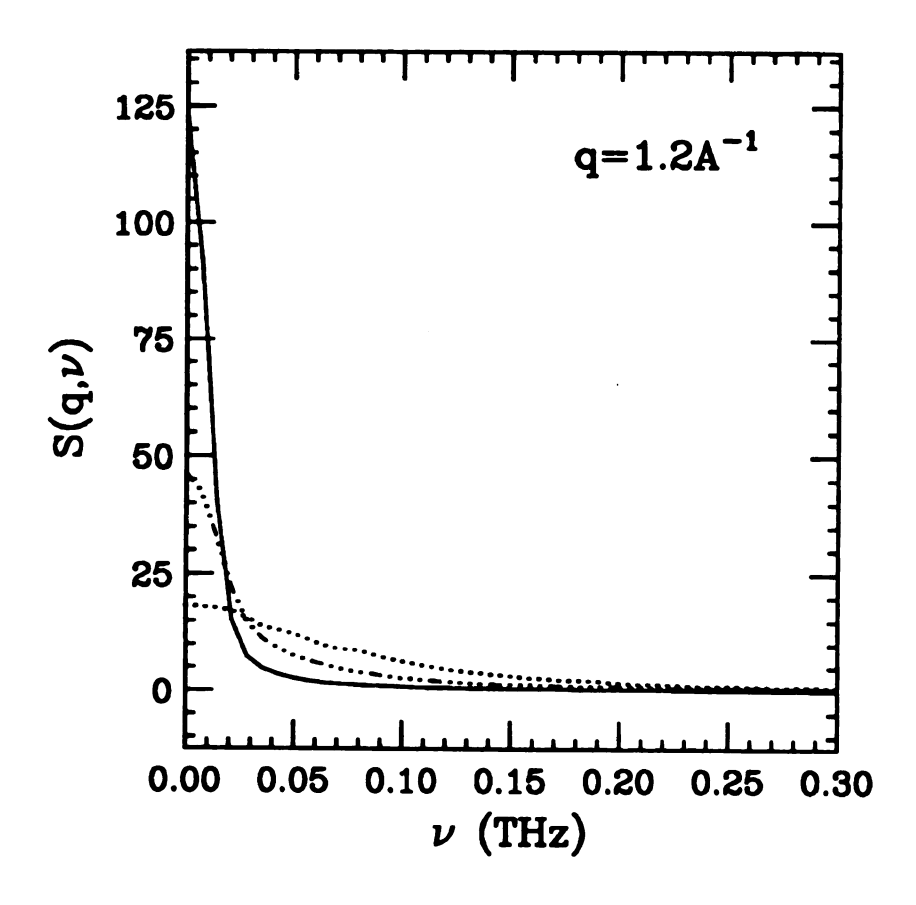


Figure 6.18: Same as Figure 6.17 except  $q = 1.2 \mathring{A}^{-1}$ 

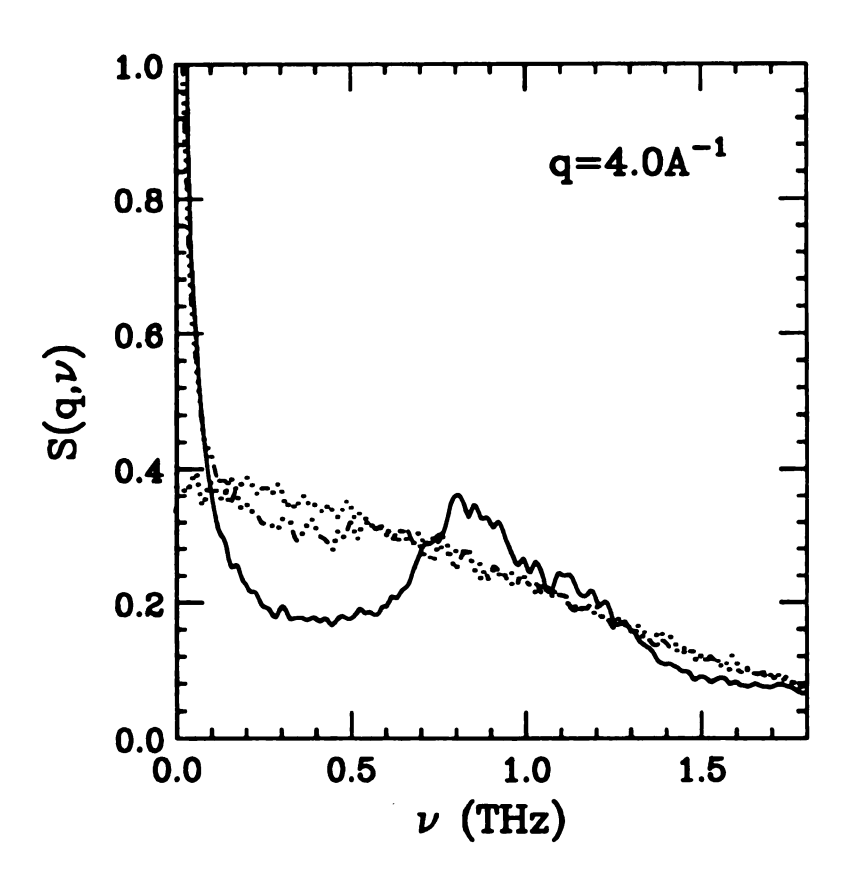


Figure 6.19: Same as Figure 6.17 except  $q = 4\mathring{A}^{-1}$ 

$$j_{\mathbf{q}\alpha}(t) = \sum_{l} v_{l\alpha}(t) e^{i\mathbf{q} \cdot \mathbf{R}_{l}(t)}. \tag{6.43}$$

By combining the two equations

$$\frac{\partial^2}{\partial t^2} F(q, t) = -q^2 J_l(q, t) \tag{6.44}$$

$$\frac{\partial}{\partial t} n_{\mathbf{q}}(t) = i\mathbf{q} \cdot j_{\mathbf{q}}(t), \tag{6.45}$$

we obtain

$$J_l(q,\nu) = (2\pi\nu)^2 S(q,\nu)/q^2. \tag{6.46}$$

This relation is exact and follows from the number conservation through the equation of continuity (Eq (6.45)). While this relation implies that the two correlation functions have the same information, certain spectral properties are more easily discerned in one function than in the other. In fact, it is more appropriate to discuss the collective modes in a liquid in terms of  $J_l(q, \nu)$  rather than  $S(q, \nu)$ . The factor  $\nu^2$  in Eq. (6.46) effectively suppresses that the central component (Rayleigh component) in  $S(q, \nu)$  which does not show up in  $J_l(q, \nu)$ . If the Brillouin peak in  $S(q, \nu)$  is sharp, it will appear also as a sharp peak in  $J_l(q, \nu)$  at the same frequency. However, if the peak in  $S(q, \nu)$  is broad, it can appear considerably distorted in  $J_l(q, \nu)$  and the peak position can be shifted to a higher frequency.

Figures 6.20 and 6.21 give the longitudinal current correlation functions as a function of q (< 0.6Å<sup>-1</sup>) for 2K=0 and 0.9. We can see how the peak position moves to a higher frequency as q increases. For the 2K=0.9, some shoulders come from the large central peak and should not be included in the collective mode response. The dispersion of the peak frequency vs. q gives us information about the sound velocity of the system in the hydrodynamic regime. In other words, the peak position in  $J_l(q, \nu)$  can be regarded as the frequency of the sound waves at that wave number q. Therefore, we plot in Figure 6.22 the q-dependence of the frequency

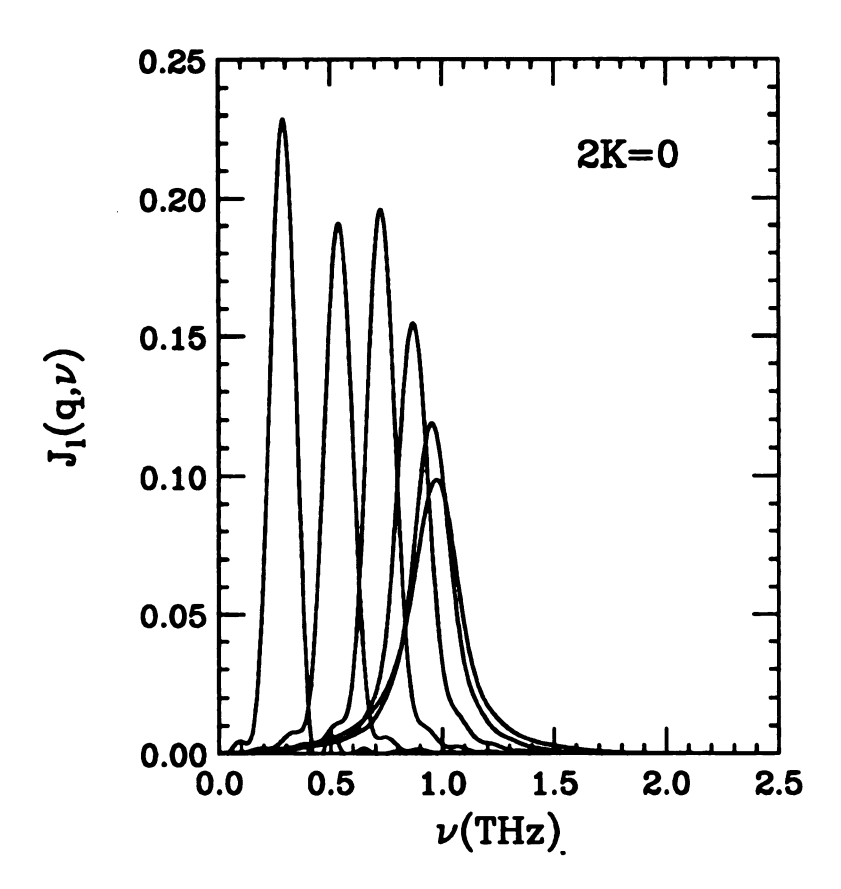


Figure 6.20: Longitudinal current correlation functions are shown as a function of q (from left q = 0.1, 0.2, 0.3, 0.4, 0.5, and 0.6 in  $\mathring{A}^{-1}$ ) for system 2K = 0.

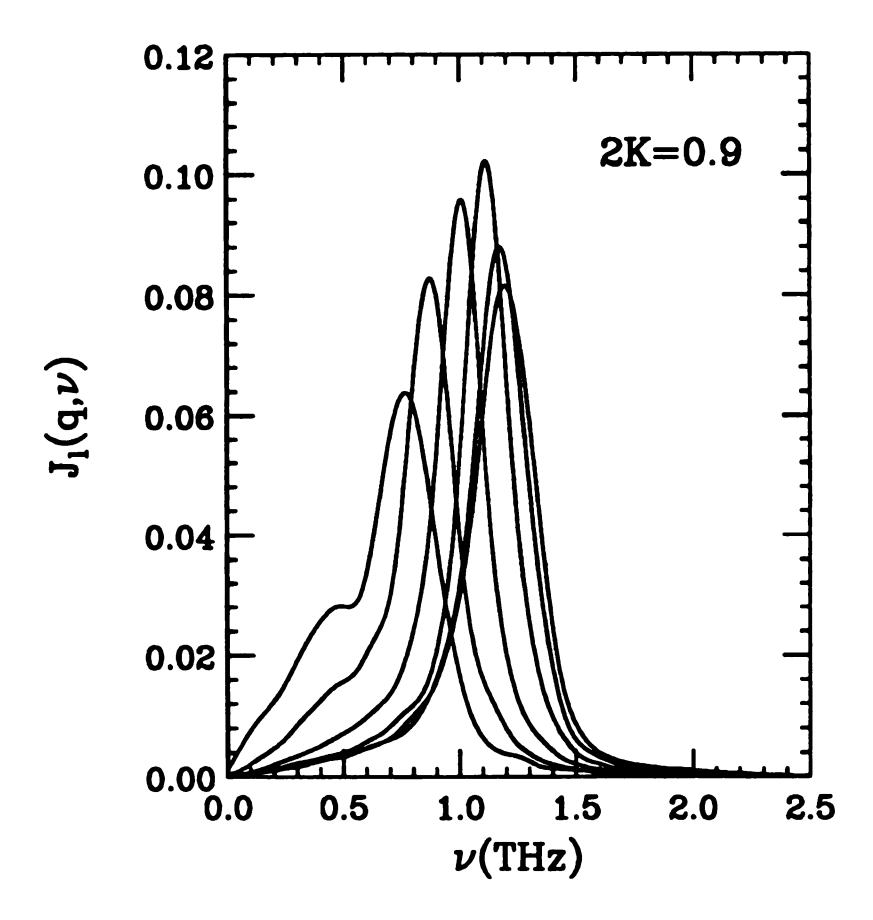


Figure 6.21: Longitudinal current correlation functions are shown as a function of q (from left  $q=0.1,\,0.2,\,0.3,\,0.4,\,0.5,\,$  and 0.6 in  $\mathring{A}^{-1}$ ) for the system 2K=0.9

at maximum intensity of  $J_l(q,t)$ . We obtain a sound velocity  $1.7 \times 10^5 cm/sec$  for the system 2K = 0 from the linear dependence of the frequency on q. However, for large 2K, we find that the collective mode frequency appears to approach a finite value as q goes to 0. For a liquid the collective mode frequency must be zero for  $q \sim 0$ . Therefore for large 2K there is a rapid increase in  $\nu_p$  as q increase from 0, thus giving rise to a high sound velocity. This is because most of the particles are trapped inside potential well and it costs a large energy to excite long wavelength collective modes. But from the finite size simulation, we are unable to get a more quantitative description of the sound wave dispersion in the small q limit in the presence of a strong corrugation potential. When we increase the temperature such that the particles can diffuse easily, we obtain the usual low sound wave frequency. For example, for the 2K = 0.9 system at high temperatures (1450K) which is above the potential barriers, the effect of the corrugation potential can be neglected and the frequency goes to 0 linearly as  $q \to 0$  as in the corrugation free system (see Figure 6.22).

# 6.6 Summary and Discussion

We have studied the effects of the corrugation potential on the dynamic properties of a two-dimensional fluid. The model system we have studied can represent not only ionic overlayers on corrugated substrates but also intercalated systems by choosing appropriate parameters. Neutron scattering studies of the dynamic structure factor at large wave numbers from a two-dimensional (2D) fluid on a corrugated substrate show an extremely narrow resolution limited central peak on the top of a fluid central peak, and a broad finite frequency peak. Using molecular dynamics simulations we reproduce all these features which are understood as general characteristics of the

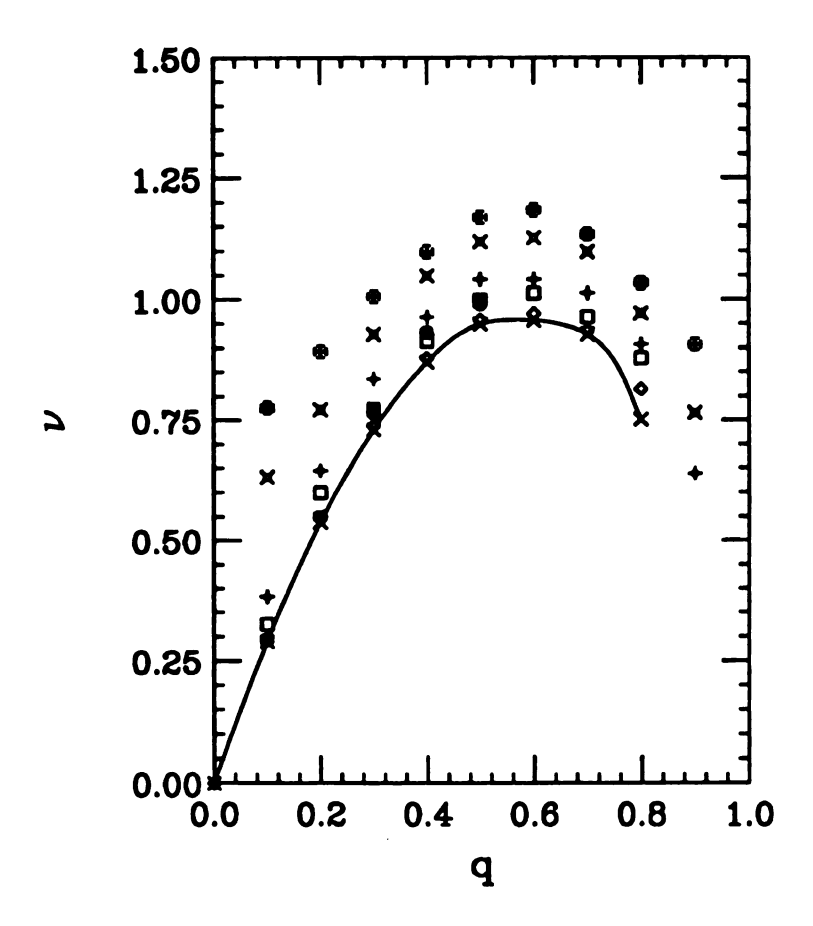


Figure 6.22: q-dependence of the frequency at maximum intensity of the Brillouin peak near 250K except that only the solid circles are at 1450K for the 2K = 0.9 system. From top to bottom 2K = 0.9, 0.75, 0.55, 0.36, 0.15, 0.

dynamics of a 2D lattice-fluid. Evolution of these spectral features as a function of the corrugation strength and scattering wave number clearly brings out the physical origin of the narrow 'solid-like' central peak. We have shown how the dynamics of a homogeneous fluid changes to that of a lattice-fluid where the fluid particles are trapped for sufficiently long time before undergoing an activated diffusion process. The corrugation potential which traps the particles with an average trapping time  $\tau$  gives rise to the 'solid-like' narrow central peak which can be seen clearly at large wave numbers. In the absence of the corrugation potential i.e. for a homogeneous fluid, even when we approach the transition to the solid phase we find no evidence of such a narrow peak at large q.

In addition to the single particle dynamics, we also studied the collective modes in the liquid state through the coherent dynamic correlation functions. For small q, we saw both Rayleigh and Brillouin peaks. The Brillouin peak is well defined enough to study the sound wave dispersion curve. For the corrugation free system, we obtain its sound velocity from the dispersion curve. As we increase the strength of the corrugation, the sound velocity of the system increases. We hope that experiments can be done in the corrugation free system to confirm our results. Also of interest will be measurements of the sound velocity propagating in the layer direction in  $RbC_{24}$  system.

# **Bibliography**

- [1] J.P. Hansen and I.R. McDonald, Theory of Simple Liquids, (Academic Press, London, 2nd edition, 1986).
- [2] M.P. Allen and D.J. Tildesley, Computer Simulation of Liquids, (Oxford University Press, Oxford, 1989).
- [3] Jean Pierre Boon and Sidney Yip, Molecular Hydrodynamics, (McGraw Hill Inc., 1980).
- [4] J. Koplik, J.R. Banavar, and J.F. Willemsen, Phys. Rev. Lett. 60, 1282 (1988);
  M. Sun and C. Ebner, Phys. Rev. Lett. 69, 3491 (1992).
- [5] P.A. Thompson and Mark O. Robbins, Phys. Rev. Lett. 63, 766 (1989) and references therein.
- [6] Graphite Intercalation Compounds, Vol 1: Structure and Dynamics, H. Zabel and S. A. Solin, eds. Springer Series on Topics in Current Physics, Springer (1990).
- [7] H. Zabel, A. Magerl, J. J. Rush, and M. E. Misenheimer, Phys. Rev. B 40, 7616 (1989).
- [8] H. Zabel, A. Magerl, A. J. Dianoux, and J. J. Rush, Phys. Rev. Lett. 50, 2094 (1983); H. Zabel, et al., Phys. Rev. Lett. 57, 2041 (1986).
- [9] J. D. Fan, George Reiter, and S. C. Moss, Phys. Rev. Lett. 64, 188 (1990).

- [10] W.A. Curtin, Phys. Rev. Lett. 59, 1228 (1987); D. Zhu and J.G. Dash, Phys. Rev. Lett. 60, 433 (1988).
- [11] M.B. Reiter, D.D. Awschalom, and N.W. Schafer, Phys. Rev. Lett. 61, 966,(1988); N.J. Wilkinson et al., Phys. Rev. Lett. 69, 3535 (1992).
- [12] S.W. Lovesey Dynamics of Solids and Liquids by Neutron Scattering p.1, Springer-Verlag, Heidelberg, (1977).
- [13] van L. Hove, Phys. Rev. 95, 249, (1954).
- [14] W. Marshall and S.W. Lovesey, Theory of Thermal Neutron Scattering, (Oxford University Press, Oxford, 1971).
- [15] B.J. Alder and T.E. Wainwright, Phys. Rev. A1, 18 (1970).
- [16] M. Davidovic and A.K. Soper, Static and Dynamic Properties of Liquids, Springer Proceedings 40, (1989).
- [17] K. Sköld et al, Phys. Rev. A 6, 1107, (1972).
- [18] Hyangsuk Seong, Surajit Sen, Tahir Çağin, and S. D. Mahanti, Phys. Rev. Rapid Communications B45, 8841 (1992).
- [19] Hyangsuk Seong, S. D. Mahanti, Surajit Sen, and Tahir Çağin, Phys. Rev. B 46, 8748 (1992).
- [20] W.A. Kamitakahara and H. Zabel, Phys. Rev. B 32, 7817 (1985).
- [21] Although Zabel et al. measured coherent scattering structure factor, for  $q = 4\mathring{A}^{-1}$ , the coherent and the incoherent structure factors are nearly the same. Furthermore we find that with increasing temperature the doublet peak structure becomes a single one as seen in Zabel et al. experiment [7].

# Chapter 7

# Multiphonon Response in 2D Corrugated Systems

## 7.1 Introduction

As discussed in the introduction and in more detail in chapters 4 and 5, atomic and molecular overlayers on corrugated substrates and intercalants inside host layers exhibit a rich variety of structures depending on the size of the atoms (or intercalants), planar density, and the strength and period of the substrate (or host) corrugation potential [1, 2]. Melting and dynamic properties of some of these physical systems which exhibit incommensurate ground state structure (or a discommensurate domain-wall structure) have been of considerable experimental and theoretical interest [3, 4]. For melting of an incommensurate solid, the main interest was to understand the physics underlying the domain and domain-wall melting [3, 5] which we covered in chapter 5. As regards the dynamics of the incommensurate solid, some of the fundamental questions related to, for example, the existence of low-frequency modes and how the in-plane vibrational modes reflect and probe the discommensuration structure and the atom-substrate interaction [6, 7, 8]. In this chapter we address these dynamics questions with the intercalants inside graphite host layers

as our model systems.

Kamitakahara and Zabel (KZ) [7, 8] investigated the phonon density of states (PDOS) associated with the in-plane vibration of the intercalants in a large class of alkali metal GICs using inelastic neutron scattering experiments with scattering wave number  $(3.5 < q < 4.5 \text{Å}^{-1})$  for which the incoherent approximation [9] was found to be justified. Here we focus on the stage-n  $(n \ge 2)$  GICs (in particular  $RbC_{24}$ ) where 2-dimensional models have been quite successful [10]. The PDOS for  $RbC_{24}$  extracted by KZ (to be denoted as  $g(\nu)$ , see Figure 7.1) shows two peaks, one near 1THz and the other near  $2 \sim 2.6$ THz. Even above the melting temperature (experimentally,  $T_m \sim 162$ K) when the intercalants form a 2D lattice-fluid, some anharmonicity becomes noticeable, but nothing dramatic happens to  $g(\nu)$ . The frequency of the first peak near 1THz was interpreted by KZ to be proportional to the strength of the Intercalant-Carbon (I-C) in-plane interaction and was therefore expected to depend critically on the location of intercalants with respect to the graphite substrate. As pointed out by KZ, this low frequency peak was surprisingly well defined at low temperature in spite of the fact that many of the intercalants in the discommensuration domain structure [10, 11] did not sit precisely at the commensurate sites and therefore experienced a distribution of I-C interactions.

KZ associated the two main peaks with the in-plane transverse (TA) and longitudinal (LA) acoustic modes respectively. They observed that the low-frequency peak (TA) was still dominant above the melting temperature whereas the high-frequency peak (LA) broadened remarkably. This is very surprising because even if we consider the effect of corrugation in the liquid state, we expect the LA modes to be still better defined than the TA modes. Furthermore, KZ could fit  $g(\nu)$  obtained from the lattice dynamics calculations with their experiments in the stage-1 K and Rb GICs

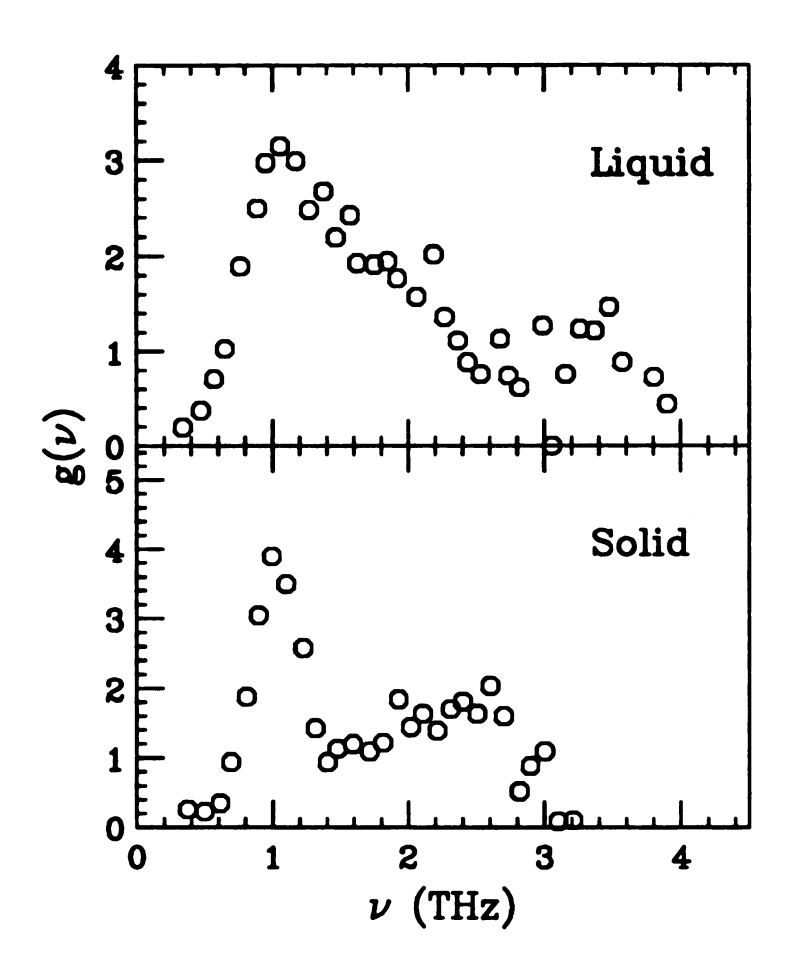


Figure 7.1: Intercalant in-plane mode phonon density of states from Kamitakahara and Zabel [7] for  $RbC_{24}$ . Top (bottom) panel is in liquid (solid) state.

[7, 8, 12] only if they used an unscreened Coulomb interaction. They assigned the high frequency peak to collective mode (plasma oscillation) of unscreened  $K^+$  and  $Rb^+$  ions. If one assumes that there is no screening in stage-1 GICs, this assumption becomes even more reasonable for the higher stage GICs because of their lower electronic density. Therefore one should be able to fit even better the  $2 \sim 2.6 \text{THz}$  peak in  $RbC_{24}$  using the unscreened Coulomb model. However, we calculate this collective mode frequency to be  $\sim 1.35 \text{THz}$  thus making the unscreened Coulomb model inadequate. Also it is difficult to accept the no screening picture in alkali metal GICs because of the metallic nature of the system.

In their MD simulation studies for  $RbC_{24}$  using a screened Coulomb model, Fan et al [13] found two peaks in the self dynamic structure factor  $S_s(q,\nu)$ . The first peak was pronounced and centered around 1THz while the second peak was very weak and centered around 2THz. Fan et al. following KZ's suggestions, tentatively assigned the first peak to TA and the second peak to LA mode without studying how these peaks changed with temperature (by going to the solid state) to confirm this identification.

In this chapter we propose a completely different explanation of the observed multipeak structure seen in neutron scattering experiments. We show that although in general it is difficult to observe multi-phonon response, particularly in the liquid phase, the substrate corrugation significantly enhances the strength of multiphonon response. We present the results of our calculation of PDOS of the stage-2 Rb GIC obtained via both Fourier transform of the velocity auto-correlation function (VAF) which we will refer to this as  $g_H(\nu)$ , and also from the incoherent dynamic structure factor following a procedure that KZ used (defined  $g(\nu)$ ). We have used MD simulations of a 2-dimensional repulsive screened Coulomb system on corrugated

layers to obtain both  $g_H(\nu)$  and  $g(\nu)$ . This model, as discussed in earlier chapter of this thesis, has been very successful in describing the structure [10], melting [14], and dynamics in the fluid phase [15] of the stage-2 Rb GIC. Our present MD simulation results for  $g(\nu)$  not only agree with that obtained from the inelastic neutron scattering experiments [7] but also elucidate the origin of the two-peak structure. Details about the potentials and MD simulations have been already discussed in chapter 4.

In order to see how the phonon dynamics depends on the strength of the corrugation and the intercalant density, we will consider three systems; system I with planar density 0.0318 per  $Å^2$  in the absence of substrate potentials i.e. no graphite layers, system II with the same planar density as the system I but in the presence of host layers (or substrates), and system III with 0.0311/Å<sup>2</sup> whose ground state structure is the periodic domain wall structure discussed that in chapter 4. This classification is the same as that in chapter 5. The systems II and III are incommensurate and commensurate solids, respectively. The strength of corrugation is chosen to be 2K = 0.9, appropriate for  $RbC_{24}$ . Comparison of the dynamics of systems with slightly different densities tells us about the role of atomic defects in the vibrational excitations of commensurate and incommensurate solids. Layout for this chapter is following. First, we will discuss the PDOS through lattice dynamics calculations for systems I and III. Next the PDOS for the system II will be obtained from the Fourier transform of the VAF and through the incoherent dynamic structure factor. Finally, the results of a harmonic oscillator model will be presented to illustrate the wave number (q) dependence of a quantity related to the PDOS but obtained from the incoherent dynamic structure factor  $S_s(q, \nu)$ .

#### 7.2 Lattice Dynamics

In this section, we briefly review the theory of the vibrations of a crystal lattice [16]. The atomic displacements are assumed to be small so that the forces are regarded as linear functions of the displacements. The force constants between atoms are known as the second derivatives of the interatomic potentials with respect to the atomic displacements. This is the usual harmonic approximation where the lattice vibrations are treated as a collection of coupled simple harmonic oscillators. The Hamiltonian of the system is

$$H = \frac{1}{2} \sum_{\alpha i \kappa} M_{\kappa} \dot{u}_{\alpha i \kappa}^2 + \frac{1}{2} \sum_{\alpha i \kappa, \beta j \mu} \Phi_{\alpha \beta, i \kappa, j \mu} u_{\alpha i \kappa} u_{\beta j \mu}, \tag{7.1}$$

where

$$\Phi_{\alpha\beta,i\kappa,j\mu} = \left[\partial^2 \Phi / \partial u_{\alpha i\kappa} \partial u_{\beta j\mu}\right]_0, \tag{7.2}$$

 $\Phi$  being potential energy of the system. For system I,  $\Phi$  is just the repulsive screened Coulomb potential whereas for systems II and III, the corrugated potential is also included (see chapter 4) in  $\Phi$ .  $u_{\alpha i\kappa}$ 's are the displacements of atoms from their equilibrium positions and the subscripts stand for the  $\alpha$ th rectangular component of the  $\kappa$ th atom in the *i*th unit cell. The equations of motion for the atoms are then easily found to be

$$M_{\kappa}\ddot{u}_{\alpha i\kappa} = -\sum_{\beta j\mu} \Phi_{\alpha\beta,i\kappa,j\mu} u_{\beta j\mu}. \tag{7.3}$$

Choosing periodic solutions to Eq. (7.3) (using Bloch's theorem)

$$u_{\alpha i\kappa} = \frac{1}{\sqrt{M_{\pi}}} u_{\alpha\kappa}(\mathbf{q}) e^{-i\omega t + i\mathbf{q} \cdot \mathbf{R}_i}, \tag{7.4}$$

we obtain

$$\omega^2 u_{\alpha\kappa}(\mathbf{q}) = \sum_{\beta\mu} D_{\alpha\beta,\kappa\mu}(\mathbf{q}) u_{\beta\mu}(\mathbf{q}), \tag{7.5}$$

where

$$D_{\alpha\beta,\kappa\mu}(\mathbf{q}) = \frac{1}{\sqrt{M_{\kappa}M_{\mu}}} \sum_{\mathbf{R}_{i}-\mathbf{R}_{j}} \Phi_{\alpha\beta,i\kappa,j\mu} e^{-i\mathbf{q}\cdot(\mathbf{R}_{i}-\mathbf{R}_{j})}.$$
 (7.6)

 $\overrightarrow{D}$  is referred to as the 'Dynamic Matrix' and  $\mathbf{q}$  is the wave vector of the phonon. For a crystal with r atoms in a unit cell and each atom having d degrees of freedom, the number of equations to be solved is rd [Eq. (7.5)].

We have obtained the dispersion relation  $\omega = \omega_j(\mathbf{q}) \ (j=1,2,\cdots,2r)$  by solving Eq. (7.5) for the systems I and III where we have used d=2 by considering only the motion of atoms parallel to the plane. Since system II has no periodicity (incommensurate solid), it is not possible to use a simple unit cell with a small number of basis atoms for lattice dynamics calculations. We can form a unit cell with 7-atom basis for the system III. Therefore, to directly compare the normal mode frequencies and PDOS in systems I with those of the system III, we also choose a 7-atom basis conventional cell for the system I (see Figure 7.2). Figure 7.3 shows the dispersion curves for both the systems along the (10) direction of its unit cell. We have 14 branches which come from 7 (=r, number of basis atoms)  $\times$  2 (=d, degrees of freedom). The figure also shows the linear dependence of the two acoustic modes (LA and TA) for small q (long wavelength limit) for the system I. However, the phonon spectrum for the system III whose ground state is a commensurate structure shows a gap due to pinning by the corrugation potential [8]. Furthermore the phonon dispersion becomes very narrow in the presence of the corrugation potential. Once we know the dispersion curves, we can obtain the PDOS,  $g_H(\nu)$ , through

$$g_H(\nu) = \frac{1}{2N} \sum_{j,\mathbf{q}} \delta(\nu - \nu_j(\mathbf{q})),$$
 (7.7)

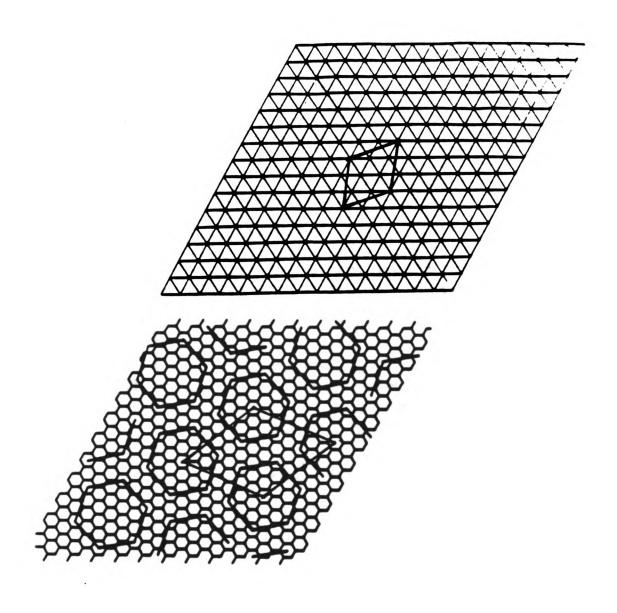


Figure 7.2: Top panel is the ground state structure of system I (without corrugation potential) and the bottom panel is domain and domain wall structure which is the ground state structure of system III (with corrugation potential).

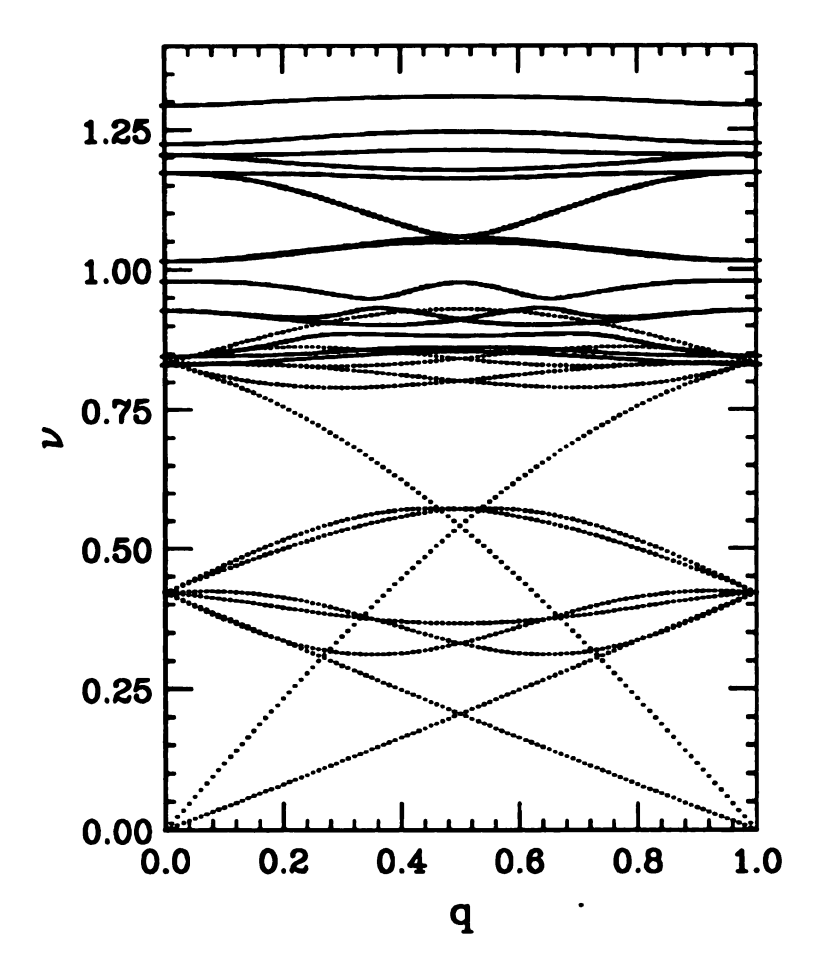


Figure 7.3: Dispersion curve for the system I (dotted lines) and the system III (solid lines). Notice the difference not only in the shape but also in the acoustic branches. The direction of q is along the (10) reciprocal lattice vector of the unit cell.

where  $\nu_j$ 's are the 2N normal mode frequencies. To get the PDOS, we have carried out the summation over a regular grid of  $\mathbf{q}$  values by taking a sufficiently large area in the  $\mathbf{q}$  space. If enough points are selected (about 100,000),  $g_H(\nu)$  converges to the correct result [17]. In Figure 7.4 the result for the system I (without corrugation potential) is given and provides a check of our calculation procedure because the ground state of this system is known to be a triangular lattice whose PDOS is exactly known. The PDOS for system III shows a gap in the low frequency region where vibrational modes are forbidden due to the commensurate nature of the ground state. The gap depends on the strength of the corrugation potential. Spiky structure in  $g_H(\nu)$  for system III indicates that its normal mode dispersions are much smaller than that for the corrugation-free system.

# 7.3 Phonon Density of States through Velocity Auto-correlation Function

For system II whose ground state is an incommensurate structure, it is difficult to calculate the PDOS associated with harmonic vibrations  $g_H(\nu)$  by going through the normal mode frequency analysis. Although the systems II and III differ only slightly in density, this small difference leads to completely different ground state structures and it is very difficult to handle the dynamics of the system II analytically because we cannot choose a simple unit cell with a small number of basis atoms for this system. Strictly speaking, there is no unit cell for this system. The way one can handle this problem is through MD simulation. It is well known that  $Z(\nu)$  (Fourier transform of VAF) is directly related to the PDOS in a harmonic system [18]. In Figure 7.5, we compare  $Z(\nu)$  for system II and system III and can see the effects of corrugation potential and atomic defects on the density of vibrational states. The

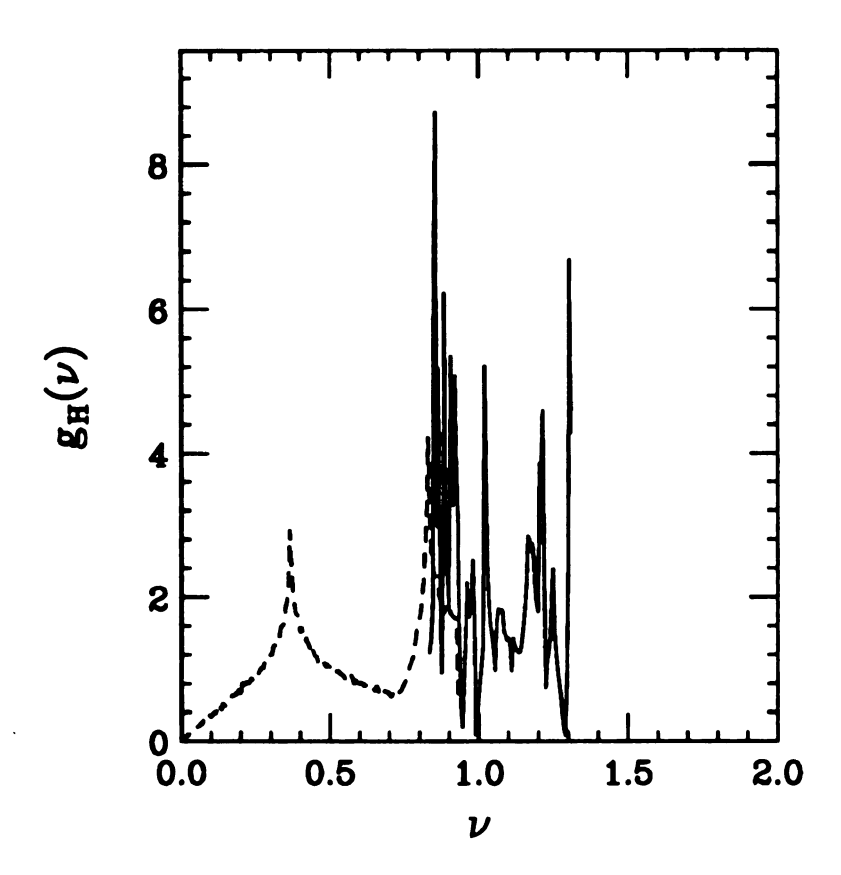


Figure 7.4: Phonon density of states for the same density of system III but without corrugation potential (dotted line) and system III (solid line) through lattice dynamics in harmonic approximation with next nearest neighbor interaction. Notice the gap for the system III due to corrugation potential.

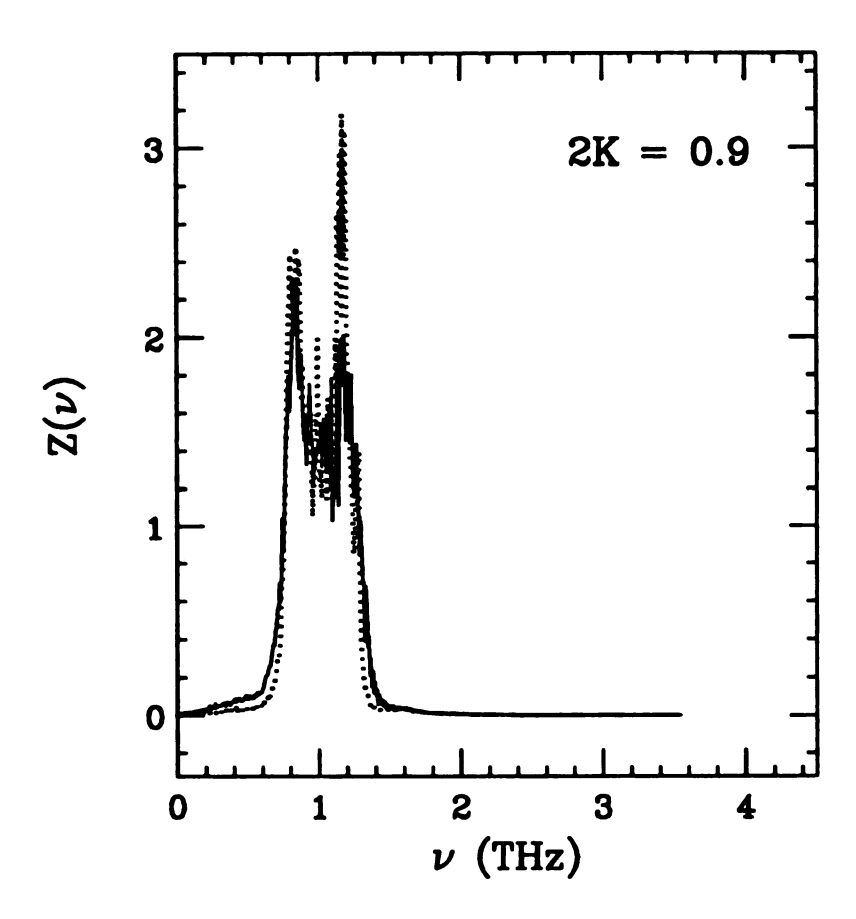


Figure 7.5: Fourier transform of the velocity auto-correlation functions near 150K. Notice the small difference in  $Z(\nu)$  between system II (solid line) and III (dotted line) in low frequency region. In system II which is an incommensurate solid, there are long wavelength phonons which appears to be a linear density of states. Low frequency modes are remarkably suppressed due to the corrugation potential.

PDOS for the system II shows the existence of a few allowed modes in the low frequency region. Physically, the ground state of II can be thought of as that of III (periodic domain-wall structure) with a few atomic defects caused by the additional intercalants in the former. We attribute the small difference in the low frequency PDOS between systems II and III to the existence of long wave length phonons in the incommensurate solid. The reason we do not attribute this difference to thermal effects is because the temperature is nearly the same in both the systems. Also, the number of thermally excited topological defects such as disclination pairs are nearly the same in both the systems (see chapter 5). The very small tail in  $Z(\nu)$  seen in the system III in the low frequency region (see Figure 7.5) at this temperature is due to anharmonicity and/or thermally excited disclination pairs, and major source of the difference between the systems II and III is primarily due to the defects in the former.

Parameters for the system II were chosen as appropriate for the  $RbC_{24}$ . Therefore, we can compare the results for this system with experimental data. In Figure 7.5, we see that  $Z(\nu)$  for the system II shows a peak (actually a doublet structure separated by about 0.3THz) near 1THz and its overall width is about 0.5THz. Furthermore,  $Z(\nu)$  does not show any discernible peak near 2THz contrary to the experimental  $g(\nu)$  (see Figure 7.1) given in Ref. [7] obtained from the incoherent dynamic structure factor. To unravel this puzzle we must look at the procedure KZ used to obtain  $g(\nu)$  from their inelastic neutron scattering experiment.

# 7.4 Phonon Density of States through Incoherent Dynamic Structure Factor

To understand why KZ saw two peaks one near 1THz and the other near 2THz, we briefly review the method KZ [7] used to obtain  $g(\nu)$  from their neutron scattering data. Although Rb is a coherent scatterer, if one takes a sufficiently large q and considers all possible crystalline orientations in the intercalant plane (perpendicular to the graphite c-axis) then one can use the incoherent approximation i.e.  $S_{coh}(q,\nu) \simeq S_{s}(q,\nu)$ . Basically one is summing over all phonon states in the first Brillouin zone. The incoherent dynamic structure factor,  $S_{s}(q,\nu)$ , can be expanded as follows [19]:

$$S_{s}(q,\nu) = \sum_{p} S_{s}^{p}(q,\nu)$$

$$= \sum_{p} \frac{e^{-2W(q)}}{p!} \left(\frac{hq^{2}}{4\pi m}\right)^{p} \prod_{i=1}^{p} \left(\int_{-\infty}^{\infty} d\nu_{i} \frac{g_{H}(\nu_{i})}{2\pi \nu_{i}} n(\nu_{i})\right) \delta(\nu + \sum_{i=1}^{p} \nu_{i}), (7.8)$$

where p is the p-phonon contribution and W(q) and  $n(\nu_i)$  are Debye-Waller factor and Bose-Einstein factor, respectively. The one- and two-phonon contributions in Eq. (7.8) are respectively

$$S_s^1(q,\nu) = e^{-2W(q)} \frac{hq^2}{8\pi^2 m} \frac{n(\nu) + 1}{\nu} g_H(\nu), \qquad (7.9)$$

$$S_s^2(q,\nu) = e^{-2W(q)} \frac{1}{2!} \left(\frac{hq^2}{8\pi^2 m}\right)^2$$

$$\int_{-\infty}^{\infty} d\nu_1 \frac{g_H(\nu_1)g_H(-\nu-\nu_1)}{\nu_1(-\nu-\nu_1)} n(\nu_1)n(-\nu-\nu_1). \tag{7.10}$$

We define a new function,  $A(q, \nu)$ , given by

$$A(q,\nu) = c(q)S_{s}(q,\nu)\frac{\nu}{n(\nu)+1},$$
(7.11)

where c(q) is a normalization constant. This  $A(q, \nu)$  is what KZ referred to as  $g(\nu)$ . If the one phonon term  $S^1_s(q, \nu)$  in Eq. (7.8) is dominant, then one can get the PDOS  $g_H(\nu)$  from  $S_s(q, \nu)$  i.e.,

$$g(\nu) = A(q, \nu) \simeq c(q) S_s^1(q, \nu) \frac{\nu}{n(\nu) + 1} = g_H(\nu). \tag{7.12}$$

Therefore,  $A(q, \nu)$  or  $g(\nu)$  is the PDOS,  $g_H(\nu)$ , associated with one phonon excitations when (1) the incoherent approximation is valid and (2) multi-phonon contributions to  $S_s(q, \nu)$  are negligible. Thus  $g(\nu)$  is equal to  $g_H(\nu)$  only when the above two approximations are valid. The fact that experimental  $g(\nu)$  and our calculation  $g_H(\nu) = 2Z(\nu)$  do not agree suggests that either (1) or (2) (or both) break down.

Now let us study the  $g(\nu)$  for the stage-2  $RbC_{24}$  via MD simulation. We can calculate directly  $S_s(q, \nu)$  related to the incoherent scattering cross section; unlike the experimental measurement we are not restricted to only large values of q to pick up the incoherent part of the dynamic structure factor. But to compare with the experiment, we choose  $q = 4\mathring{A}^{-1}$  which is in the range of the q values KZ used. Figure 7.6 gives  $A(q, \nu)$  (see Eq. (7.11)) for  $q = 4\mathring{A}^{-1}$  for  $RbC_{24}$  in both the solid and the liquid obtained following the procedure of KZ but by using  $S_{\bullet}(q,\nu)$  from our MD results. We see two peaks with the high frequency peak near 2THz. Our result for  $A(q, \nu)$  agrees with what KZ plotted as  $g(\nu)$  (circles in Figure 7.6), particularly very well for the liquid state. (The large intensity seen in the experiment near 3THz is most likely due to the intercalant dynamics perpendicular to the graphite plane. Also the experimental resolution near 3THz is about 1THz, which implies large error bars.) In the solid, the doublet structure we obtain near 1THz is washed out by experimental resolution of ~0.3THz near 1THz [7]. The agreement with the experiment is quite remarkable and tells us two things. One, the incoherent approximation made by KZ [7] is reasonable for  $q \sim 4 \mathring{A}^{-1}$  and two, our potential

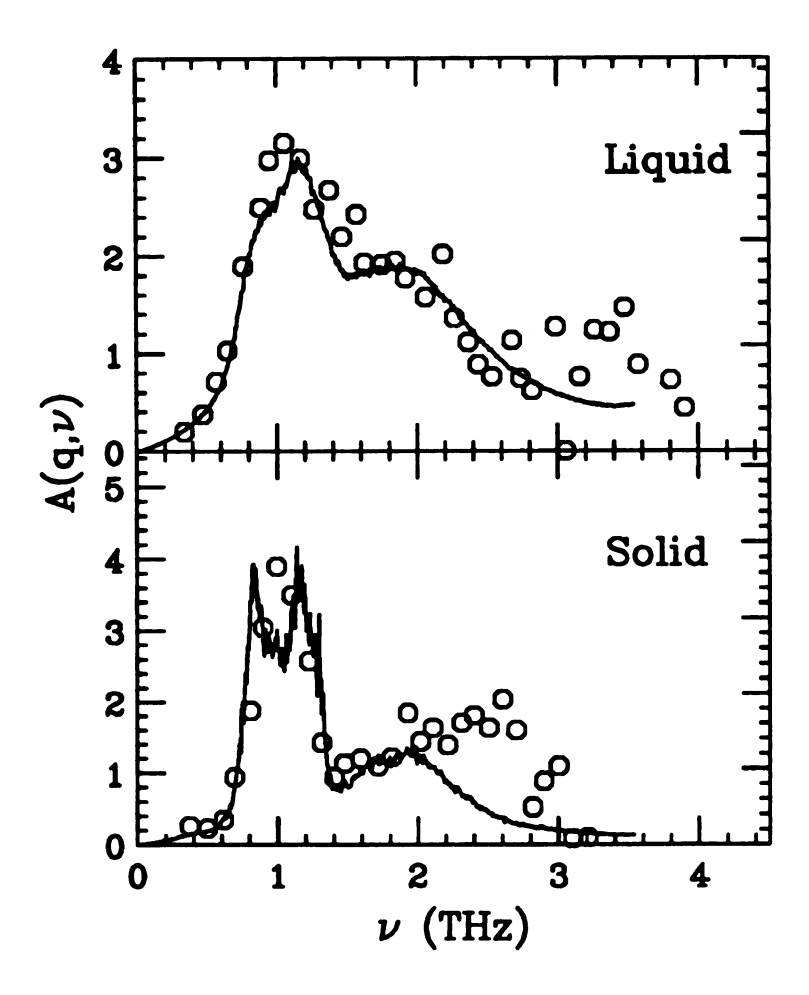


Figure 7.6:  $A(q, \nu)$  at  $q = 4 \mathring{A}^{-1}$ . The symbols are experimental data [7] for  $RbC_{24}$ . The top and the bottom panels correspond to the liquid and the solid states of the intercalants respectively. MD simulation was done at T=144K for the solid and T=250K for the liquid; the melting temperature in MD simulation is  $\sim 220K$ . Experimental data is for  $T=100K=0.6T_m$  for the solid and  $T=210K>T_m$  for the liquid where experimentally obtained  $T_m$  is 162K.

is adequate to represent the stage-2 Rb GIC. However, we still have a puzzle, the PDOS obtained through  $Z(\nu)$  i.e.  $g_H(\nu)$  does not show a peak near 2THz in contrast to the one obtained via  $S_s(q,\nu)$  for  $q=4\mathring{A}^{-1}$ , the latter of course agreeing with the results of KZ [7]. To solve this puzzle let us look at the multiphonon contribution to  $S_s(q,\nu)$ .

Since p-phonon contribution to  $S_s(q, \nu)$  is proportional to the  $q^{2p}$  [see Eq. (7.8)], one phonon contribution is dominant at small q [20]. Figure 7.7 gives  $A(q, \nu)$  for  $q = 0.4 \mathring{A}^{-1}$ ;  $A(q, \nu)$  does not show any high frequency peaks and is a replica of the  $Z(\nu)$  shown in Figure 7.5. This answers the puzzle i.e. to get the one-phonon density of states  $g_H(\nu)$  via the incoherent dynamic structure factor one must confine  $A(q, \nu)$  to small values of q for which Eq. (7.12) is valid. However it is impossible experimentally for  $RbC_{24}$  since the Rb ions are strong coherent scattering and for small q coherent scattering dominates over the incoherent scattering.

We further analyze the PDOS for  $RbC_{24}$  obtained from  $A(q,\nu)$  with  $q=0.4 \mathring{A}^{-1}$ . To see the effect of the corrugation potential, we calculate  $g_H(\nu)$  for a repulsive screened Coulomb system with the same density as  $RbC_{24}$  but in the absence of graphite corrugation potential. In Figure 7.7, we give the PDOS for both these systems, the corrugation free system is given in the inset of the figure. We see clearly that the low frequency modes are strongly suppressed in  $RbC_{24}$  due to the corrugation potential. One important feature of  $Z(\nu)$  or  $A(q=0.4,\nu)$  is their narrow width ( $\sim 0.5 THz$ ). This narrow width not only gives a well-defined low frequency peak seen in experimental  $g(\nu)$  but also leads to a pronounced two-phonon peak when q is large. As we increase the temperature beyond  $T_m$  ( $\sim 220 K$  in our MD), we find that the strength of the low frequency peak starts to decrease and that of the high frequency peak increases (see Figure 7.6), as expected for a multi-phonon

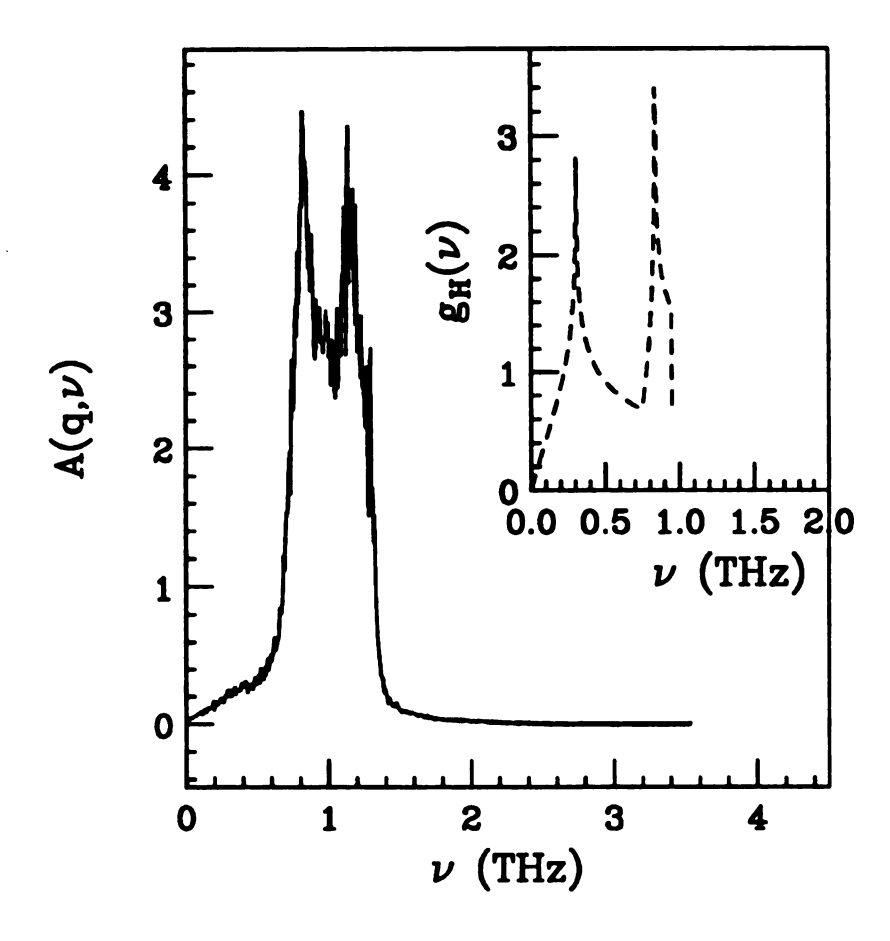


Figure 7.7:  $A(q, \nu)$  at  $q = 0.4 \mathring{A}^{-1}$  for the system II at 144K. This agrees very well with  $2Z(\nu)$  in Figure 7.5. Inset is the PDOS,  $g_H(\nu)$ , for the system I (without the corrugation potential) obtained from lattice dynamics calculation.

response. The overall peak near 1THz is quite well defined even above  $T_m$  although the doublet structure is weakened because of the softening of the TA modes. The reminiscence of the TA mode in the peak is interpreted as a characteristic feature of lattice-fluid as KZ pointed out. Even if they did not assign two peaks correctly, the interpretation of the persistence of the TA mode is reasonable. When we increase the temperature to about twice the melting temperature, the intensities of the one-and two-phonon peaks become comparable. This is clearly seen in experiments for both  $KC_{24}$  and  $RbC_{24}$  [7] thus confirming our multiphonon description of the high frequency peak.

To see how the relative spectral weights of multi-phonon responses change with q, we calculate the  $A(q,\nu)$  for a harmonic oscillator with a fundamental frequency 1THz and at temperature 150K. Fig. 7.8 shows that the multi-phonon contributions become important with increasing q as expected (Eqs. (7.9) and (7.10)). The dominant peak at 1THz is due to the one-phonon response. We see the evolution of two-and three-phonon contributions at 2THz and 3THz, respectively as we increase q. This clearly tells us that to get the PDOS we must confine  $A(q,\nu)$  to small values of q.

Finally, let us calculate multiphonon response of the system I which is a corrugation free system and compare it with that of the system II. Figure 7.9 shows  $A(q, \nu)$  at  $q = 4\mathring{A}^{-1}$  for the systems I and II both in the solid and in the liquid state. For the system I, either in the solid or in the liquid state, we cannot distinguish one-phonon from multiphonon contributions in  $A(q, \nu)$ . This tells us that a clear distinction between one and multiphonon process in  $A(q, \nu)$  is indeed a remarkable characteristic of strong corrugated system (with a narrow PDOS).

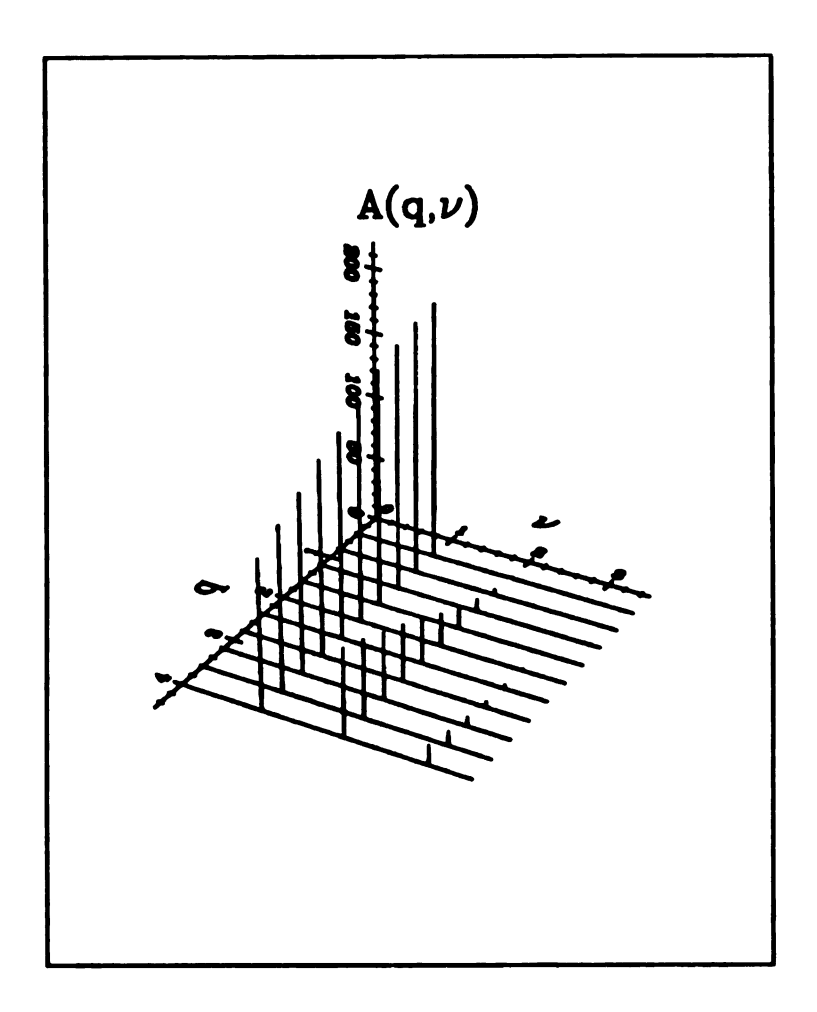


Figure 7.8: Frequency dependence of  $A(q, \nu)$ 's for different values of q from 0.4 to 4 in steps of 0.4 (in units of  $\mathring{A}^{-1}$ ) for a simple harmonic oscillator of fundamental frequency 1THz. This clearly shows the evolution of multi-phonon peaks as q increases.

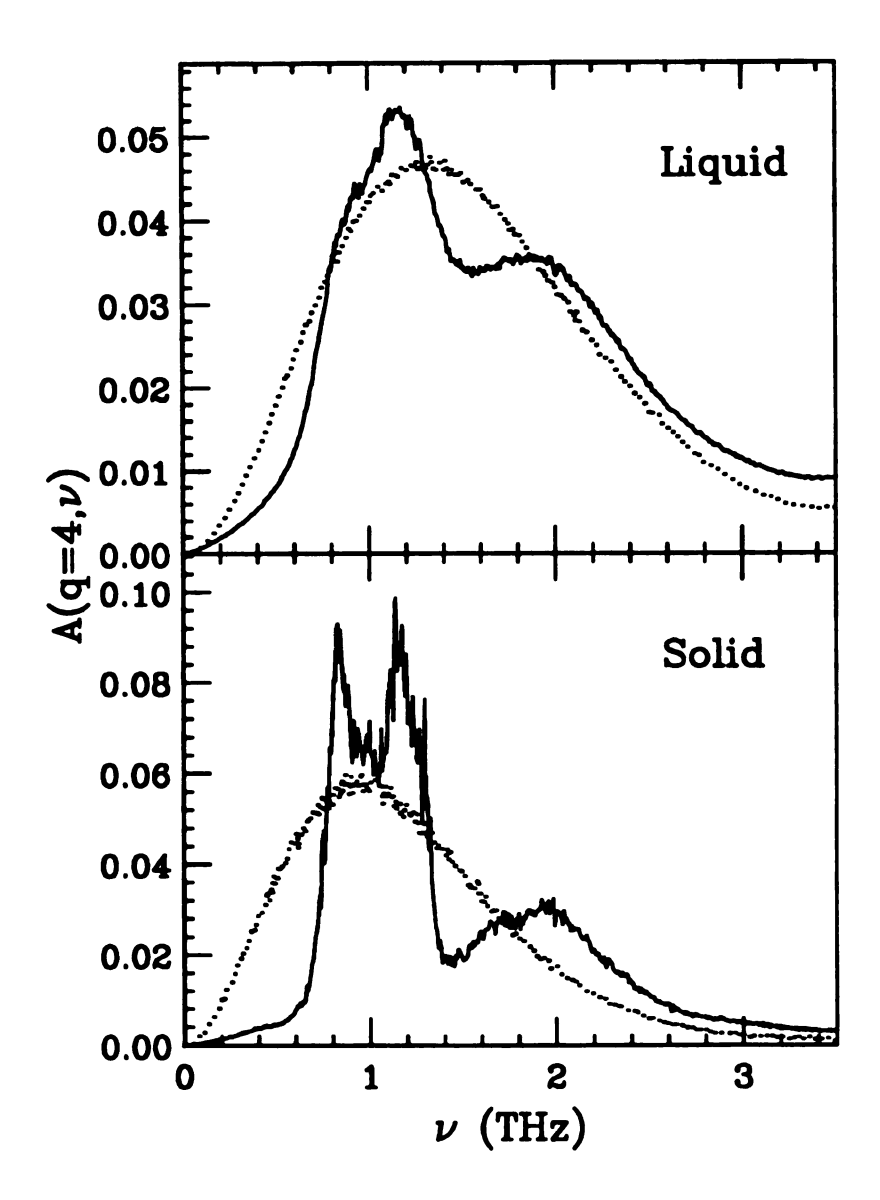


Figure 7.9:  $A(q,\nu)$  at  $q=4\mathring{A}^{-1}$  (multiphonon response) of the systems I (dotted line) and II (solid line). The system I (system II) corresponds to at T=120K (144K) for the solid and T=233K (250K) for the liquid; The melting temperature is about 200K and 220K for systems I and II, respectively.

#### 7.5 Summary and Conclusion

In conclusion, we have studied the phonon density of states for the stage-2 Rb GIC by using MD simulations. The advantage of the MD simulations is that we can obtain both the incoherent dynamic structure factor and the Fourier transform of the velocity-auto correlation function independently and by comparing these two, we can give a clear interpretation of the origin of the two peaks in the density of states obtained from the incoherent dynamic structure factor at large values of q. The results of the inelastic neutron scattering experiments of Kamitakahara and Zabel [7] for this system have been reproduced by MD simulations and we have clearly demonstrated that the multi-phonon response is extremely important at large q particularly for systems with strong substrate corrugation. We also predict that the relative strength of the high frequency peak compared to the low frequency one should increase with q which can be easily checked experimentally.

### **Bibliography**

- R. J. Birgenau and P. M. Horn, Science 232, 329 (1986); F. F. Abraham, Adv. Phys. 35, 1 (1986).
- [2] Graphite Intercalation Compounds, vol. 1, Structure and Dynamics, ed. by H. Zabel and S.A. Solin, Springer Series on Topics in Current Physics, Springer (1990).
- [3] S. N. Coppersmith et al., Phys. Rev. B 25, 349 (1982).
- [4] Edward Vives and Per-Anker Lindgard (preprint).
- [5] W. A. Steele (preprint).
- [6] M. Nielson, J. P. McTague and L. Passell, Phase transitions in Surface Films, edited by J. G. Dash and J. Ruvalds, p127 (1979).
- [7] W.A. Kamitakahara and H. Zabel, Phys. Rev. B 32, 7817 (1985).
- [8] H. Zabel in reference [2], p101.
- [9] M.M. Bredov, B.A. Kotov, N.M. Okuneva, V.S. Oskotskii, and A.L.Shakh-Bugadov, Fiz. Tverd (Lennigrad) 9, 287 (1967)[Sov. Phys. Solid State 9, 214 1967)].
- [10] Hyangsuk Seong, Surajit Sen, Tahir Çağin, and S. D. Mahanti, Phys. Rev. B45, 8841 (1992).

- [11] R. Clarke, J. N. Gray, H. Homma, and M. J. Winokur, Phys. Rev. Lett. 47, 1407 (1981); H. Zabel, et al., Phys. Rev. Lett. 57, 2041 (1986).
- [12] W.A. Kamitakahara, N. Wada, and S.A. Solin, Solid State Commun. 44, 297 (1982).
- [13] J. D. Fan, George Reiter, and S. C. Moss, Phys. Rev. Lett. 64, 188 (1990).
- [14] Hyangsuk Seong, S. D. Mahanti, Surajit Sen, and Tahir Çağin, Phys. Rev. B46, 8748 (1992).
- [15] Hyangsuk Seong and S. D. Mahanti (unpublished).
- [16] Quantum Theory of the Solid State; Part A, Joseph Callaway, Academic Press (1974).
- [17] Garboczi, Ph.D dissertation, Michigan State University (1984).
- [18] A. Rahman, M.J. Mandel and J.P.McTague, Jour. Chem. Phy. 64, 1564 (1976).
- [19] W. Marshall and S.W. Lovesey, Theory of Thermal Neutron Scattering, (Oxford University Press, Oxford, 1971).
- [20] P.A. Egelstaff, Dynamics of Disordered Materials, edited by D. Richter, A.J. Dianoux, W. Petry, and J. Teixeira, p2 (1988).

# Appendix A

# Average length for $\Delta \neq 0$

#### A.1 $\delta$ - bonds (same layer)

$$\langle L_{\mu,\mu} \rangle_{\delta}^{AA} = \langle L \rangle_{\delta} + a_{\delta\delta}^* x_{\mu}^2 \Delta$$

$$+ 4(b_{\delta\delta}^* + 2b_{\delta\nu}^*) x_{\mu} (L_{AA}^0 - L_{AB}^0)$$

$$- 2x_{\mu} [2x_{\mu} b_{\delta\delta}^* + (x_{\mu-1} + x_{\mu+1}) (b_{\delta\nu}^* + b_{\delta\eta}^*)] \Delta$$
(A.1)

$$\langle L_{\mu,\mu} \rangle_{\delta}^{BB} = \langle L \rangle_{\delta} + a_{\delta\delta}^{*} (1 - x_{\mu})^{2} \Delta$$

$$+ 4(b_{\delta\delta}^{*} + 2b_{\delta\nu}^{*})(1 - x_{\mu})(L_{AA}^{0} - L_{AB}^{0})$$

$$- 2(1 - x_{\mu})[2x_{\mu}b_{\delta\delta}^{*} + (x_{\mu-1} + x_{\mu+1})(b_{\delta\nu}^{*} + b_{\delta\eta}^{*})] \Delta$$
(A.2)

$$\langle L_{\mu,\mu} \rangle_{\delta}^{AB} = \langle L \rangle_{\delta} + a_{\delta\delta}^* x_{\mu} (1 - x_{\mu}) \Delta$$

$$+ 4(b_{\delta\delta}^* + 2b_{\delta\nu}^*) (1 - 2x_{\mu}) (L_{AA}^0 - L_{AB}^0)$$

$$- 2(1 - 2x_{\mu}) [2x_{\mu} b_{\delta\delta}^* + (x_{\mu-1} + x_{\mu+1}) (b_{\delta\nu}^* + b_{\delta\eta}^*)] \Delta \tag{A.3}$$

$$\langle L \rangle_{\delta} = \frac{l}{l+m} \sum_{\mu=1}^{l+m} \left[ x_{\mu} L_{AA}^{0} + (1-x_{\mu}) L_{BB}^{0} - x_{\mu} (1-x_{\mu}) \Delta \right]$$
 (A.4)

$$a_{\delta\delta}^* = 4\sum_{\mathbf{Q}} [\hat{\delta} \cdot \vec{D} (\mathbf{Q})^{-1} \cdot \hat{\delta}] \sin^2(\frac{\mathbf{Q} \cdot \hat{\delta}}{2})$$
 (A.5)

$$b_{\delta\nu}^{\bullet} = \sum_{\mathbf{Q}} [\hat{\delta} \cdot \stackrel{\leftrightarrow}{D} (\mathbf{Q})^{-1} \cdot \hat{\nu}] \sin(\mathbf{Q} \cdot \hat{\delta}) \sin(\mathbf{Q} \cdot \hat{\nu})$$
 (A.6)

$$s_{\nu\eta}^* = \sum_{\mathbf{Q}} [\hat{\nu} \cdot \stackrel{\leftrightarrow}{D} (\mathbf{Q})^{-1} \cdot \hat{\eta}] (1 - \cos(\mathbf{Q} \cdot \hat{\nu}) (1 - \cos(\mathbf{Q} \cdot \hat{\eta}))$$
 (A.7)

#### A.2 $\nu(\eta)$ - bonds (interlayer)

$$\langle L_{\mu,\mu-1} \rangle_{\nu}^{AA} = \langle L_{\mu,\mu-1} \rangle_{\nu} + a^{**}(x_{\mu-1} + x_{\mu})(L_{AA}^{0} - L_{AB}^{0})$$

$$+ \Delta \left[ a^{*}_{\nu\nu}(x_{\mu-2}x_{\mu-1} - x_{\mu-1}x_{\mu} + x_{\mu}x_{\mu+1}) - 2b^{*}_{b\nu}(x_{\mu-1}^{2} + x_{\mu}^{2}) - 2b^{*}_{b\nu}(x_{\mu-1}^{2} + x_{\mu}^{2}) - 2b^{*}_{\nu\nu}(x_{\mu-2}x_{\mu-1} + x_{\mu}x_{\mu+1}) - b^{*}_{\nu\eta}(x_{\mu-2}x_{\mu-1} + 2x_{\mu-1}x_{\mu} + x_{\mu}x_{\mu+1}) + s^{*}_{\nu\eta}(x_{\mu-2}x_{\mu-1} - 2x_{\mu-1}x_{\mu} + x_{\mu}x_{\mu+1}) \right]$$

$$\langle L_{\mu,\mu-1} \rangle_{\nu}^{BB} = \langle L_{\mu,\mu-1} \rangle_{\nu} + a^{**}(1 - x_{\mu-1} + 1 - x_{\mu})(L_{AA}^{0} - L_{AB}^{0})$$

$$+ \Delta [a^{*}_{\nu\nu}((1 - x_{\mu-2})(1 - x_{\mu-1}) - (1 - x_{\mu-1})(1 - x_{\mu}) + (1 - x_{\mu})(1 - x_{\mu+1}))$$

$$+ 2b^{*}_{b\nu}((1 - x_{\mu-1})x_{\mu-1} + (1 - x_{\mu})x_{\mu}) + 2b^{*}_{\nu\nu}(x_{\mu-2}(1 - x_{\mu-1}) + (1 - x_{\mu})x_{\mu+1})$$

$$+ b^{*}_{\nu\eta}((x_{\mu-2} + x_{\mu})(1 - x_{\mu-1}) + (1 - x_{\mu})(x_{\mu-1} + x_{\mu+1}))$$

$$- s^{*}_{\nu\eta}((1 - x_{\mu-2})(1 - x_{\mu-1}) - 2(1 - x_{\mu-1})(1 - x_{\mu}) + (1 - x_{\mu})(1 - x_{\mu+1}))]$$

$$(A.9)$$

$$\langle L_{\mu,\mu-1} \rangle_{\nu}^{AB} = \langle L_{\mu,\mu-1} \rangle_{\nu} + a^{**} (1 - x_{\mu-1} - x_{\mu}) (L_{AA}^{0} - L_{AB}^{0})$$

$$+ \Delta \frac{S}{(1 - x_{\mu})x_{\mu-1} + x_{\mu}(1 - x_{\mu-1})}$$
(A.10)

where

$$S = a_{\nu\nu}^* (x_{\mu-2}x_{\mu-1} - x_{\mu-1}x_{\mu} + x_{\mu}x_{\mu+1})$$

$$+2b_{\delta\nu}^* ((1-2x_{\mu})(1-x_{\mu-1})x_{\mu-1}^2 + (1-2x_{\mu-1})(1-x_{\mu})x_{\mu}^2)$$

$$+2b_{\nu\nu}^* (x_{\mu-2}x_{\mu-1}(1-x_{\mu-1})(1-2x_{\mu}) + (1-2x_{\mu-1})(1-x_{\mu})x_{\mu}x_{\mu+1})$$

$$+b_{\nu\eta}^* ((x_{\mu+1}+x_{\mu-1})(1-x_{\mu})x_{\mu}(1-2x_{\mu-1}) + (x_{\mu-2}+x_{\mu})(1-x_{\mu-1})x_{\mu-1}(1-2x_{\mu}))$$

$$-s_{\nu\eta}^* ((x_{\mu+1}+x_{\mu-1})(1-x_{\mu})x_{\mu}(1-2x_{\mu-1}) - (x_{\mu-2}+x_{\mu})(1-x_{\mu-1})x_{\mu-1}(1-2x_{\mu}))$$
(A.11)

## Appendix B

#### **EMT** in Harmonic Limit

In the harmonic limit where  $\gamma_A = \gamma_B = 0$ , Eq. (3.32) reduces to a simple form,

$$\langle h_{\alpha} \rangle = \frac{F}{K_{c}' + K_{\alpha}} + \frac{K_{e}' h_{e} + K_{\alpha} h_{\alpha}^{0}}{K_{c}' + K_{\alpha}}.$$
 (B.1)

Eq. (3.28) then becomes

$$\langle h \rangle = h_e + \frac{F}{K_e}. \tag{B.2}$$

Eq. (3.33) gives

$$h_e + \frac{F}{K_e} = (1 - x) \frac{F}{K'_e + K_A} + (1 - x) \frac{K'_e h_e + K_A h_A^0}{K'_e + K_A}$$

$$+ x \frac{F}{K'_e + K_B} + x \frac{K'_e h_e + K_B h_B^0}{K'_e + K_B}.$$
(B.3)

This equation is satisfied under an arbitrary force F. If we rearrange Eq.(B.3), we have an equation such as  $\alpha F + \beta = 0$ . Solutions of this equation for the arbitrary force F are  $\alpha = 0$  and  $\beta = 0$ . Therefore, we obtain two equations which are exactly the same as the results of Thorpe *et al.* [14].

## Appendix C

# Mean Square Displacement in d-dimension

Let me show here how Eq. (6.6) is obtained. All what we need to know is a volume element  $d\mathbf{r}$  in d-dimensional spherical coordinate<sup>1</sup>. To get the  $d\mathbf{r}$ , we use a following identity.

$$\int_{-\infty}^{\infty} dx e^{-x^2} \int_{-\infty}^{\infty} dy e^{-y^2} \cdots \int_{-\infty}^{\infty} dz e^{-z^2} = \int_{0}^{\infty} dr S_d r^{d-1} e^{-r^2}$$
 (C.1)

where  $d\mathbf{r} \equiv S_d r^{d-1} dr$  and  $r^2$  in d-dimension is  $x^2 + y^2 + \cdots z^2$ .

L.H.S. of Eq. (C.1) =  $\pi^{d/2}$ .

R.H.S. of Eq. (C.1) = $S_d\Gamma(d/2)/2$ 

where  $\Gamma$  is the gamma function. Therefore,  $S_d = 2\sqrt{\pi}^d/\Gamma(d/2)$ .

Now, we are ready to calculate the mean square distance in d-dimension.

$$\langle (\mathbf{r}(t) - \mathbf{r}(0))^2 \rangle = \int d\mathbf{r} r^2 G_s(\mathbf{r}, t)$$
 (C.2)

$$= \left(\frac{1}{2\pi\alpha(t)}\right)^{d/2} \int d\mathbf{r} r^2 e^{-r^2/2\alpha(t)} \tag{C.3}$$

$$= \left(\frac{1}{2\pi\alpha(t)}\right)^{d/2} S_d \int dr r^{d+1} e^{-r^2/2\alpha(t)} \tag{C.4}$$

<sup>&</sup>lt;sup>1</sup>Shang-Keng Ma, Statistical Mechanics, World Scientific, p77 (1985); M.F. Thorpe, Lecture note

$$= \left(\frac{1}{2\pi\alpha(t)}\right)^{d/2} S_d \int \frac{\alpha(t)}{2} dx \sqrt{2\alpha(t)}^{d+1} x^{d/2} e^{-x}$$
 (C.5)

$$= \left(\frac{1}{2\pi\alpha(t)}\right)^{d/2} S_d \frac{\alpha(t)}{2} \sqrt{2\alpha(t)}^{d+1} \Gamma(d/2+1)$$
 (C.6)

$$= \alpha(t)d \tag{C.7}$$